LBNL-54008

Ernest Orlando Lawrence Berkeley National Laboratory

Coherence Properties of Extreme Ultraviolet/Soft X-Ray Sources

Yanwei Liu

Materials Sciences Division

October 2003

Ph.D. Thesis

REFERENCE COPY
Does Not
Circulate

Library Annex Reference
Lawrence Berkeley National Laboratory

LBNL-54008

Copy 1

DISCLAIMER

This document was prepared as an account of work sponsored by the United States Government. While this document is believed to contain correct information, neither the United States Government nor any agency thereof, nor the Regents of the University of California, nor any of their employees, makes any warranty, express or implied, or assumes any legal responsibility for the accuracy, completeness, or usefulness of any information, apparatus, product, or process disclosed, or represents that its use would not infringe privately owned rights. Reference herein to any specific commercial product, process, or service by its trade name, trademark, manufacturer, or otherwise, does not necessarily constitute or imply its endorsement, recommendation, or favoring by the United States Government or any agency thereof, or the Regents of the University of California. The views and opinions of authors expressed herein do not necessarily state or reflect those of the United States Government or any agency thereof or the Regents of the University of California.

LBNL-54008

Coherence Properties of Extreme Ultraviolet/ Soft X-Ray Sources

Yanwei Liu
Ph.D. Thesis

Department of Applied Science and Technology
University of California, Berkeley

and

Materials Sciences Division
Ernest Orlando Lawrence Berkeley National Laboratory
University of California
Berkeley, CA 94720

October 2003

This work was supported by the Director, Office of Science, Office of Basic Energy Sciences, Materials Sciences Division, of the U.S. Department of Energy under Contract No. DE-AC03-76SF00098.

Coherence Properties of Extreme Ultraviolet/ Soft X-Ray Sources

Copyright © 2003

by

Yanwei Liu

The U.S. Department of Energy has the right to use this document
for any purpose whatsoever including the right to reproduce
all or any part thereof.

Abstract

Coherence Properties of Extreme Ultraviolet / Soft X-Ray Sources

by

Yanwei Liu

Doctor of Philosophy in Applied Science and Technology

University of California, Berkeley

Professor David T. Attwood, Chair

Extreme ultraviolet (EUV) and soft x-ray (SXR) wavelengths, covering the electromagnetic spectrum region of ~1-40nm, provide many unique opportunities in a wide range of scientific research and industrial applications. Coherence properties of light sources play critical roles in many of these applications. In this thesis, properties of three currently available coherent EUV/SXR sources: undulators in synchrotron radiation facilities, lasers, and high-order harmonic generation (HHG) sources, are investigated.

For undulator radiation, the detailed spectrum and angular distribution in the important central radiation cone are studied. The radiation from a single electron including the effects of limited number of oscillations, and the radiation from an electron beam with finite electron beam size and divergence angle are analytically and numerically calculated.

Based on amplified spontaneous emission (ASE) process, EUV/SXR lasers have long been limited to poor spatial coherence. In a series of Young's two-pinhole experiments performed with a capillary discharge 46.9-nm EUV laser, rapid spatial coherence buildup has been observed as a result of refractive anti-guiding (mode selection) in a long and narrow plasma column. It is demonstrated for the first time that essentially full spatial coherence can be obtained from an ASE-based EUV/SXR laser.

High-order Harmonic Generation is a promising method for generating coherent EUV/SXR radiation by up-shifting intense optical lasers to very high order harmonics. However, due to the strong interaction between the laser field and the atom, coherence of the pump laser field is not always preserved. Through a phase-matched HHG process inside a hollow-core fiber, spatially coherent EUV radiation is generated and verified by two-pinhole interference experiments. Fourier analysis of the two-pinhole interference pattern reveals spectral information characteristic of the broadband radiation, providing a simple yet useful method for absolute wavelength and spectrum measurements at EUV/SXR wavelengths.

Comparing the sources, undulator radiation has the best spectral coverage, highest average photon flux, and the flexibility to produce desired coherence properties with adequate filtering techniques. The other two sources have made significant progress recently and the experiments reported here have demonstrated their ability to generate coherent radiation with useful photon flux at EUV wavelengths. With their compact sizes, they are likely to play important roles in EUV/SXR science and technology in the coming years.

Table of Contents

Acknowledgements iv

Chapter 1. Introduction

1.1 Opportunities at Extreme Ultraviolet and Soft X-Ray Wavelengths 1

1.2 High Quality EUV/SXR Optics 4

1.3 EUV/SXR Sources 8

1.4 About This Thesis 10

Chapter 2. Optical Coherence at EUV/SXR Region

2.1 Fundamental Optical Coherence Theory 11

2.1.1 Temporal Coherence and Coherence Time 13

2.1.2 Spatial Coherence and Coherence Area 15

2.1.3 Phase-Space Product, Brightness and Coherent Power (Flux) 19

2.2 Importance of Characterizing the Coherence Properties of Sources 23

2.3 Generating Coherent Radiation at EUV/SXR Region 26

Chapter 3. Undulator Radiation

3.1 Undulator Radiation Basics 29

3.2 Properties of Undulator Radiation by a Single Electron 30

3.2.1 Central Radiation Cone 33

3.2.2 Limited Number of Oscillations 35

3.2.3 Photon Beam (by a Single Electron) 40

3.3 Properties of Undulator Radiation from a Finite Electron Beam 40

3.3.1 The Influence of Beam Size 41

3.3.2 The Influence of Beam Divergence 42

3.3.3 Spectral Brightness and Coherent Power Calculations 47

3.4 Undulator Harmonics 48

3.5 An Example 50

3.6 Comments on Undulator Radiation as EUV/SXR Source 53

Chapter 4. EUV/SXR Lasers

4.1 Lasers Working in the EUV/SXR Spectral Region 55

4.1.1 Lasing Medium: Hot-Dense Plasma 55

4.1.2 Amplified Spontaneous Emission (ASE) 57

4.1.3 Limited Coherence of EUV/SXR Lasers and Possible Solutions 59

4.2 Coherence Properties of a 46.9-nm EUV Laser 63

4.2.1 Introduction to the Laser 63

4.2.2 Spatial Coherence Measurements 65

4.2.3 The 46.9-nm Laser as a Coherent Source 72

4.3 Focusability of the 46.9-nm EUV Laser 73

4.3.1 Experiment Setup 73

4.3.2 M^2 Characterization of Light Beam 75

4.3.3 Results 77

4.4 Comments on Lasers as EUV/SXR Source 79

Chapter 5. High-order Harmonic Generation (HHG)

5.1 HHG Basics 82

5.1.1 Semi-classical Model of HHG 84

5.1.2 Nonlinear Polarization for HHG 88

5.1.3 The Two Trajectories and Intensity-Dependent Dipole Phase 90

5.1.4 Phase-Matching Effect 93

5.1.5 Phase-Matched HHG in Hollow Fiber 95

5.2 Observation of Full Spatial Coherence from a HHG Source 96

5.2.1 Experiment Setup 97

5.2.2 Recorded Two-Pinhole Interference Patterns 98

5.2.3 Results 100

5.3 Two Pinhole Interference Experiment with Polychromatic Light 101

5.3.1 Theoretical Analysis 102

5.3.2 The Spectrum Measurement Experiment 106

5.4 Ultrashort Pulse Generation 110

5.5 Comments on HHG as EUV/SXR Source 113

Chapter 6. Other EUV/SXR Sources

6.1 Synchrotron-Based Sources 115

6.1.1 Bending Magnet Radiation 116

6.1.2 Wiggler Radiation 119

6.1.3 Femtosecond Pulses at Short Wavelengths 120

6.2 Plasma Radiation Sources for EUV Lithography 124

Chapter 7. Conclusion 128

References 131

Acknowledgements

First of all, my deepest appreciation goes to Professor David Attwood. His guidance led me into this interesting field of EUV/SXR radiation and applications. I have benefited not only from his broad knowledge, but also his dedication and sustained support to his students. This work would not have been possible without his guidance and suggestions. Through his connections, I also have had the opportunity to collaborate with other outstanding scientists in this field: Prof. Jorge J. Rocca at Colorado State University, and Profs. Henry C. Kapteyn and Margaret M. Murnane at University of Colorado at Boulder. Their expertise and world-class work on EUV laser, ultrafast laser, and high harmonic generation, greatly enhanced my understanding and knowledge on these sources.

As a student in Applied Science and Technology program, I want to thank our Graduate Advisor Prof. Daryl Chrzan for his guidance in my course selection and for serving on all the important committees throughout my study: prelim exam, qualify exam, and dissertation. I would also like to thank Prof. Yuen-Ron Shen of the Physics Department for serving on my qualify exam and dissertation committee.

My special thanks to Ms. Patricia M. Berumen, AS&T program coordinator, for her help and assistance in making the transition to Berkeley for me as smooth as possible, and her help with all the administrative issues.

Throughout my studies I worked as a research assistant in the Center for X-Ray Optics at Lawrence Berkeley National Lab. I received valuable help and support from staff members

of CXRO. Among them I am particularly grateful to Eric Gullikson, Farhad Salmassi, and Andrew Aquila for their help on multilayer mirror coating and characterization. I have also benefited tremendously from the many discussions with Patrick Naulleau, Gregory Denbeaux, Chang Chang, Weilun Chao, and Kristine Rosfjord.

Finally, thanks to my wife Yi Xia, and our family members in China for their unconditional love, encouragement and support. I would not be where I am today without them.

Chapter 1

Introduction

1.1 Opportunities at Extreme Ultraviolet and Soft X-Ray Wavelengths

The extreme ultraviolet (EUV) and soft x-ray (SXR) regions of the electromagnetic spectrum provide many unique opportunities in both scientific research and industrial applications. In this region, the wavelengths extend from approximately 1 nm to 40 nm, corresponding to photon energies from 30 eV to several keV. The applications of EUV/SXR radiation can be roughly grouped to those utilizing these photon energies and those taking advantage of the wavelengths, while in some cases combining these two aspects can give additional benefits.

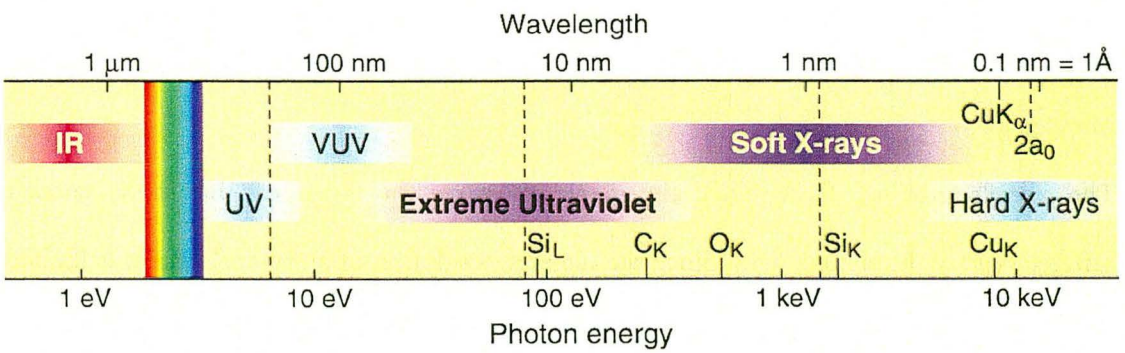

Figure 1-1. The EUV/SXR region of the electromagnetic spectrum. Shorter wavelengths in this region permit one to "see" and "write" smaller features, as in microscopy and lithography, while photon energies from 30eV to several keV provide efficient and sensitive elemental and chemical identifications. [1]

The photon energies in EUV/SXR region are well matched to the primary atomic resonance of most elements across the periodic chart, permitting clear elemental identifications. While

infrared/visible/UV light are routinely used to probe the vibration states of molecules and the electronic states of valence and outer shell electrons, the relatively high photon energy of EUV/SXR can reach the core levels of atoms. The core levels reachable by EUV/SXR are usually those "shallow" ones, which are sensitive to the electronic environment and have abundant chemical information. As a result, EUV/SXR absorption spectra usually have rich features, which can be used as chemical "fingerprints" for the system. Furthermore, due to efficient absorption, the penetration depth of EUV/SXR photons in most materials is generally on the order of a micron or less, thus providing an ideal probe for surfaces. These unique interaction properties between materials and EUV/SXR photons are revealing much new information to scientists in many disciplines, including atomic and molecular physics, chemistry, material science, surface, and environmental science. Some examples of the techniques used are XPS (X-ray Photoemission Spectroscopy), NEXAFS (Near Edge X-ray Absorption Fine Structure) Spectroscopy and PEEM (PhotoElectron Emission Microscopy).

The wavelengths of EUV/SXR are much shorter than those of the more familiar infrared/visible/ultraviolet light. Since the ultimate resolution of an optical system is limited by the wavelength, EUV/SXR based systems have intrinsic advantages over their optical counterparts when trying to "see" smaller features, as in microscopy, or "write" smaller patterns, as in lithography. For example, a SXR microscope has reached spatial resolution of 21nm [2]. Critical for the semiconductor industry to maintain the "Moore's Law" (the doubling of transistors on a chip every couple of years), EUV lithography [3] (using EUV light at 13.4 nm) will follow current deep-UV lithography (in which the shortest working wavelength is currently 193 nm) to be the next generation technology for the patterning of computer chips. EUV is expected to enter high volume manufacturing at so-called 45-nm

and 32-nm "nodes", in the years 2007 and 2009. Also benefiting from the short wavelength, an EUV interferometer can measure wavefront aberrations with accuracy smaller than the size of an atom [4]. With wavelength and resolution in nanometer scale, EUV/SXR imaging system will also find more applications in the fabrication and characterization of nanostructures, whose amazing properties are attracting much research interest.

Although aforementioned applications generally only take advantage of one aspect of EUV/SXR light (either photon energy or wavelength), combining them can give some interesting results. A good example is the operating of SXR microscope at the so-called "water window" [5] region. In this region, photon energy lie between the carbon K-edge (284 eV) and the oxygen K-edge (543 eV). The microscope usually operates just below the oxygen edge (corresponding to wavelength of 2.4nm), where organic matter is highly absorptive (due to carbon) while water is relatively transparent. This provides a natural contrast when observing cells in their natural aqueous environment, an attractive feature to biologists, since higher resolution electron microscope can only work on samples without water's presence.

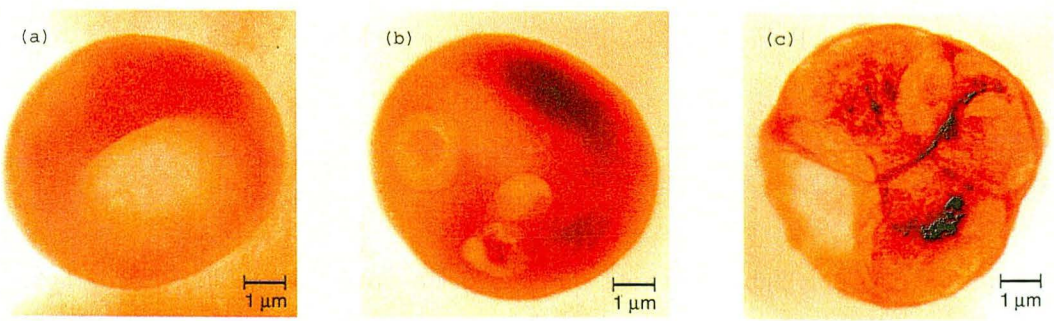

Figure 1-2. Images of malaria-infected red blood cells obtained by a SXR microscope operating at "water window". Images are cells (a) un-infected, (b) newly infected and (c) 36 hours after infection. Extracted from Ref. 6.

Recently there have been more and more clever and creative uses of the high spatial resolution EUV/SXR microscope using photons with intentionally selected properties (particular photon energy, polarization, etc.). Such experiments demonstrate the power and flexibility of EUV/SXR microscopy. An example is illustrated in Fig. 1-3, where a FeGd alloy is imaged at three slightly different wavelengths. The image shows dramatic changes due to the polarization-depended interaction between photons and iron atoms.

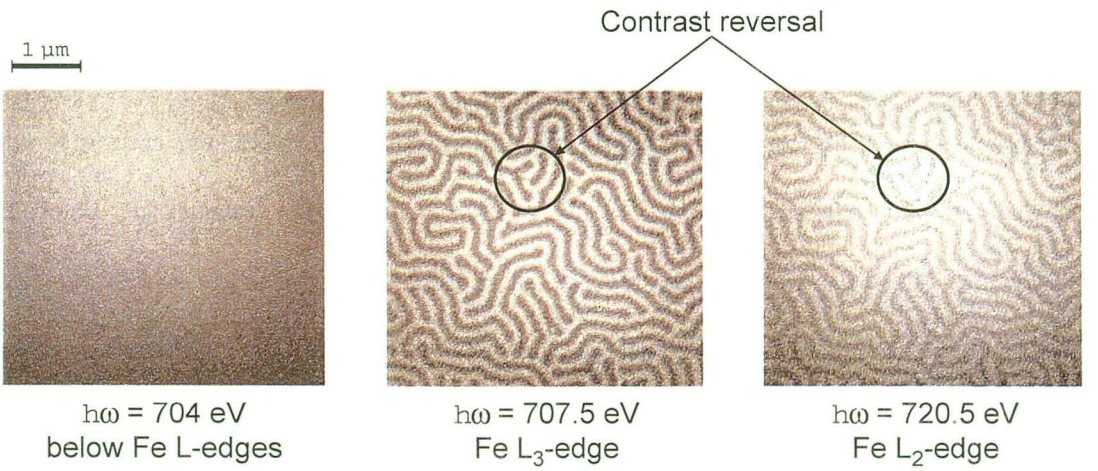

Figure 1-3. High spatial resolution SXR imaging of magnetic domains on a FeGd alloy. Images taken at slightly different photon energies around Fe L-edges show dramatic changes. (Courtesy of P. Fischer, Max-Planck-Institute for Metals Research) [7]

1.2 High Quality EUV/SXR Optics

All applications using light as a tool need adequate optics to manipulate the light, for example collect, transport and focus it. Materials are generally too absorptive in EUV/SXR region; therefore familiar refractive optics (e.g., lenses) do not work. Even if some particular materials are relative transparent at particular wavelengths (usually just below a primary absorption edge, like Si at ~90 eV or Al at ~70 eV), their refractive indexes are so close to

unity that no noticeable refraction will occur. This close-to-one refractive index also cause very weak reflection at any interface, so another type of familiar optics, metallic film coated reflectors, is also not a viable option. Fortunately, in the past decade there has been great progress in the development of EUV/SXR optics. Two types of high quality optics are now readily available: multilayer-coated reflective optics, and diffractive optics represented by Fresnel zone plate.

Multilayer coatings greatly enhance total reflectivity as a result of constructive interference between reflections from the many interfaces. For example, a 50-period Mo/Si multilayer coating can achieve more than 70% peak reflectivity just below the Si L_3-edge (99.2 eV), at wavelengths in 13–14 nm range. This provides the "enabling technology" for EUV lithography. By choosing adequate material combinations, multilayer coatings can cover the long wavelength end of EUV/SXR region with fairly good reflectivity.

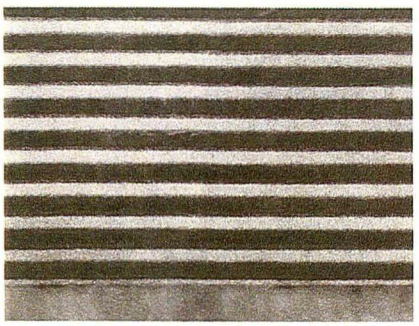

(a)

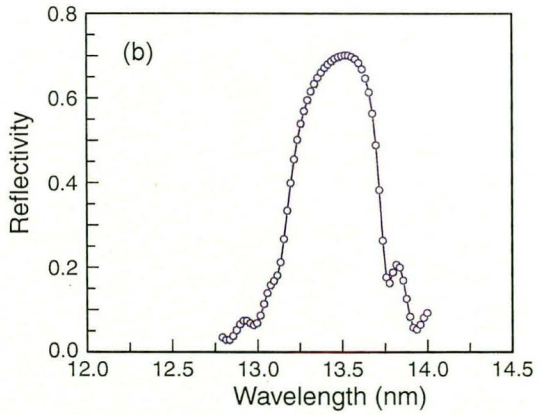

(c)

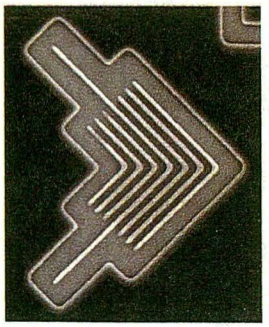

39-nm lines

Figure 1-4. (a) Side view of a Mo/Si multilayer coating. Mo is the dark layer and Si is the light one. [8] (b) 70% reflectivity can be reached by a 50-pair Mo/B_4c/Si multilayer. (Courtesy of Sasa Bajt, Lawrence Livermore National Lab) (c) 39 nm lines printed by multilayer mirror based EUV lithography testing system. [9]

The resonant wavelength for constructive interference (where the reflectivity is peaked) of a multilayer is twice the thickness of a unit pair (known as the d-spacing). This is the case of normal incidence, first order; a more general expression is $m\lambda = 2d \sin \theta$, where θ is the incidence angle measured from the surface and m is the order. As a result, the thickness of each layer is roughly a quarter of the desired working wavelength. Given the short wavelength of EUV/SXR, each layer is usually only tens of atomic layers thick. This not only constitutes a tremendous challenge on the layer deposition technique, but also effectively prevents multilayer mirrors from working in the shorter wavelength end of EUV/SXR region. Diffractive optics, represented by Fresnel zone plate, is the alternative for this region. Currently a state-of-the-art e-beam lithography system can fabricate zone plate having hundreds of zones with minimum displacement error and outer zone width of around 20 nm [10], the enabling technology of high spatial resolution SXR microscope mentioned before.

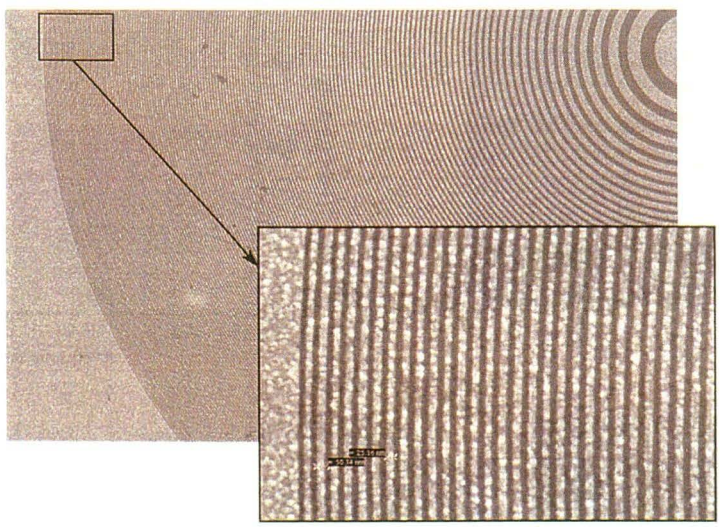

Figure 1-5. A zone plate consisting of 618 zones with outer zone width of 25nm. Such high quality optics is the core component of a high spatial resolution SXR microscope. (Courtesy of E. Anderson, Center for X-Ray Optics, Lawrence Berkeley Lab)

Diffractive optics also provide the design freedom for "customized" patterns to generate desired amplitude and phase change, which can be much more complex and useful than the simple spherical wave phase factor obtained by a zone plate. Figure 1-6 shows one such example. In it, the XOR pattern of a zone plate and grating produced a focal plane dominated by the foci of ± 1 orders, while the usually strong 0th order is eliminated. In the future, wavefront engineering using diffractive optics should find more applications in EUV/SXR regions, where as few as possible optics elements are desired (due to poor efficiency), and traditional wavefront correction and modulation methods, which depend on refractive optics, do not work.

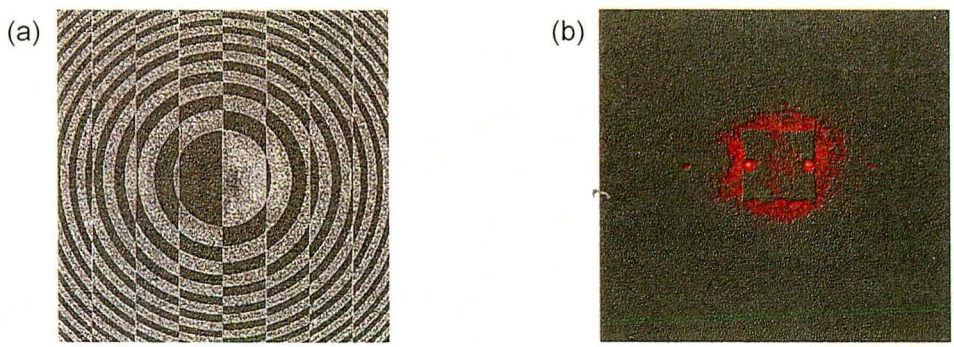

Figure 1-6. (a) A designed pattern combining zone plate and grating in one element. (b) The intensity distribution at focal plane of (a). Extracted from the cover of Applied Optics, Dec. 2002 issue. See Ref. 11 for details.

The availability of high quality optics has greatly helped the developments of optical systems in the EUV/SXR region to take advantage of the short wavelengths. At this point, it's interesting to have a look at the situations in the hard x-ray region, where the wavelengths are in the order of 0.1 nm and less. Although the wavelengths are even shorter, the lack of high quality optics greatly limits the performance of imaging systems in that region. For

example, reflective optics used in hard x-ray telescope is limited to grazing-incidence mirror, usually having a bulky size [12]. In contrast, normal incidence multilayer mirrors help to make very compact EUV telescope and eliminate many problems associated with grazing-incidence optics, for example aberrations and nonspecular scattering [13]. For microscope, hard x-ray zone plates are troubled with the lack of interaction between hard x-rays and materials. As a result, opaque zones have to use thick materials, in turn making the fabrication of narrow zones difficult. Since the resolution of a zone plate system is approximately equal to the minimum (outer zone) width, currently the highest spatial resolution is achieved by a SXR microscope, rather than a hard x-ray one.

1.3 EUV/SXR Sources

Without practical light sources, all these great applications and optics would be pointless. Historically the EUV/SXR region is a relatively "dark" region in the exploration of electromagnetic spectrum, with less research going on. While part of the reason may be EUV/SXRs can't exist "naturally" (due to strong absorption by essentially all materials) so that even experiments have to be done in vacuum, the major obstacle now is the source. The reason is rather simple: photon energies of EUV/SXR are simply too high for our ordinary world which fits, naturally, to the visible light. For example, let's consider a thermal source based on black body model. Having a surface temperature around 6000 K, the Sun is a good radiator of visible photons with energies in ~1 eV region (For T=6000 K, kT = 0.3 eV, k is the Boltzmann constant). To shift the peak of spectrum to EUV around 100 eV, this will require the temperature go up 100 times to a formidable 600,000 K, far away from our 300K equilibrium world.

Given the difficulties of generating EUV/SXR radiation, it is no surprise that currently the widely used source is synchrotron radiation, a rather non-conventional way of generating light. Synchrotron radiation is produced when a particle (usually an electron) moving at speed close to *c* (speed of light) undergoes acceleration (typically a "turn" in magnetic field). Such radiation has a very broad spectrum due to the extreme relativistic motion, extending well into x-ray region with GeV-level electrons [14]. Driven by both the exciting research opportunities and the lack of dependable source in the short wavelength region, dedicated synchrotron radiation facilities have been constructed throughout the world and still more planned. Currently they are the main mature and practical sources in short wavelength region. (Synchrotron radiation facilities are usually built with their particular spectrum coverage in mind. There are "low energy" machines with electron energy in the range of 1-2 GeV to cover EUV/SXR region, "high energy" machines with electron energy in the range of 6-8 GeV to cover hard x-ray region and some "medium energy" machines are also available. With the help of novel magnetic structures, in fact either of them is capable of covering the whole band, only a matter of optimization.)

Synchrotron radiation apparently has its "shortcomings" in terms of expense and accessibility. Alternatively, smaller scale (so-called table-top) sources have also been actively pursued. These sources are usually based on the radiation from hot-dense plasmas, which have high enough temperature and density to generate intense EUV/SXR radiation. The generation of such hot and dense plasmas requires significant energy to be delivered, on a very short time scale, accomplished by high peak power lasers or fast high-current electrical discharges. In addition to the continuum radiation, ions in the hot plasmas can be excited and produce strong line emission. With suitable plasmas conditions, population inversion and lasing can occur. [15]

More recently high order harmonic generation (HHG) has enjoyed extensive research interest as another promising technique to generate EUV/SXR. In HHG, strong electric fields, generated by focused terawatt-level (peak power) femtosecond lasers, induce extremely high order nonlinear process, up-shifting photon energies from the IR to greater than 300 eV [16]. With recent progress in both the IR laser pump and optimization of the harmonic generation process, HHG is emerging as a realistic approach to laboratory-scale EUV/SXR experimentation.

1.4 About This Thesis

This thesis is about the coherence properties of EUV/SXR sources. A laser is the best-known example of a coherent light source. If we just compare our understanding of Nature before and after the invention of the laser, it's quite natural to have the desire for coherence in the EUV/SXR region. For reasons will be discussed in following chapters, a traditional laser is not available in EUV/SXR region. In this thesis we will begin, in chapter 2, with fundamentals of optical coherence theories, with emphasis on applications at EUV/SXR wavelengths. The following three chapters will be assigned to the three currently available coherent sources: undulator, EUV/SXR laser, and high order harmonic generation sources. For each type, the mechanism of generating EUV/SXR radiation and the factors influencing their coherence properties will be discussed. Among the potential applications, many do not require a high degree of coherence. For this reason, an additional chapter (chapter 6) will follow, discussing other types of EUV sources, largely incoherent in nature. In the final chapter, sources properties will be summarized and compared for their strengths and limits for potential applications.

Chapter 2

Optical Coherence at EUV/SXR Region

2.1 Fundamental Optical Coherence Theory

Although light is a form of wave, its frequency is usually too high for the direct detection of its instantaneous amplitude and phase. In most cases, the observable quantity is intensity, a time-averaged value: $I = c\varepsilon_0 \langle E(t)E^*(t) \rangle$, where ε_0 is the permittivity of free space, c is the velocity of light (assuming the medium is vacuum). Here (and in this thesis) the electric field is represented in scalar form E, with E^* as its complex conjugate. The brackets denote a time average (as the result of long detector response time compared to the optical frequency). For simplicity, from now on we will drop the two unimportant constants and represent intensity as $I = \langle E(t)E^*(t) \rangle$.

"Coherence" is a measure of the correlation between fields drawn from different points in space and time. To see this, we consider the field arising from two point sources. The total electric field is the sum of the fields originating from each source point, which can be represented as $E(t) = E_1(t+\tau) + E_2(t)$. A time delay τ is introduced to include the possible path difference from the observation point to the two source points. The intensity is then

$$\begin{aligned} I &= \langle E(t)E^*(t) \rangle \\ &= \langle E_1(t+\tau)E_1^*(t+\tau) \rangle + \langle E_2(t)E_2^*(t) \rangle + \langle E_1(t+\tau)E_2^*(t) \rangle + \langle E_1^*(t+\tau)E_2(t) \rangle \\ &= I_1 + I_2 + 2\,\mathrm{Re}\,\Gamma_{12}(\tau) \end{aligned} \tag{2-1}$$

The term $\Gamma_{12}(\tau) = \langle E_1(t+\tau)E_2^*(t) \rangle$ is called mutual coherence function [17], determining whether or not pronounced interference effect will occur. The normalized form of $\Gamma_{12}(\tau)$,

$$\gamma_{12}(\tau)=\frac{\langle E_1(t+\tau)E_2^*(t)\rangle}{\sqrt{\langle|E_1|^2\rangle}\sqrt{\langle|E_2|^2\rangle}} \tag{2-2}$$

is called the complex degree of coherence, a fundamental quantity in the optical coherence theory. Using $\gamma_{12}(\tau)$, Eq. (2-1) can be represented as

$$I=I_1+I_2+2I_1I_2\,\mathrm{Re}\,\gamma_{12}(\tau)=I_1+I_2+2I_1I_2|\gamma_{12}(\tau)|\cos(\alpha_{12}(\tau)) \tag{2-3}$$

From Eq. (2-2) and Schwarz's inequality, $|\gamma_{12}(\tau)|$ is limited to a range of $0\le|\gamma_{12}(\tau)|\le 1$. One extreme, $|\gamma_{12}(\tau)|=0$, corresponds to the **incoherent** case, where electric fields are uncorrelated and intensities simply add. The other extreme, $|\gamma_{12}(\tau)|=1$, corresponds to the **coherent** case, where the intensity shows the strongest constructive or destructive interference effect (depending on the phase angle α). In reality, the degree of coherence is generally somewhere between the two extremes, and is referred to as **partially coherent**.

Please notice that the coherence discussed in this thesis is limited to the classical description of light field (electrical field E representation, with associated amplitude and phase) and the correlation between the electric fields. This is sufficient for the applications we are interested in, where the final results are always related to the intensity distribution, for example image formation in microcopy and lithography, or time-integrated reading of interference patterns. In those cases, the influence of coherence can be well studied using the concept of a mutual coherence function, as described in Eq. (2-1). More complete theory also includes higher order coherence, for example the correlation between intensities, and coherence under the quantum description of light, in forms of annihilation and creation operators. Such advanced topics can be found in the books listed in Refs. [18, 19], and the references therein.

A comprehensive description of the coherence properties of light will require the information of $\gamma_{12}(\tau)$ between any two points in the space-time domain. The coherence

properties of two points separated in **time** and of those separated in **space** are usually treated separately. The former is called **temporal coherence** and the later **spatial coherence**. They are discussed in detail in following sections.

2.1.1 Temporal Coherence and Coherence Time

Temporal coherence can be illustrated with the help of a Michelson interferometer. In it, light from a point source S is divided by a beam splitter. Each beam goes through one arm of the Michelson interferometer, and they are reunited at the detector. By moving M_1, a path difference of h can be introduced between the two arms.

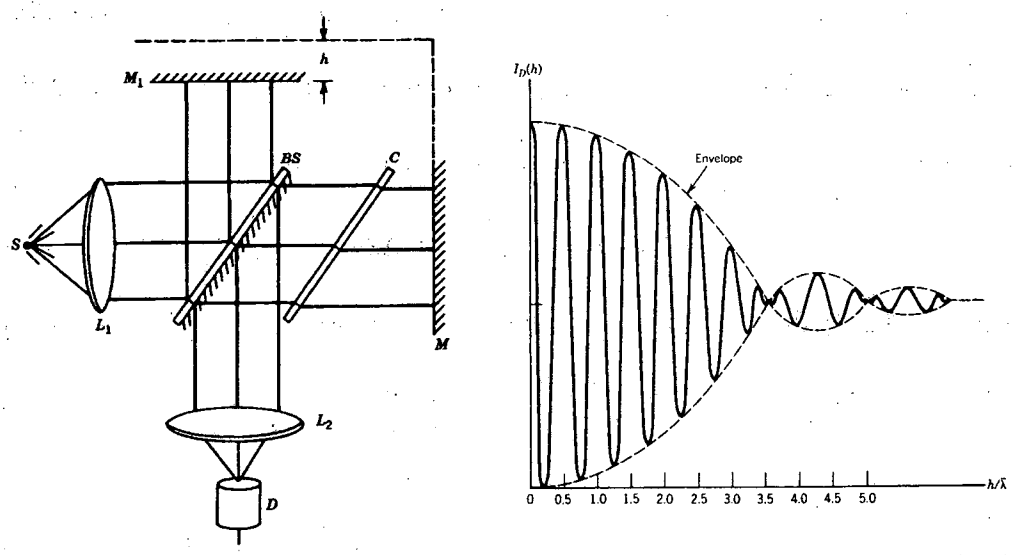

Figure 2-1. Temporal coherence illustrated by means of a Michelson interferometer. For incident light with relatively broad bandwidth, large modulation in the detected intensity can only be observed within a short range of path length difference h. Following Ref. [20].

Assuming that the light is equally divided and that the only difference between the two arms is a time delay of $\tau = h/c$. The incident electric field on the detector is then $E(t+\tau)+E(t)$,

with the subscript 1 and 2 removed since they are both from the same point source S. From Eq. (2-1), the detected intensity will be $I(\tau) = 2I_0 + 2\,\mathrm{Re}\,\Gamma(\tau)$, where I_0 is the intensity if only one arm is present. Besides the invariable term $2I_0$, the intensity will show an h-dependent modulation through the term $\Gamma(\tau)$ (See Fig. 2-1). The modulation term, $\Gamma(\tau) = \langle E(t+\tau)E^*(t)\rangle$, is by definition the autocorrelation function of E(t). From the Fourier transform theorem regarding autocorrelation [21], the Fourier transform of $\Gamma(\tau)$ will give the power spectral density (spectrum) of the source. This is in fact the basis of Fourier transform spectroscopy [22]. What interests us here is the general uncertainty relationship associated with any Fourier-transform pair, which in this case means $\Delta\tau \cdot \Delta\nu \sim 1$, where $\Delta\nu$ is the spectral bandwidth, and $\Delta\tau$ is the time range in which $\Gamma(\tau)$ is non-trivial. Since $\Gamma(\tau) \to 0$ means the disappearance of interference effect, we can define a coherence time τ_c as $\tau_c = 1/\Delta\nu$. The corresponding path length

$$L_c = c\tau_c = c/\Delta\nu = \lambda^2/\Delta\lambda \tag{2-4}$$

is called the (longitudinal) coherence length. This can also be explained in a more straightforward way, as shown in Fig. 2-2 and the reference therein.

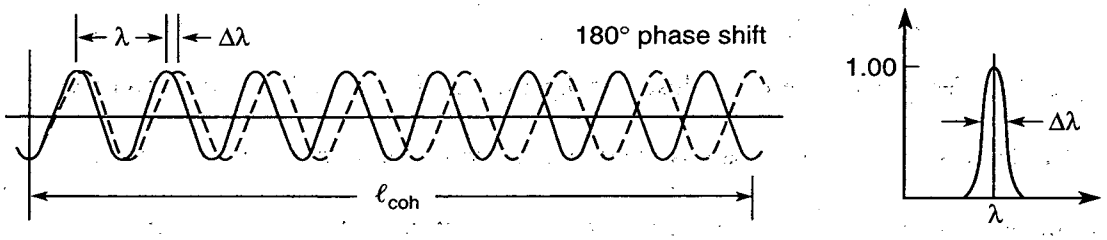

Figure 2-2. Longitudinal coherence length and the spectral bandwidth. Detailed explanations are given in Ref. 23.

From the above discussion, full temporal coherence has to be associated with a strictly monochromatic light with a δ-function spectrum. This is obviously impossible in reality since such a source would have to be a perfect single frequency oscillator lasting forever. More realistically, if the maximum optical path difference in an optical system is set to be less than the coherence length of the light, we can consider the radiation to be temporally coherent. Moreover, if an application needs longer coherence time/length than a source can support, a monochromator can be used to narrow the source's natural spectral bandwidth. The efficiency of such a spectral filter is

$$\eta = \frac{B.W._{coh}}{B.W._{source}} \cdot \eta_{optics} \tag{2-5}$$

where $B.W._{coh}$ is the bandwidth to be considered narrow enough for good temporal coherence, $B.W._{source}$ is the natural bandwidth of the source, and η_{optics} is the efficiency of the optics used in the monochromator, including factors such as absorption, scattering losses, etc.

2.1.2 Spatial Coherence and Coherence Area

Temporal coherence is sometimes called self-coherence, since it's about the ability of the field at one point (in space) to interfere with itself delayed (or advanced) by some time. Spatial coherence, on the other hand, is about the correlation between the fields at two points in space. The concept of spatial coherence can be illustrated by Young's interference experiment. To separate the influence of temporal coherence, we assume the light source is quasi-monochromatic, i.e. $\Delta\lambda << \lambda$.

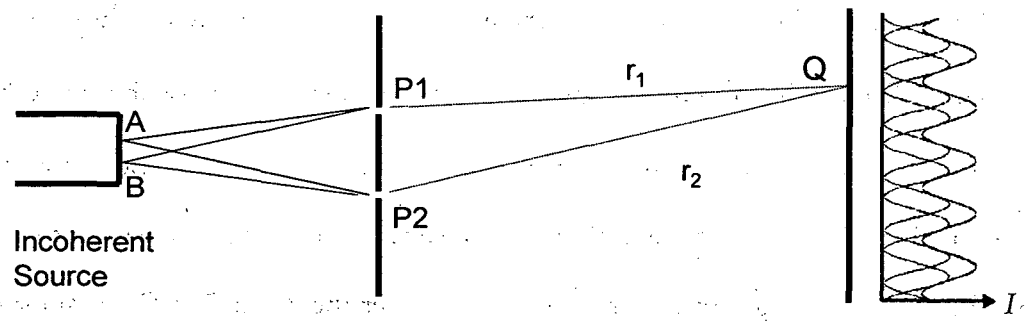

Figure 2-3. Spatial coherence illustrated by Young's interference experiment.

It's well known that by using a point source, Young's experiment shows high contrast periodic bright-dark pattern at the observation screen as a result of the interference between light passing through the two pinholes P_1 and P_2. However, if the pinholes are illuminated by an extended incoherent source (a thermal source, for example), the fringe becomes less visible. This can be explained as following: each of the source points (e.g. A and B in the figure) produces its own set of high contrast interference pattern. Since the source is incoherent, the final pattern will simply be the sum of all these interference patterns. The exact position of the maximum and minimum of each set is different, thus the sum of the intensity patterns will show lower contrast.

More formal analysis of the fringe contrast leads us to the concept of spatial coherence. The electric field at a point Q on the screen is the sum of the diffracted fields from the two pinholes. It can be expressed as

$$E_Q(t) = K_1 E_1(t - \frac{r_1}{c}) + K_2 E_2(t - \frac{r_2}{c})$$

where K_1 and K_2 are factors associated with diffraction and propagation, and are pure imaginary [17, 20] in the case of pinhole diffraction. Knowing this, the intensity at point Q can be expressed in a manner similar to that in Eq. (2-3) as

$$I_Q = I_1 + I_2 + 2\sqrt{I_1 I_2}\,\mathrm{Re}\,\gamma_{12}(\frac{r_2 - r_1}{c}) \tag{2-6}$$

where $I_{1(2)} = \left|K_{1(2)}\right|^2 \left|E_{1(2)}\right|^2$ is the intensity at point Q if only one pinhole is present. For quasi-monochromatic light, and with maximum path difference less than the temporal coherence length, the τ -dependence of $\gamma_{12}(\tau)$ can be simplified to [17]:

$$\gamma_{12}(\tau) = \gamma_{12}(0)e^{-2\pi i\nu\tau} = \mu_{12}e^{-2\pi i\nu\tau} \tag{2-7}$$

where υ is light frequency and $\mu_{12} = \gamma_{12}(0)$ is called complex coherence factor. Since $|\mu_{12}| = |\gamma_{12}(0)|$, $|\mu_{12}|$ is also in the range of $0 \le |\mu_{12}| \le 1$, thus another measure of the degree of coherence. Using μ_{12}, Eq. (2-6) becomes

$$I_Q = I_1 + I_2 + 2\sqrt{I_1 I_2}|\mu_{12}|\cos(\beta_{12} - k(r_2 - r_1)) \tag{2-8}$$

where k=2π/λ. Here we retrieve the well-known periodic fringes through the last term, where $\beta_{12} = \arg(\mu_{12})$ can be regarded as the initial phase difference between the two pinholes. The normalized degree of coherence $|\mu_{12}|$ is related to the visibility of the fringes:

$$V = \frac{I_{Q,MAX} - I_{Q,MIN}}{I_{Q,MAX} + I_{Q,MIN}} = \frac{2\sqrt{I_1 I_2}}{I_1 + I_2}|\mu_{12}| \tag{2-9}$$

When I_1=I_2, this becomes a simple relationship, $V = |\mu_{12}|$, which has been used to evaluate the degree of coherence in the classical Thompson-Wolf experiments [24]. It will also be used to explain experiments in the next several chapters.

The exact form of complex coherence factor μ_{12} from an incoherent source is investigated and mathematically expressed by the van Cittert-Zernike theorem [25]. It states that the complex coherence factor between two points at a plane some distance (z) away from an incoherent source can be obtained by the Fourier transformation of the source intensity

distribution: (See Fig. 2-4 for geometry illustrations)

$$\mu_{OP} = \frac{e^{-i\psi} \iint I(\xi,\eta)\exp[i2\pi(\xi x+\eta y)/\lambda z]d\xi d\eta}{\iint I(\xi,\eta)d\xi d\eta} \tag{2-10}$$

The phase term $e^{-i\psi}$, with $\psi = k\frac{x^2+y^2}{2z}$, is a pure geometrical term that does not influence the value of $|\mu_{OP}|$, the degree of coherence.

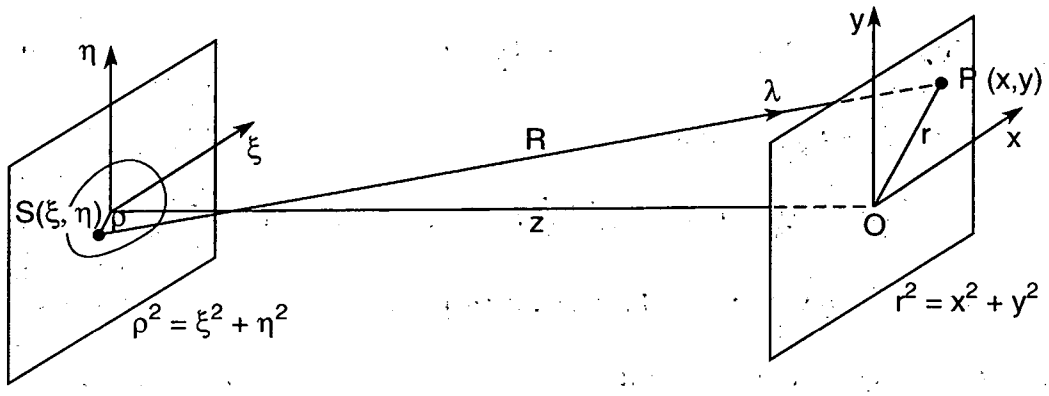

Figure 2-4. Geometry used in illustrating the van Cittert-Zernike theorem. [23]

The van Cittert-Zernike theorem explains the decrease of fringe visibility when using an extended incoherent source. The intuition of perfect spatial coherence from a point source, whose intensity distribution can be described as a δ-function, can also be easily obtained from it. One of the most important applications of the van Cittert-Zernike theorem is that it states the existence of an area of coherence even with an incoherent source. Here we take a Gaussian incoherent source as an example. Assume the radius (rms) is a: $I = I_0 e^{-\rho^2/2a^2}$. Using Eq. (2-10), the coherence function is found to be also Gaussian: $|\mu_{OP}| = e^{-(kar/z)^2/2}$.

Therefore, we can define a transverse coherence length at distance z as $R_c(z) = z/ka$, within which the degree of spatial coherence is high ($e^{-1/2} = 0.61$). An aperture with this size can be used as a spatial filter to pass through spatially coherent light. In EUV/SXR spectral region most sources are at best partially coherent. The van Cittert-Zernike theorem provides a very useful approach to obtain light with very high degree of spatial coherence. This spatial filter is by nature a phase-space product filter, as will be discussed in next section.

2.1.3 Phase-Space Product, Brightness and Coherent Power (Flux)

In previous paragraph, the transverse coherence length scales linearly with the distance z, implying more suitable description than coherence area is in fact a solid angle, roughly with its extent in angular space as $\Delta\Omega = A_c / z^2$. This can be further expressed as $\Delta A \cdot \Delta\Omega = \lambda^2$, with ΔA representing extent of source area. The product of area and solid angle, $\Delta A \cdot \Delta\Omega$, is called phase-space product. This shows an interesting result that good spatial coherence exists in a phase space $\sim \lambda^2$, even if the source is totally incoherent.

The minimum phase-space product occupied by any light beam, regardless of its coherence, is in fact also $\sim \lambda^2$. Let's first examine a beam in the lowest order Hermite-Gaussian mode (TEM_{00}). Intensity distributions at both its waist and far-field are Gaussian profile: $I_w \propto \exp(-r^2/2r_0^2)$ and $I(\theta) \propto \exp(-\theta^2/2\theta_0^2)$, with $r_0 \cdot \theta_0 = \lambda/4\pi$. The phase-space product of TEM_{00} mode is $\Delta A \cdot \Delta\Omega = 2\pi r_0^2 \cdot 2\pi\theta_0^2 = (\lambda/2)^2$. (The factor of 2π comes from the normalization of a Gaussian function). In fact, it can be proven that this lowest order Hermite-Gaussian mode has the minimum phase-space product [26]. Knowing this, the

good spatial coherence within a phase-space product of $\sim \lambda^2$ is understandable, since such a small phase-space product can contain only very few spatial modes.

Based on the concept of phase-space product, a commonly used parameter for characterizing light beam is brightness, defined as $B = \frac{F}{\Delta A \cdot \Delta\Omega}$, where F is the photon flux, in units of photons per second. Brightness is a conserved quantity in a lossless optical system. In many cases brightness is a more appropriate measure than the integrated total flux for representing the real "strength" of a source. From the discussion in the previous paragraph, with a source of known brightness B, we can define a spatially coherent flux

$$F_{sp.coh} \geq B(\frac{\lambda}{2})^2 \tag{2-11a}$$

It is slightly different from the one commonly used in most literatures:

$$F_{sp.coh} = B(\frac{\lambda}{2})^2 \tag{2-11b}$$

The reason for the inequality is that the spatially coherent flux should be **at least** $B(\lambda/2)^2$, since (as mentioned before) $(\lambda/2)^2$ is a **minimum** phase-space product, which can only be realized for the TEM_{00} mode. In general, other spatial modes will have larger phase-space product and the use of $F_{sp.coh} = B(\frac{\lambda}{2})^2$ will underestimate the spatially coherent flux. To see this, let us consider diffraction by a circular aperture. Assuming uniform plane wave illumination, the angular distribution is the well-known Airy pattern [27]. The aperture serves as a coherent source, thus $F_{sp,coh} = F_{total}$. The distribution of the flux at source plane and far field can be expressed as

$$\frac{dF}{dA} = \frac{F}{\pi a^2} \quad \text{and} \quad \frac{dF}{d\Omega} = \frac{F}{4\pi/(ka)^2}\left[\frac{2J_1(ka\theta)}{ka\theta}\right]^2$$

The normalization factors ensure $\iint \frac{dF}{dA} dA = \iint \frac{dF}{d\Omega} d\Omega = F$. The brightness is then

$$B = \left. \frac{d^2F}{dAd\Omega} \right|_0 = \frac{F}{\pi a^2 \cdot 4\pi/(ka)^2} = \frac{F}{\lambda^2}$$

Now we have an example of $F_{sp.coh} = B(\lambda)^2$, four times larger than that would have been obtained using the minimum phase-space product of $(\lambda/2)^2$. As a result, Eq. (2-11b) can be regarded as a conservative estimate, or the lower limit of spatially coherent photon flux.

As discussed in the previous section, full spatial coherence, in reality, is related to a single spatial mode. We can then define spatially coherence power (photon flux) as the power (photon flux) contained in one spatial mode. A partially coherent source excites multiple spatial modes and it is generally difficult to realize effective separation of those modes. In this case, the direct approach is to build a filter with limited phase-space product so that the lowest mode, with smallest phase-space product, can pass through with little loss while higher modes are mostly blocked. As an example, we investigate one such filter using a pinhole and an angular aperture. (See Fig. 2-5.) The pinhole serves as the source filter, limiting the size of the source. The angular aperture limits the accepted solid angle.

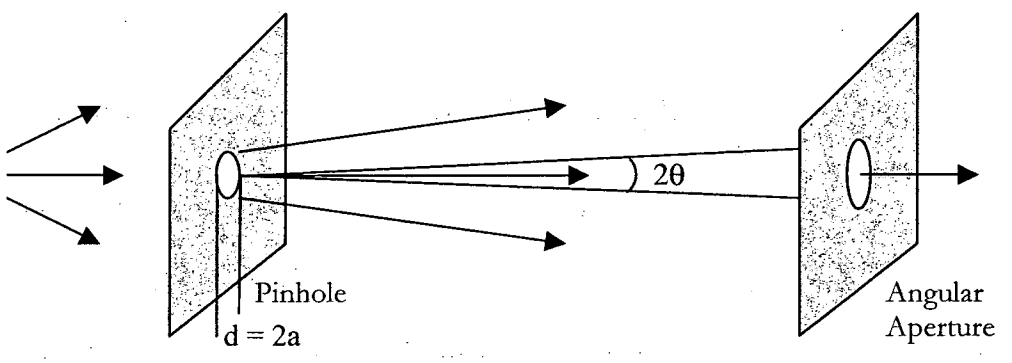

Figure 2-5. A spatial filter limiting the phase-space product to $a \cdot \theta = \lambda/2\pi$ can be used to provide light with high spatial coherence.

Assume the incoming light is of low spatial coherence (many modes), the pinhole is essentially an incoherent source. Appling the van Cittert-Zernike theorem to this incoherent source with radius a, one finds that with the limitation of $a \cdot \theta = \lambda/2\pi$, the degree of coherence within the range of angular aperture satisfies $|\mu_{OP}| > 0.88$, a criteria usually used as a measure of full spatial coherence [17]. The phase-space product of this filter is $\pi a^2 \cdot \pi\theta^2 = (\lambda/2)^2$. This demonstrates the use of Eq. (2-11b) for the calculation of spatially coherent power with a largely incoherent source. As indicated earlier, a coherent circular pinhole source will occupy a phase-space product of λ^2, thus this spatial filter sacrifices some coherent flux to keep the degree of coherence high. Clearly, opening up the θ-filter can pass more coherent flux (since $|\mu_{OP}|$ is still fairly high), but doing so also inevitably allows more incoherent radiation from other modes to pass. Thus there exists a compromise between the degree of coherence and flux throughput when using such spatial filters. Depending on the level of acceptable coherence, the coherent flux, if defined as the output from such filters, can vary. For consistency, we will only use Eq. (2-11b), for both the theoretical consideration and its relatively easy realization in practice by simple pinhole aperture filters.

The minimum phase space also sets an upper limit of the brightness of a source if its total flux is known: $B \le \frac{F_{sp,coh}}{(\lambda/2)^2} \le \frac{F_{total}}{(\lambda/2)^2}$. This is important when calculating the brightness of a near "point" source, as will be encountered in chapter 3 for calculating the brightness of undulator radiation generated by a single electron. The minimum phase-space product means that a point source can not be arbitrarily small. This is consistent with the uncertainty principle: the position of a photon has to carry some degree of uncertainty, since the photon's momentum uncertainty can not be infinite in a physical light beam. Generally a

diffraction-limited source size should be associated with a beam having limited angular spread, as will be employed in chapter 3, section 3.2.3.

Another widely used parameter is the spectral brightness, $B_{\Delta\varpi/\omega} = \frac{F_{\Delta\varpi/\omega}}{\Delta A \cdot \Delta\Omega}$, usually in units of photons/s/(mm)^2/(mrad)^2/0.1%bandwidth. Including the effect of spectral bandwidth, spectral brightness is more closely related to the source's ability to generate both temporally and spatially coherent radiation. As an example, we relate a source's spectral brightness B to the photon degeneracy parameter. The photon degeneracy parameter is the number of photons within a coherence volume (having both good spatial and temporal coherence), a critical parameter for nonlinear multi-photon experiments. The spatially coherent part is described by Eq. (2-11b) above. The longitudinal coherence length given by Eq. (2-4) is L_c = 1000λ (for 0.1%B.W.). The corresponding coherence time, τ_c, is $\tau_c = L_c/c$. Including the limitation of longitudinal coherence, the degeneracy parameter, for spatially coherent photon flux within the coherence time, is:

$$g = B(\frac{\lambda}{2})^2 \cdot \frac{1000\lambda}{c}$$

A high degeneracy parameter is a figure of merit for highly coherent radiation. For example, the degeneracy parameter of a 1mW single mode He-Ne laser is about 10^9, while in the EUV/SXR region, it is usually less than 1 with currently available sources.

2.2 Importance of Characterizing the Coherence Properties of Sources

The importance of characterizing the coherence properties of sources is two-fold. On one hand, it provides more understanding of the physics behind the generation process. This is especially true and important in the EUV/SXR region where conventional lasers are not

available (see next section). At this point in time each type of source intended for generating coherent radiation is based on relatively new and immature techniques. Experiment measures of their coherence properties help to verify and improve our understanding of these techniques. On the other hand, knowledge of source coherence properties is essential to properly match sources with particular applications, since the influence of coherence to applications can be very significant.

Applications like interferometry and holography obviously need a high degree of coherence. Such applications depend on the production of high contrast interference patterns to obtain desired information. Diffraction-limited propagation and focusing also require a high degree of spatial coherence since they both imply a minimum phase-space product. For such applications, highly coherent sources are desire, or adequate (temporal and/or spatial) filters can be used to generate necessary coherence based on the knowledge of the source's brightness, spectral bandwidth, etc.

On the other hand, an excessive degree of coherence is deleterious for many applications, particularly for imaging systems, such as in microscopy and lithography. Recent advances in optical technology and engineering have pushed the resolution of modern imaging systems to their physical limits. The physical limit of resolution of a microscope is known to explicitly depend on the coherence of illumination, with the best resolution achieved with partial coherence (between the extremes of incoherent and coherent illumination) [17]. The partial coherence has been used to improve the spatial resolution of a SXR microscope [28], and is major design consideration of modern lithography systems [29].

Partially coherent illumination, characterized by a factor σ defined as $\sigma = NA_{cond} / NA_{obj}$, is determined by the numerical apertures of condenser (illumination optics) and objective (imaging lens) [17, 29]. It can be controlled by designing different illumination-imaging

schemes. The definition of partial coherence factor based on the numerical apertures is in fact obtained by applying van Cittert-Zernike theorem to the condenser, assuming an essentially incoherent source. Such a definition will be invalid when using a source with full or very good spatial coherence. More generally, the effective value of σ may need revision based on the knowledge of the source's own coherence properties. Therefore, in cases where controlled coherence plays a critical role, knowing the sources' coherence properties is especially important.

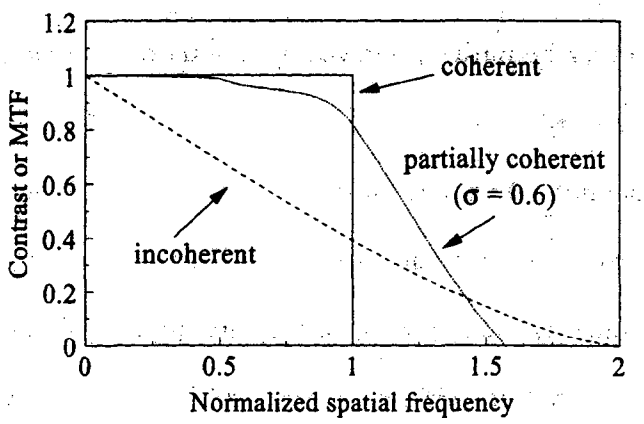

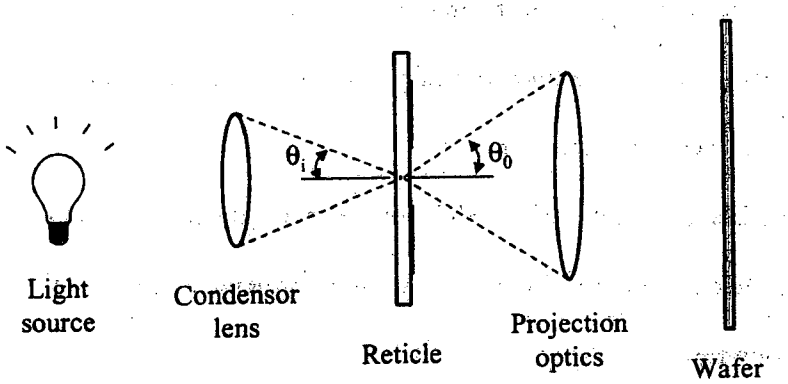

Figure 2-6. (Top) Effect of partial coherence factor σ on an imaging system's response to different spatial frequency. (Bottom) In an optical lithography system, the partial coherence factor is controlled by the numerical apertures of condenser lens and projection optics. The light source is largely incoherent. (Following Ref. 29)

2.3 Generating Coherent Radiation at EUV/SXR Region

The conventional method of generating coherent visible light is well known: through a laser. Good spatial coherence is achieved by imposing light oscillation in a cavity supporting a single transverse mode (this can be either achieved by the geometry of the cavity, or by using a pinhole as the transverse mode selector). The cavity and pinhole are critical for limiting the phase-space product to $\sim\lambda^2$ scale, ensuring high degree of spatial coherence. Good temporal coherence is a consequence of the combination of laser transition's narrow linewidth and cavity resonance, and can be further improved by an intra-cavity longitudinal mode selector (e.g., an etalon) if necessary.

Unfortunately we can not at this time build such a laser for use in the EUV/SXR spectral region, mainly due to the impracticality of a cavity. Even multilayer mirrors are of high enough quality at some wavelength regions, they are usually vulnerable to damage from debris and high radiation from plasmas, which are the necessary lasing media at short wavelengths. The extremely short lifetime of plasmas (unavoidable with their high temperature) also makes oscillation basically end within very few round trips, too little to build up desired wave field characteristics.

Without a true laser, currently EUV/SXR sources generally produce only partially coherent light. Among them, there are three approaches to generate radiation with relatively good coherence properties:

1) Undulator Radiation

Undulator radiation is one form of synchrotron radiation that is particularly designed to generate high spectral brightness radiation. As discussed above, high spectral brightness implies good coherence properties, and can "afford" further filtering to provide highly

coherent light with useful power. Chapter 3 will detail the spectral and spatial distributions of undulator radiation. The brightness and coherent power from typical undulators in modern synchrotron facilities will be calculated. The influence of electron beam parameters on the performance of undulators will be emphasized.

2) EUV/SXR laser

EUV/SXR lasers are similar to conventional lasers in many aspects, but without the cavity for reasons discussed above. Hot-dense plasmas are the gain media (population is inverted for a particular transition) and light is amplified by stimulated emission. For this reason, an EUV/SXR laser qualifies to be called a laser, since it indeed satisfies "Light Amplification by Stimulated Emission of Radiation". The temporal coherence of the short wavelength laser is usually good, since the lasing linewidth is quite narrow. But without a cavity, the spatial coherence of EUV/SXR lasers is generally quite poor. In fact, the EUV/SXR laser radiation is in nature built up from spontaneous emission within the initially incoherent source. Fortunately, the radiation from an incoherent source is not necessarily of poor spatial coherence. In the case of EUV/SXR laser, the improvement of coherence can happen in the amplification process. Under certain circumstances (usually closely related to the geometry of the plasma), the laser output is dominated by few spatial modes that experienced largest gain. The small number of spatial modes implies good spatial coherence. In chapter 4 we will show one such example, where the total number of spatial modes of an EUV laser is significantly reduced by intrinsic mode selection mechanisms, resulting in an essentially full spatial coherence.

3) High Harmonic Generation (HHG)

HHG is probably the most promising way of generating coherent EUV/SXR. Beginning with a fully coherent field (from the IR pump laser), HHG is also a coherent process with

the light-atom interaction fully deterministic. HHG sources have shown fairly good coherence properties in previous experiments, however the excellent coherence properties of the pump laser were not fully preserved [30]. In chapter 5, factors that degrade the coherence will be discussed, with possible solutions to minimize these effects. The experimental results of a fully spatially coherent EUV beam from a HHG source will be presented.

Chapter 3

Undulator Radiation

3.1 Undulator Radiation Basics

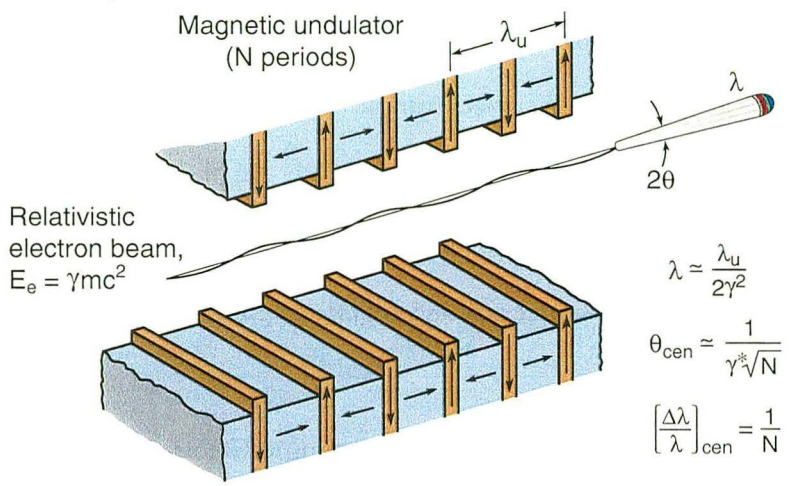

Figure 3-1. Undulator radiation is generated by relativistic electrons traversing a periodic magnet structure with moderate field strength. [31]

Undulator is one form of insertion devices used in synchrotron radiation facilities. It consists of a periodic magnet structure with modest field strength. A relativistic electron traversing an undulator undergoes a small amplitude oscillation (thus the name undulator) and radiates. Strong Doppler shift associated with the relativistic motion helps to generate very short wavelengths, a factor of $2\gamma^2$ shorter than that of the undulator period. Here

$$\gamma = E_e / mc^2 = 1957 E_e(GeV)$$

where E_e is the electron's kinetic energy and mc^2 = 0.511 MeV its rest energy. With E_e typically ranging from about 1 to 10 GeV (corresponding to γ from 2000 to 20,000), the factor of $2\gamma^2$ efficiently connects the typical centimeter scale undulator period to radiations

in EUV/SXR and even shorter wavelengths. Moreover, undulators are optimized to generate radiations with very high spectral brightness by intentionally limiting the strength of the magnetic fields. The constrained small amplitude oscillation prompts interesting interference effects, effectively squeezing the radiation into a rather discrete spectrum (in contrast to the continuum spectrum from other devices, like bending magnet and wiggler) and a narrower radiation cone. As a result, undulator radiation can provide respectable power with good temporal coherence (for its narrow spectral bandwidth) and spatial coherence (for its limited phase-space product) [32]. In the following sections, we will quantitatively investigate the undulator radiation, with close attentions to coherence-related properties, such as spectrum, source size and angular distribution of the radiation.

3.2 Properties of Undulator Radiation by a Single Electron

In this section we will examine the radiation generated by an electron passing through a typical planar undulator, which has a magnetic field distribution of the form

$$\vec{B}(z) = B_y \overrightarrow{e_y} = B_0 \cos(\frac{2\pi}{\lambda_u} z)\overrightarrow{e_y} = B_0 \cos(k_u z)\overrightarrow{e_y}$$

where λ_u is the magnetic field period and k_u the corresponding wave number. (See figure 3-2)

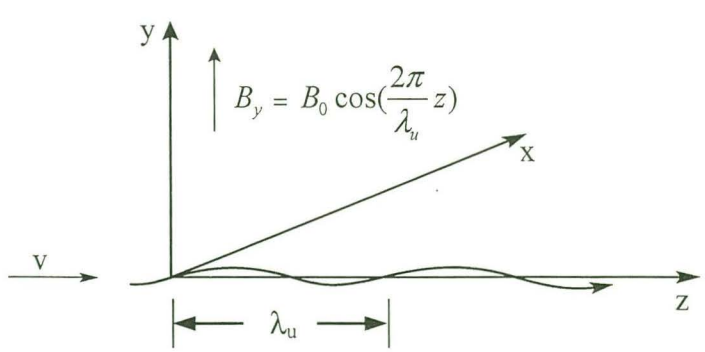

Figure 3-2. Coordinate system describing electron motion in a planar undulator.

The approach here follows that in chapter 5 of Ref. [1]. For brevity, we will only keep the important results and definitions of parameters for the sake of further discussions.

As a result of the Lorentz force, the electron's oscillation in x-direction can be expressed as

$$v_x = \frac{Kc}{\gamma}\sin(k_u z) \tag{3-1}$$

where

$$K = \frac{eB_0\lambda_u}{2\pi mc} = 0.9337 B_0(T)\lambda_u(cm) \tag{3-2}$$

is referred to as the deflection parameter, one of the most important parameters for undulator radiation. For $K \leq 1$, the maximum excursion angle of the electron's trajectory ($\tan^{-1}(v_x/v_z)$; with $v_z \sim c$, it is approximately K/γ) is smaller than the natural opening angle of synchrotron radiation $1/\gamma$. As a result, radiations from all points in the trajectory have good overlap and their interferences enhance the radiation at some particular wavelengths (resulting in a discrete spectrum) and within a narrower emission angle. The radiation produced at the weak field limit ($K \leq 1$) is called undulator radiation, having very high spectral brightness and, as a result, good coherence properties. On the strong field limit ($K \gg 1$), it's called wiggler radiation, which is essentially an incoherent sum of the radiations from all periods. Wiggler radiation possesses higher power, but distributed in a near-continuum spectrum and a larger radiation cone. It will be briefly discussed in chapter 6 as one form of incoherent sources.

Undulator radiation (under weak field condition) can be studied in a simple yet very helpful manner with the help of a moving frame of reference, whose velocity (relative to the lab frame of reference) is the average velocity of the electron's motion in z-direction. Since Lorentz force doesn't change the absolute value of the electron's velocity, we have

$$v_x^{\ 2} + v_z^{\ 2} \equiv v^2 = \beta^2 c^2$$

where $\beta \equiv v/c$, and is related to γ as $\gamma = 1/\sqrt{1-\beta^2}$. For our cases, $\beta \approx 1$ and $1-\beta \approx 1/2\gamma^2$.

Using Eq. (3-1) and these approximations, we have

$$\frac{v_z}{c} = 1 - \frac{1+K^2/2}{2\gamma^2} + \frac{K^2}{4\gamma^2}\cos(2k_u z) \tag{3-3}$$

Under the assumption K $\ll$ 1, we average the oscillation term and approximate the z-motion of the electron to be a constant velocity drift:

$$v_z \approx \overline{v_z} = \beta^* c = (1 - \frac{1+K^2/2}{2\gamma^2})c = (1 - \frac{1}{2\gamma^{*2}})c$$

where we obtain the effective relativistic factor

$$\gamma^* \equiv \frac{\gamma}{\sqrt{1+K^2/2}} \tag{3-4}$$

The motion of the electron can then be simplified to

$$x = \frac{K}{\gamma\beta^* k_u}\sin(\omega_u t);\ z = \beta^* ct$$

where $\omega_u = \beta^* c k_u \approx c k_u$. In the moving frame of reference, with a velocity of $\beta^* c$, the electron's motion has a very simple form after Lorentz space-time transformations:

$$x' = x = \frac{K}{\gamma\beta^* k_u}\sin(\omega_u t) = \frac{K}{\gamma\beta^* k_u}\sin(\omega_u \gamma^* t');\ z' = 0$$

With K$\ll$ 1, this constitutes a well-behaved single frequency ($\omega' = \gamma^* \omega_u$) dipole radiation, with radiation power and angular distribution can both be readily obtained:

$$\frac{d\overline{P}'}{d\Omega'} = \frac{e^2 c \gamma^2 K^2}{8\varepsilon_0 \lambda_u^2 (1+K^2/2)^2}\sin^2\Theta'$$

where prime denotes quantities in moving frame and the cap denotes time average value. It has the well-known $\sin^2\Theta'$ dipole radiation pattern.

Back to the lab frame, a stationary observer will see much higher radiation frequencies due to Doppler effect. The Doppler shift is angular dependent:

$$\omega = \frac{\omega'}{\gamma^*(1-\beta^*\cos\theta)}$$

With $\omega' = \gamma^* \omega_u$ and expanding $\cos\theta$ at small θ, we get the important result of the angular-dependent wavelength of undulator radiation:

$$\lambda = \frac{\lambda_u}{2\gamma^{*2}}(1+\gamma^{*2}\theta^2) \tag{3-5}$$

It implies that shortest wavelength (highest photon energy) will be observed on-axis, while the wavelength becomes longer at off-axis angles. The on-axis wavelength is

$$\lambda_0 = \frac{\lambda_u}{2\gamma^{*2}} = \frac{\lambda_u}{2\gamma^2}(1+\frac{K^2}{2}) \tag{3-6}$$

This provides a tuning mechanism for undulator radiation through varying the K value, usually achieved by opening/closing the gap of the magnetic structure (thus changing the magnetic field strength B_0). The radiation pattern, after transforming $\sin^2\Theta'$ to the lab frame, can be found to be highly concentrated on the forward direction:

$$\left.\frac{d\overline{P}}{d\Omega}\right|_{e^-} = \frac{e^2cK^2\gamma^4}{\varepsilon_0\lambda_u^2(1+K^2/2)^3}\left[\frac{1+2\gamma^{*2}\theta^2(1-2\cos^2\phi)+\gamma^{*4}\theta^4}{(1+\gamma^{*2}\theta^2)^5}\right] \tag{3-7}$$

The additional notation of e- serves as a reminder that this is for a single electron.

3.2.1 Central Radiation Cone

For undulator radiation, the radiation within the **central radiation cone** is usually the most useful part of the radiation. The central radiation cone angle, θ_{cen} is defined as

$$\theta_{cen} = \frac{1}{\gamma^*\sqrt{N}} \tag{3-8}$$

The radiation spectrum within a small collection angle comparable to θ_{cen} is rather simple. When $\theta \sim \theta_{cen}$, the angular-dependent term in Eq. (5-7) has a small relative variation in the order of 1/N, therefore can be dropped to a good accuracy since N ≫ 1. This gives

$$\left.\frac{d\overline{P}}{d\Omega}\right|_{e^-} = \frac{e^2 c K^2 \gamma^4}{\varepsilon_0 \lambda_u^2 (1+K^2/2)^3} = C_1(\text{constant}) \tag{3-9}$$

From Eq. (3-5), radiation within a narrow spectral bandwidth (from λ to λ+dλ) can only be found within a ring region in the angular space (from θ to θ+dθ). (See figure 3-3) The solid angle occupied by this ring is $d\Omega = 2\pi \sin\theta d\theta = 2\pi\theta d\theta$. From Eq. (3-5), we have $d\lambda = \lambda_u \theta d\theta$. Combining them, we get

$$d\Omega / d\lambda = 2\pi / \lambda_u (\text{constant})$$

Since Eq. (3-9) gives $d\overline{P}/d\Omega$ = constant, we find the spectrum has a simple profile with $d\overline{P}/d\lambda$ = constant. Within θ_{cen}, the spectrum is a flat-top square with sharp cutoff at λ_0 and $\lambda_0(1+1/N)$.

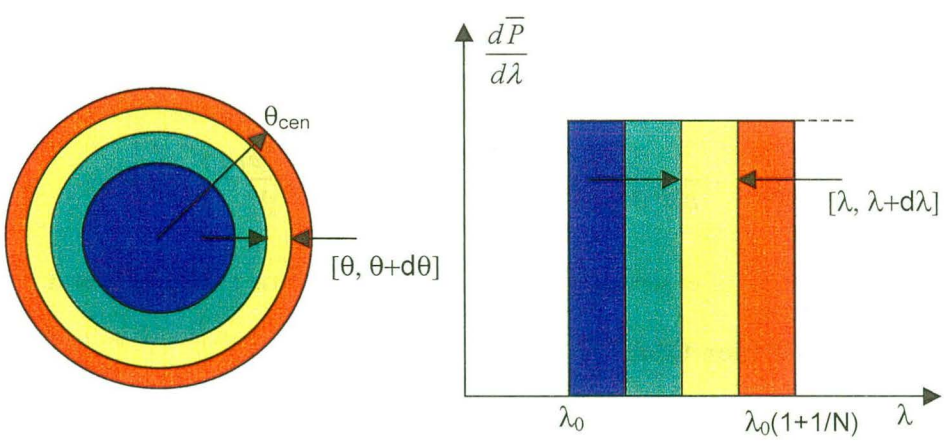

Figure 3-3. Angular-dependent wavelength of undulator radiation. Wavelength is shortest on-axis and become longer off-axis. Central radiation cone corresponds to a wavelength (relative) increase of 1/N.

Power in the central radiation cone, $\overline{P}_{cen}$, is of fundamental importance to undulator radiation. At this point we ignore the difference between individual electrons (it will be discussed in section 3.3) and include the contributions from all electrons in the undulator. The total number of electrons in the undulator is $N_e = IL/ec$, where I is the average beam current and $L = N\lambda_u$ is the length of the undulator. We exclude the free electron laser (FEL) situation and treat all electrons as uncorrelated. In this case, the total power contained in central radiation cone is simply the sum of the power from each electron:

$$\overline{P}_{cen} = N_e \cdot C_1 \cdot \pi\theta_{cen}^2 = \frac{\pi e \gamma^2 I}{\varepsilon_0 \lambda_u} \frac{K^2}{(1+K^2/2)^2} \qquad \text{Eq. (3-10a)}$$

Or in practical units,

$$\overline{P}_{cen} = N_e \cdot C_1 \cdot \pi\theta_{cen}^2 = (5.69\times10^{-6} W) \frac{\gamma^2 I(A)}{\lambda_u(cm)} \frac{K^2}{(1+K^2/2)^2} \qquad \text{Eq. (3-10b)}$$

Since $\overline{P}_{cen}$ is the power within 1/N relative bandwidth with flat-top spectrum, we can also get power in a narrower relative bandwidth $\Delta\lambda/\lambda$ as:

$$\overline{P}_{\Delta\lambda/\lambda} = \overline{P}_{cen} \cdot \frac{\Delta\lambda/\lambda}{1/N} \qquad \text{Eq. (3-11a)}$$

Or in practical units and in terms of photon flux,

$$\overline{F}_{\Delta\lambda/\lambda} = (1.43\times10^{17}\, ph/s) NI(A) \frac{K^2}{1+K^2/2} \cdot \frac{\Delta\lambda}{\lambda} \qquad \text{Eq. (3-11b)}$$

3.2.2 Limited Number of Oscillations

Above discussion uses a one-on-one relationship between wavelength and observation angle, as expressed in Eq. (3-5). It implies a small enough pinhole can be used to get light with arbitrarily narrow bandwidth. The sharp cut-off at the shortest wavelength is also one result of it. These seemingly unphysical results arise from the idealistic treatment that the radiation

is monochromatic in the moving frame of reference. In fact, since the electron only oscillates N cycles in the undulator, its radiation will not be perfect single frequency. This is described mathematically by the sinc^2-function associated with a harmonic oscillator:

$$\frac{I(\omega)}{I(\omega_0)} = \frac{\sin^2(N\pi u)}{(N\pi u)^2}$$

where ω_0 is the harmonic frequency and $u=(\omega-\omega_0)/\omega_0$. The full width at half maximum (FWHM) of the sinc^2 function corresponds to a relative bandwidth of 0.9/N, which can be regarded as the "natural" bandwidth of undulator radiation. This "natural" bandwidth effect has two important subsequences:

1) Spectrum broadening

Every single wavelength λ in previous section (without including the N-cycle effect) now has to be extended to a range according to the sinc^2 function. This is a homogenous broadening effect and can be treated mathematically by convolution. The convolution will round the sharp cut-off edge and give a smoothly varying spectrum. It will also set the lower limit of relative bandwidth to the "natural" bandwidth however small the collection angle is.

2) Angular distribution spreading for a particular wavelength

Another consequence of the N-cycle effect is that we'll find a particular wavelength λ not only at a particular angle θ decided by Eq. (3-5), but also in the nearby angles. At these nearby angles, the central wavelengths are not λ, but due to the "natural" bandwidth, they will also produce radiation at λ, with relative strength decided by the sinc^2 function. The profile of the angular distribution for λ_p can be deducted from the sinc^2 function as

$$\frac{d\overline{P}}{d\Omega}(\theta;\lambda) \propto Sinc^2(N\pi\frac{\lambda-\lambda(\theta)}{\lambda(\theta)})$$

where $\lambda(\theta)$ is the central wavelength at θ which can be obtained from Eq. (3-5).

These two effects arise from the same physical origin and their results can be understood better when checked together. The following two figures show the results of them:

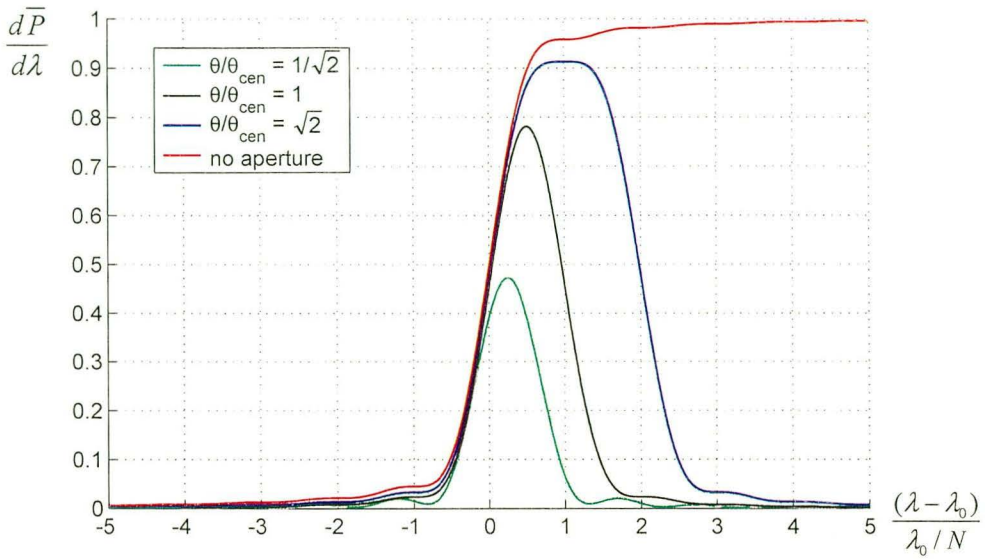

Figure 3-4 Spectrum of the radiation within different collection angles after including the effect of limited number of oscillations.

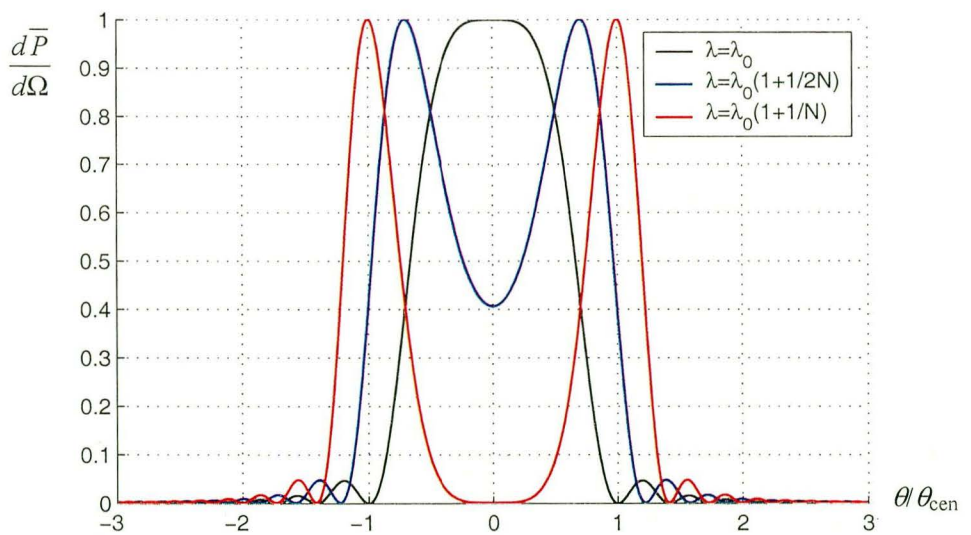

Figure 3-5. Angular distributions for several wavelengths around the central wavelength λ_0.

Fig. 3-4 shows the spectrum of the radiation through pinholes with collection angles of $1/\sqrt{2}$, 1 and $\sqrt{2}$ times θ_{cen}. For comparison, the spectrum without a pinhole is also shown. Fig. 3-5 shows the angular distributions of three wavelengths: λ_0, $\lambda_0(1+1/2N)$ and $\lambda_0(1+1/N)$.

We can get some interesting results from those two figures. First, notice the black line in Fig. 3-4, which is the spectrum in central radiation cone. (It will be used again in next section.) Comparing it with the other two spectrums, we see that a collection angle of θ_{cen} is an optimal balancing between the photon flux throughput and the spectral bandwidth. Pinhole size smaller than θ_{cen} has lower throughput while the relative bandwidth is not reduced much. Bigger pinhole permits more photon flux, however most of the flux gain comes from the contributions from the longer wavelength components, which is not necessarily a good thing because many applications require limited bandwidth. Also, a collection angle equal to θ_{cen} will be able to catch most of the available photon flux at λ_0 (compare the black line and the red line). Next, let us see the importance of the radiation at λ_0.

From Fig. 3-4, spectral density $d\overline{P}/d\lambda$ at λ_0 is only half of the maximum possible value (In the figure, $d\overline{P}/d\lambda$ is scaled to what would be obtained using Eq. (3-11)), As a result, the photon flux within some fixed narrow bandwidth $\Delta\lambda/\lambda$ at λ_0 is

$$\overline{F}_{\Delta\lambda/\lambda}\Big|_{\lambda_0} = (0.71\times10^{17}\,phs/s)NI(A)\frac{K^2}{1+K^2/2}\cdot\frac{\Delta\lambda}{\lambda} \qquad \text{Eq. (3-12)}$$

It's half of that in Eq. (3-11b). More flux (within the same bandwidth $\Delta\lambda/\lambda$) can be obtained, and approach the same value as in Eq. (3-11b) at $\lambda_0(1+1/N)$ and longer wavelengths. This, however, does not mean we should always try to utilize the radiation at this longer wavelength. For applications whose main interest is the photon flux within some fixed narrow bandwidth $\Delta\lambda/\lambda$, this is the way to go. But for applications where intensity

and brightness are important, the radiation at λ_0 is preferred, after we check Fig. 3-5 for their angular distributions.

In Fig. 3-5, we see that the radiation at λ_0 is concentrated in the forward direction. As a result, although the photon flux at λ_0 is lower than at longer wavelengths, the brightness is not lowered. In fact, it has the maximum possible on-axis brightness since longer wavelengths have a dip in the forward direction. This property is particularly important for experiments that use on-axis pinholes to do spatial filtering and improve the spatial coherence. In addition, the regularly shaped angular distribution can be approximated to a Gaussian profile and simplifies further analysis, as discussed in next section. For these reasons, we will concentrate our attention on the radiation at λ_0 to carry future calculations on spectral brightness and coherent power.

From Fig. 3-5, the radiation at λ_0 is mostly contained in the region $\theta < \theta_{cen}$, which explains why a pinhole with collection angle θ_{cen} will be able to catch most of the available photon flux at λ_0, as has been observed in Fig. 3-4. Longer wavelengths are spread beyond the central radiation cone (θ_{cen}), therefore larger pinholes are needed to catch those photons. This is important for preparing aforementioned experiments where higher photon flux in a fixed narrow bandwidth is the main interest. In these cases, an upstream collection angle greater than θ_{cen} (preferably about 1.4 θ_{cen}; see red line in Fig. 3-5) should be used and the monochromator should be tuned to longer wavelength, approximately at $\lambda_0(1+1/N)$. The in-band photon flux at this longer wavelength would be maximized and is twice of that at λ_0, approaching that predicted by Eq. (3-11b). For other applications in which high spectral brightness is important, a collection angle of θ_{cen} is the optimal choice. It can accept most of the useful photons at λ_0 while blocking the longer wavelengths, reducing the heat load and spectral contamination for downstream experiments.

3.2.3 Photon Beam (by a Single Electron)

Although in this section we are only dealing with the radiation from a single electron, we can not automatically assume the source size to be zero or arbitrarily small. Since the radiation is concentrated within a very narrow forwarding cone, there's a photon beam source size associated with it, set by the minimum phase-space product for any light beam as stated in chapter 2. Here we use a Gaussian beam approximation to the radiation at λ_0. The angular distribution of the photon beam at λ_0 (the black line in Fig. 3-5) can be approximated by a Gaussian with rms angular spread [33]

$$\sigma'_{ph} = \theta_{cen}/2 = \frac{1}{2\gamma^*\sqrt{N}} = \sqrt{\frac{\lambda_0}{2L}} \qquad \text{Eq. (3-13)}$$

where $L = N\,\lambda_u$ is the undulator length. We note that for diffraction-limited radiation, the concomitant beam size (rms) is

$$\sigma_{ph} = \frac{\lambda/4\pi}{\sigma'_{ph}} = \frac{\sqrt{2\lambda_0 L}}{4\pi} \qquad \text{Eq. (3-14)}$$

In next section the photon beam parameters will be combined with electron beam parameters to obtain an accurate description of the photon beam emerging from an undulator.

3.3 Properties of Undulator Radiation from a Finite Electron Beam

The above discussions are based on a single electron moving on-axis, or, equivalently, the limiting case in which all the electron trajectories are identical. In real synchrotron radiation facilities, electron beams are used to increase the number of radiators and boost photon output. As a result of the physics and dynamics of beam creation, an electron beam has finite

beam size and divergence angle, usually described by Gaussian distributions in both spatial and angular coordinates:

$$n(x,y) = \frac{N_0}{2\pi\sigma_x\sigma_y}\exp(-\frac{x^2}{2\sigma_x^2})\exp(-\frac{y^2}{2\sigma_y^2})$$

and

$$n(\theta_x,\theta_y) = \frac{N_0}{2\pi\sigma'_x\sigma'_y}\exp(-\frac{\theta_x^2}{2\sigma'^2_x})\exp(-\frac{\theta_y^2}{2\sigma'^2_y})$$

Usually a set of parameters is used to describe the electron beam's distribution in an undulator: emittance ε and β-value. They are related to the beam size and divergence as $\varepsilon_{x,y} = \pi\sigma_{x,y}\sigma'_{x,y}$ and $\beta_{x,y} = \sigma_{x,y}/\sigma'_{x,y}$. Emittance of the electron beam is a phase-space product, similar to that of light beam discussed in chapter 2. Modern 3rd generation synchrotron facilities differ themselves from older generation ones largely on the small emittance beams they used, typically in the order of nm·rad. This ensures the electron beam itself does not compromise the high brightness of the radiation, as we will see below.

3.3.1 The Influence of Beam Size

Usually the beam size is quite small (on order of 100s μm or less) so there is no noticeable difference in the magnetic field at this scale. Therefore the electron's trajectory is not affected by the finite beam size. Also the downstream workstation at an undulator beamline is usually located fairly far from the source (10's m). Therefore, the finite electron beam size has negligible influence on the radiation power, spectrum, or angular distribution. However, it has a dominating effect on both the brightness and the spatial coherence of undulator radiation. It defines the size of an incoherent source (once again, we are not considering an

FEL here, and treat electrons as uncorrelated.) Consequently, spatially coherent radiation can only be obtained in a limited solid angle, which can be related to the incoherent source size by the van Cittert-Zernike theorem (see chapter 2). This is represented by the decrease of brightness through the increase of source size. The "total" photon beam size is the convolution of the electron beam size and the photon beam size by a single electron (as discussed in section 3.2.3). It is straightforward to calculate when both are Gaussian:

$$\sigma_{Tx,y} = \sqrt{\sigma_{x,y}{}^2 + \sigma_{ph}{}^2} = \sqrt{\sigma_{x,y}{}^2 + \lambda_0 L / 8\pi^2} \qquad \text{Eq. (3-15)}$$

Generally σ_{ph} is small compared with the electron beam size, but there are also situations that they are comparable, especially at vertical direction (emittance at vertical direction is usually much smaller than horizontal direction) and for undulators operating at long wavelengths (σ_{ph} is proportional to $\sqrt{\lambda}$). Therefore, an undulator operating at SXR/hard x-ray wavelengths can usually be well approximated as an incoherent source whose size is determined by the electron beam, while one operating in the EUV region should be treated as a partially coherent source with its size including a diffraction-limited term, as expressed by Eq. (3-15).

3.3.2 The Influence of Beam Divergence

Unlike the beam size, the beam divergence, due to the off-axis motion of many electrons, causes a more noticeable change to the observed undulator radiation. On one hand, it is directly related to the angular distribution of the radiation. On the other hand, since the undulator spectrum is determined by the angular-dependent Doppler shift, deviations of the electron's motion from the axial direction will also change the spectrum.

It is worthwhile to show at the beginning that radiation from every electron is essentially identical, if observed along its own 'axis'. To show this, let us compare two electrons, one moving in the axial direction (of the undulator), while the other one moving in some small off-axis angle α. They will experience different undulator magnetic fields. The difference, to the first order, is just a slight difference in magnetic field's period. Along the direction of off-axis angle α, the period of magnetic field is a little bit longer at $\lambda_u(\alpha) = \lambda_u/\cos\alpha$. For small α, the relative change $[\lambda_u(\alpha)-\lambda_u]/\lambda_u$ can be found to be $\alpha^2/2+o(\alpha^3)$. This is a negligible change since the divergence angle spread for a typical electron beam used in modern synchrotron radiation facility is on the order of μrads. This means that electrons moving off-axis give basically the same radiation, but directing it to different angles. (See Fig. 3-6)

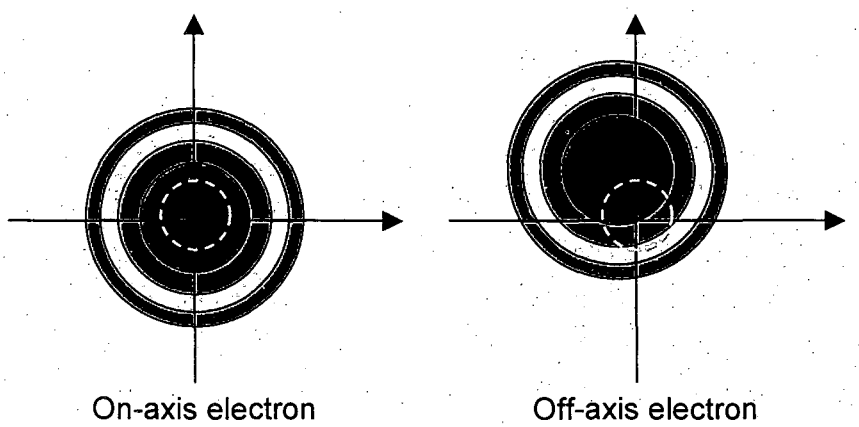

Figure 3-6. Influence of electron beam divergence. Off-axis moving electrons will produce essentially same radiation, but aiming at different direction. A small aperture (white dash line) will see longer wavelengths from those off-axis electrons due to the angular-dependent Doppler shift.

Ideally when σ'_x and σ'_y are small compared with θ_{cen}, their influence will be "screened" and the effect will be minimal. However, in a typical undulator, although σ'_y (vertical direction) can probably satisfy this, σ'_x is usually not much smaller than θ_{cen}, especially at high photon energies where θ_{cen} is very small itself (recall that $\theta_{cen} = 1/\gamma^* \sqrt{N} = \sqrt{2\lambda_0 / L}$). Large divergence angles can have a significant effect on the properties of undulator radiation, as will be examined below.

1) Spectrum Within A Particular Collection Angle

Following the above discussion, we will get the same spectrum as in previous section when the collection angle is large enough to cover all electron directions, i.e., integrated in angle. However, this is not true for a limited collection angle. For example, if we collect the light within a very small pinhole on axis, due to the angular-dependent Doppler shift, we will see different wavelengths from electrons moving in different directions. The contributions from the off-axis electrons will always be at longer wavelengths (see Fig. 3-6). This is another spectrum broadening effect, independent of the finite N-cycle effect discussed in the last section. The final spectrum will show the combined effect of the two.

Unlike the homogenous broadening associated with finite oscillation cycles, the divergence broadening depends on the <u>relative</u> angular distribution of the electron beam around each observation angle, which varies and is generally not symmetric. Therefore, no simple convolution can be done. There are only preliminary results published on this broadening effect [34], limited to the on-axis spectrum only, where the calculation is greatly simplified.

To investigate more generally this inhomogeneous broadening effect, we developed a computer program performing numerical integration of the spectrum within any pre-

designated collection angle. It is capable of calculating the spectrum under the effect of both N-cycle homogeneous broadening and Doppler-shift induced inhomogeneous broadening. It can also deal with arbitrary electron divergence distribution. For our continuing discussions, the program is used to calculate the spectral broadening within the central radiation cone, assuming different electron beam divergence distributions. To mimic the typical electron beam parameter, we use a Gaussian distribution in the x-direction and assumes $\sigma_y' = 0$. The result is presented in Fig. 3-7.

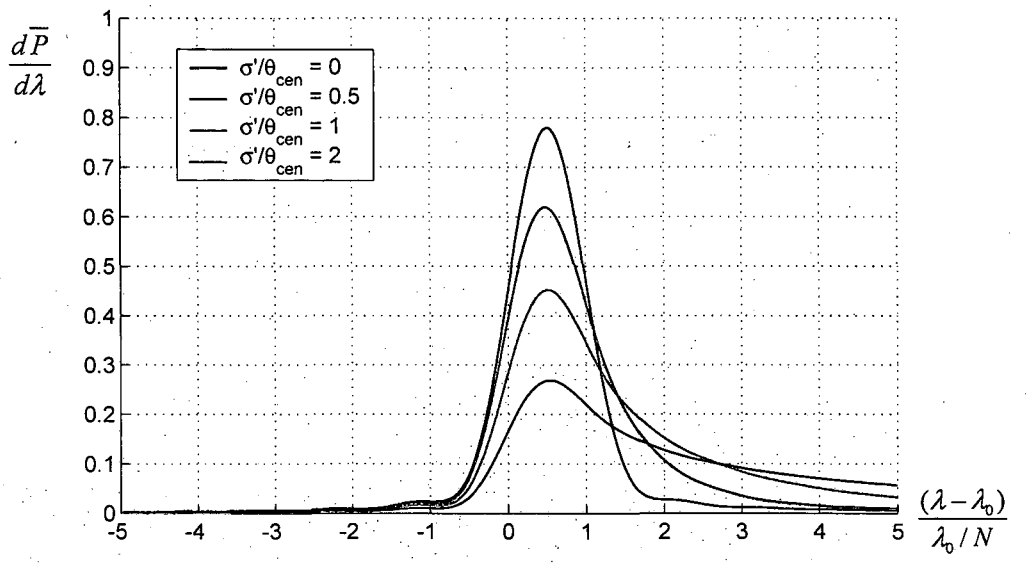

Figure 3-7. Spectral broadening in the central radiation cone as a result of electron beam divergence.

In Fig. 3-7, the $\sigma' = 0$ curve is the same as the black curve in Fig. 3-4. The others include the divergence effect. They show a gradually increased bandwidth, expanding to the long wavelength side. From it, we see that with large divergence angle, $\sigma' > \theta_{cen}$, a monochromator-less setup for getting narrow band radiation (~1/N) from just a pinhole will not work well. This spectral broadening effect will cause a decrease of spectral

brightness. It should be noticed that the decrease of spectral brightness here is not due to larger phase-space product, but due to the broader bandwidth. In other words, we get the same power from a given pinhole (whatever the divergence is), but the relative bandwidth will increase with increasing electron beam divergence. Therefore, the spectral density within a desired wavelength region (for example, around λ_0 in the figure) will be lower. While the brightness is not affected, the spectral brightness may be significantly reduced. As stated earlier, this effect is not easy evaluated in closed form. It depends on the selection of collection angle and requires use of numerical methods.

2) Angular Distribution Broadening at A Particular Wavelength

There's an alternative approach for investigating the decreased spectral brightness with large electron beam divergence. As explained in Fig. 3-6 and its related text, we can still obtain the same "spectral" photon flux, although they will be distributed in expanded angles. The expansion in angular distribution turns out to be easier to treat mathematically, since we only need to make a convolution of the angular distribution of the radiation from a single electron moving on-axis and the electron beam's Gaussian divergence angle distribution. Such a convolution can be done rather simply if the first is also Gaussian. We therefore use the radiation at λ_0 to do the calculation since it has an approximately Gaussian angular distribution (See section 3.2.3). The total angle is obtained by adding the two Gaussian distribution:

$$\sigma'_{Tx,y} = \sqrt{\sigma'^{\,2}_{x,y} + \sigma'^{\,2}_{ph}} = \sqrt{\sigma'^{\,2}_{x,y} + \lambda_0 / 2L} \qquad \text{Eq. (3-16)}$$

which represents the "total" rms photon beam divergence.

3.3.3 Spectral Brightness and Coherent Power Calculations

Following the previous discussions, including the effects of spectrum broadening and angular expansion, the spectral brightness of undulator radiation can be calculated at the central wavelength λ_0 as:

$$\overline{B}_{\Delta\lambda/\lambda}\Big|_{\lambda_0} = \frac{\overline{F}_{\Delta\lambda/\lambda}\Big|_{\lambda_0}}{(2\pi\sigma_{Tx}\sigma'_{Tx})(2\pi\sigma_{Ty}\sigma'_{Ty})} \qquad \text{Eq. (3-17)}$$

where $\overline{F}_{\Delta\lambda/\lambda}\Big|_{\lambda_0}$ can be obtained from Eq. (3-12), $\sigma_{Tx,y}$ and $\sigma'_{Tx,y}$ can be obtained from Eq. (3-15) and Eq. (3-16), respectively. From Eq. (2-11b), the coherent power is

$$\overline{P}_{coh,\Delta\lambda/\lambda} = \overline{B}_{\Delta\lambda/\lambda} \cdot (\frac{\lambda}{2})^2 \cdot \frac{hc}{\lambda} \cdot \eta \qquad \text{Eq. (3-18)}$$

It represents a spatially coherent power within $\Delta\lambda/\lambda$ bandwidth. Term hc/λ is for converting photon flux in unit of photons per second to power in unit of watt. An efficiency factor of η is included for possible losses (absorption, scattering, etc.) in the beamline optics (mirrors, monochromator, etc.).

It should be pointed out here that the brightness and coherent power calculation here is a conservative one. It is based on a Gaussian beam approximation of radiation from a single electron, which only occurs at the central wavelength λ_0. As we saw earlier, the photon flux at λ_0 is only half of that at longer wavelengths. This lower photon flux is compensated by the relatively narrower angular distribution so that the brightness is not lowered. However, under the circumstances where the electron beam's emittance is much larger than the phase-space product of the photon beam from a single electron, we will not see the difference of angular distributions at different wavelengths; they will all be dominated by the electron beam emittance. In these cases, the brightness can be a factor of 2 higher at wavelengths

longer than λ_0. In addition, the use of Eq. (3-18) (and Eq. (2-11b)) assumes the coherent power is contained within the minimum $(\lambda/2)^2$ phase-space product, which is only valid for the fundamental Gaussian mode. From Fig. 3-5, the angular distributions generally are not Gaussian. This implies that the spatial mode may occupy a larger phase-space product than $(\lambda/2)^2$, which in turn means that more spatially coherent power can be available.

3.4 Undulator Harmonics

The previous treatments are based on the model of a quasi-monochromatic dipole radiating in the moving frame of reference. This is a good approximation for $K \ll 1$. Since the power radiated scales with K^2, it's quite common to operate the undulator with larger values of K, where corrections to the monochromatic dipole model are needed. To see the effect of larger K value, recall Eq. (3-3):

$$\frac{v_z}{c} = 1 - \frac{1+K^2/2}{2\gamma^2} + \frac{K^2}{4\gamma^2}\cos(2k_u z)$$

In section 3.2, we ignored the last oscillation term and approximated the electron's z-motion to have a constant velocity $v_z \approx \overline{v_z}$. If the oscillation term is kept, in the moving frame of reference the z-motion will show a second harmonic term. Consequently, the x-motion will show frequencies of odd harmonics as a result of the nonlinear $\vec{V} \times \vec{B}$ term in the force equation, as well as contributions arising from the space-time transformation [35]. Furthermore, since both the x- and z-motion (in the moving frame of reference) are relativistic at large K values, there will be further frequency mixing as a result of phase modulations associated with the retarded time. This requires more care in calculations in the moving frame of reference. At large K values, it is actually simpler to calculate the radiation

spectrum and pattern in the rest frame of reference, in which the electron's trajectory, to a high degree of accuracy, can be expressed as: (refer to deductions in pg. 32)

$$x = \frac{K}{\gamma\beta^* k_u}\sin(\omega_u t);\ z = \beta^* ct + \frac{K^2}{8\gamma^2 k_u}\sin(2\omega_u t)$$

The radiation field can be calculated with standard method in classical electrodynamics for relativistic particles [14]. Higher harmonics will appear, with their strengths expressed by Bessel function terms [36]. The near-axis spectrum will show strong peaks around odd harmonics (n=1, 3, 5, ...) of the fundamental frequency. For most cases, the radiation within a small solid angle around the forward direction is of most interest. Under such situations, our previous discussion based on a constant power density and Doppler-shift-determined spectrum is still valid. When dealing with harmonics, we can keep most of our results in previous sections by making modifications as following [33, 36]:

1. Eq. (3-9): Power per unit solid angle $d\overline{P}/d\Omega$ is multiplied by a factor

$$f(n,K) = n^2\left(J_{\frac{n-1}{2}}\left[\frac{nK^2}{4(1+K^2/2)}\right] - J_{\frac{n+1}{2}}\left[\frac{nK^2}{4(1+K^2/2)}\right]\right)^2$$

where J denotes the Bessel function of the first kind. The Bessel function term accounts for the power transfer to higher harmonics with increased K value. The following table shows some values of $f(n,K)$ for different n and K values:

	n = 1	n = 3	n = 5	n = 7
K = 0.1	0.9975	1.248E-3	9.309E-9	5.903E-14
K = 0.5	0.9437	0.05700	2.088E-3	6.533E-5
K = 1.0	0.8281	0.4032	0.1237	0.03276
K = 2.0	0.6529	0.9515	0.9282	0.7973
K = 5.0	0.5210	1.012	1.368	1.658

For K≪1, the correction to the fundamental is minimal and higher harmonics can

be ignored. On the other hand, higher harmonics grow rapidly with increasing K. When K ≫ 1, the higher harmonics can be much stronger than the fundamental.

2. Wavelengths change to $1/n$ of that from Eq. (3-5):

$$\lambda_{0,n} = \frac{\lambda_u}{2n\gamma^{*2}} = \frac{\lambda_u}{2n\gamma^2}(1+\frac{K^2}{2})$$

3. The "natural" bandwidth and Doppler width at the central radiation cone angle is $\Delta\lambda/\lambda \sim 1/nN$;

4. Eq. (3-8): The central radiation cone angle reduces to

$$\theta_{cen,n} = \theta_{cen,1}/\sqrt{n} = 1/\gamma^*\sqrt{nN};$$

5. From 1) and 4), power within central radiation cone for harmonics is

$$\overline{P}_{cen,n} = N_e \cdot \frac{d\overline{P}_n}{d\Omega} \cdot \pi\theta^2_{cen,n} = \frac{\pi e\gamma^2 I}{\varepsilon_0\lambda_u}\frac{K^2}{(1+K^2/2)^2}\frac{f(n,K)}{n}$$

Other formulas can also be used after making these modifications.

3.5 An Example

In this section some results from an undulator at the Advance Light Source (ALS) [37] are presented as an example. The undulator used is U8 (λ_u = 8 cm) with N = 55 periods. The electron beam parameters used are δ_x= 310 μm, δ_y= 23 μm, δ_x'= 23 μrad and δ_y'= 6.5 μrad. The calculation results are presented in Fig. 3-8. The 3rd harmonic is included, showing U8's capacity at keV level photon energies. The unit for spectral brightness is the widely used photons/sec/mm^2/mrad^2. Coherent power refers to spatially coherent power within 0.1% bandwidth, calculated from spectral brightness using Eq. (3-18) and includes a beamline efficiency of 10%. The tuning assumes K values from 0.2 to 4. The results, e.g., power levels on the order of one watt in ~1% spectral bandwidth, and 10^{18}-10^{19} spectral brightness, are

typical values for undulator beamlines at a modern 2 GeV storage ring.

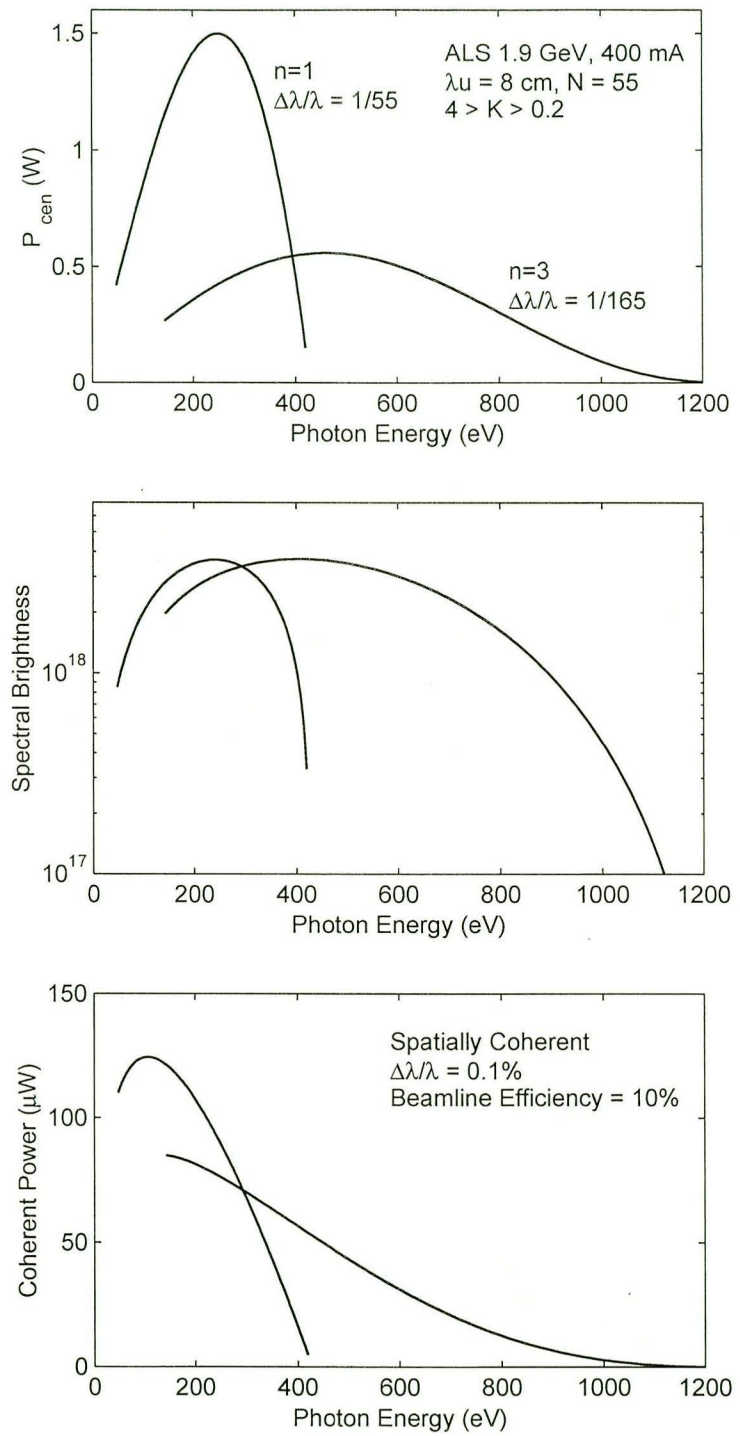

Figure 3-8. Calculation results of $\overline{P}_{cen}$, spectral brightness and coherent power of ALS U8.

Experimentally, the undulator (beamline 12 at ALS) has been demonstrated to generate spatially coherent power using a simple pinhole spatial filtering technique. Fig. 3-9 shows Airy patterns obtained at EUV wavelengths through pinhole diffraction. Deep dark rings at the Airy pattern's null positions imply high spatial coherence. The spatial coherence of the EUV radiation is also measured using two-pinhole interference method [38] (See Fig. 3-10). Similar one pinhole diffraction and two pinhole interference experiments are underway to investigate the coherence properties of 3rd harmonic radiation at 500 - 1000 eV [39].

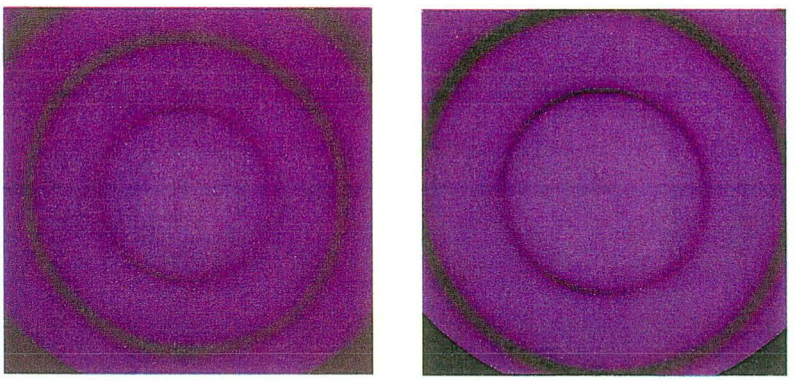

Figure 3-9. Airy patterns obtained by pinhole spatial filtering of ALS U8. (Courtesy of P. Naulleau, CXRO/LBNL)

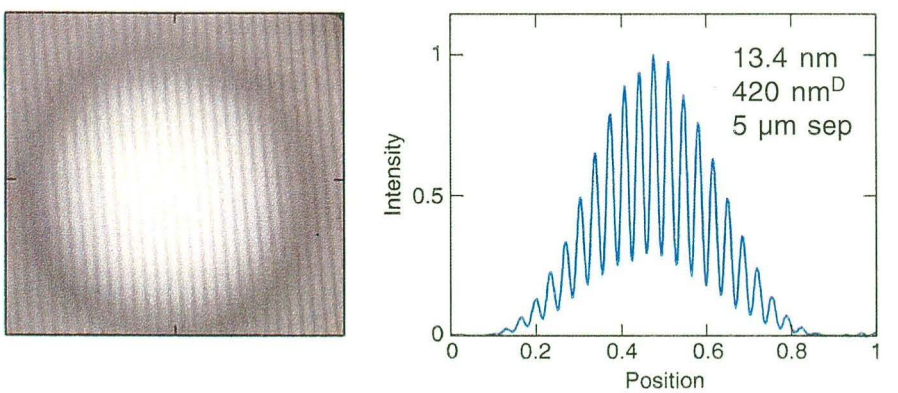

Figure 3-10. Two pinhole interference experiment demonstrating the spatial coherence properties of undulator radiation. (Courtesy of C. Chang, CXRO/LBNL) [38]

The highly coherent radiation obtained from undulator radiation has been used to achieve extraordinarily high wavefront accuracy using an EUV interferometer at the same beamline [4]. Fig. 3-11 shows an interferogram and the retrieved wavefront map of an EUV optical system at 13.4 nm wavelength. Other interferometers have been used to measure the refractive index of materials at EUV wavelengths [40].

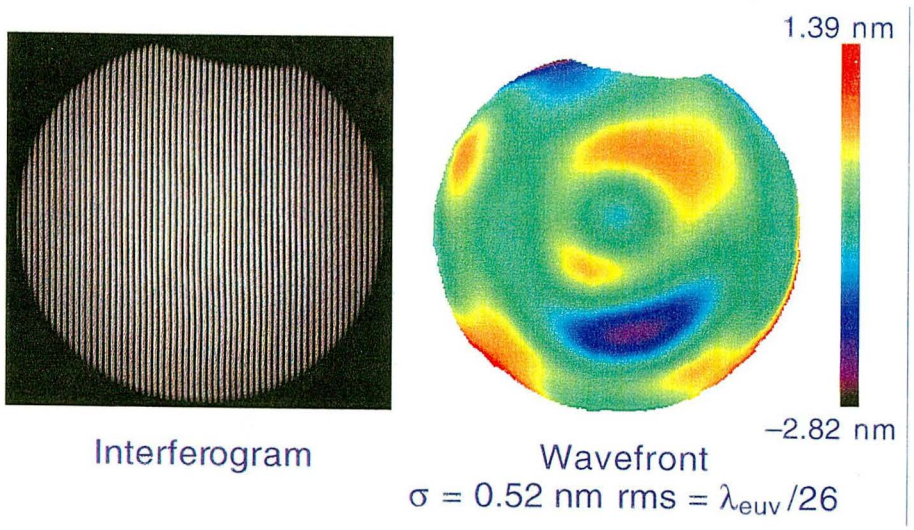

Figure 3-11. An interferogram of a multilayer-coated Schwarzchild optical system measured at a wavelength of 13.4 nm, and the retrieved wavefront map. (Courtesy of P. Naulleau, K. Goldberg, J. Bokor, et al., CXRO/LBNL)

3.6 Comments on Undulator Radiation as EUV/SXR Source

Undulator radiation provides watt-level power within the central radiation cone. By limiting the electron beam's phase-space product (emittance), 3rd generation synchrotron radiation facilities can take advantage of the high spectral brightness nature of the undulator radiation. Very useful coherent power can be obtained through the use of pinhole spatial filtering techniques. These properties are readily scalable to shorter x-ray wavelengths through the

use of higher energy electron beam. 1-2 GeV low-energy machines and 6-8 GeV high-energy machines are providing complementary coverage of the whole short wavelength spectrum, from UV to hard x-ray.

The main limitation of undulator radiation, just as any other synchrotron-based sources, is its size and cost, and thus its limited accessibility. Limited numbers of undulator beamlines, which are only available at few national facilities, are also usually heavily booked. This is the main motivation for developing smaller scale, even tabletop, sources. As we will see in the following chapters, these sources present some additional advantages, for example they can provide much higher peak power when compared with the quasi-continuous wave synchrotron radiation. The unique strengths of the compact sources open new opportunities and will accelerate science and technology advances in short wavelengths due to their wide availability; however, undulator radiation currently represents the standard technique to provide continuously tunable, coherent radiation throughout EUV/SXR/X-ray region. It is currently the only practical source for many demanding experiments.

Chapter 4

Extreme Ultraviolet / Soft X-Ray Laser

4.1 Lasers Working in the EUV/SXR Spectral Region

"Laser" is probably the first word crossing one's mind when thinking of a coherent light source. Proposals for an x-ray laser started shortly after the demonstration of the first laser [41]. However, while optical laser technologies have enjoyed dramatic progress since then, building a laser working at significantly shorter wavelengths has been found to be extremely challenging. The challenges come mainly from difficulties with achieving and maintaining population inversions that can support high gain lasing at these very short wavelengths.

4.1.1 Lasing Medium: Hot-Dense Plasma

Considering the high photon energies of EUV/SXR radiation, the energy levels involved in EUV/SXR lasers have to be on order of one hundred eV, or higher, above the ground state. To excite such levels generally causes ionizations and thus the creation of a plasma state. As a result, the commonly used lasing medium in EUV/SXR region is hot-dense plasma consisting of highly ionized atoms and energetic electrons. High temperature (hot) is generally necessary for exciting the ions to required energy levels. High density of excited ions (dense) is required for high gain. *

* Hot-dense plasma is not the only possible lasing medium in short wavelength region. Other mechanisms, such as photoionization [42] and resonant photopumping [43] can, in principle, also realize population inversion and lasing in short wavelengths. Here we limit our discussions to the widely used method of electron collision excitation, where the high kinetic energy of electron is necessary. See Ref. 15 for a review of different population inversion mechanisms.

The plasma for lasing is usually prepared at optimized conditions to take advantage of the so-called "ionization bottleneck" effect to maximize the fraction of ions in a desired ionization state. These ionization sates have closed electron shells, for example neon-like ($1s^2 2s^2 2p^6$) or nickel-like ($1s^2 2s^2 2p^6 3s^2 3p^6 3d^{10}$), and are much harder to ionize further. For example, in a Ne-like Ar laser described in next section, it takes 124 eV to ionize Mg-like Ar (12 electrons) to Na-like, 143 eV to ionize Na-like (11 electrons) to Ne-like, but it will take 422 eV to ionize the Ne-like (10 electrons, closed shell) configuration [44]. Using this "ionization bottleneck" effect, optimal plasma temperature will put a large portion of the ions into a single ionization state, increasing the number of ions involved in a particular lasing transition. Given the difficulties of exciting ions to higher levels, population inversion is often accomplished by a rapid depletion of the lower level through a strong radiative decay. Fig. 4-1 shows an example of a laser transition between the 3p and 3s states of a neon-like configuration.

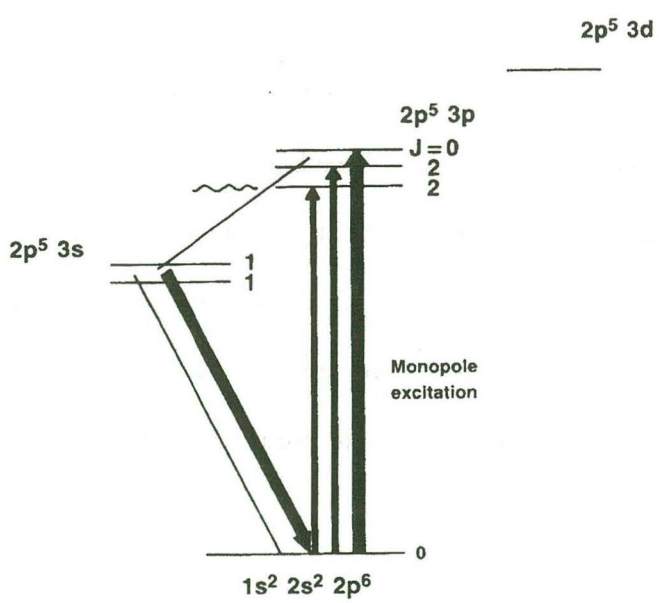

Figure 4-1. Energy level diagram for a Ne-like 3p-3s laser excited from the $2p^6$ ground state by electron collisions. Monopole excitation refers to electron impact excitation. [45]

Note that the temperature and density requirements for a plasma laser are much higher than those of an incoherent plasma source radiating in the same wavelength region. Without the requirement of population inversion, an incoherent plasmas source only needs an electron temperature capable of exciting the ion to a desired energy level, high enough above the ground state to produce the desired photon energy. Taking Fig. 4-1 as an example, the lasing photon energy is $E_{laser} = E_{3p}-E_{3s}$. On the other hand, the plasma would have strong emissions by transitions from all the excited states to ground state whenever the transition is not forbidden. The photon energies from these transitions can be much higher than E_{laser}. Without the requirement of high gain, the density of the plasma can also be much lower. This is why a 46.9-nm laser (26 eV photon energy) requires electron temperature of ~60-80 eV*, and density around 5×10^{18} cm^{-3} [46], while an incoherent plasma source for EUV lithography at 13.4 nm (92 eV photon energy) needs only an electron temperature of ~30 eV and density below 10^{18} cm^{-3}, as blackbody emission peaks at 2.82 kTe. [47]

4.1.2 Amplified Spontaneous Emission (ASE)

EUV/SXR lasers resemble optical lasers in many ways. Both require lasing media in which population inversion is achieved by external pumping. Both work on the principle of light amplification by stimulated emission, with characteristic exponential increase of intensity for small signals and eventually saturation for strong signals. However, there is a very big difference: EUV/SXR lasers generally do not benefit form the use of an oscillation cavity.

---

* Electron temperature in hot-dense plasma is represented in unit of eV through Boltzmann constant: $kT_e = 100$ eV corresponds to $T_e = 1.6 \times 10^6$ K.

Historically, the lack of efficient reflective optics at EUV/SXR region (see chapter 1) made it difficult to find suitable mirrors to form the cavity. Right now, although multilayer coatings can serve as good normal-incidence mirrors, they are limited to some particular wavelength regions and vulnerable to damage caused by debris and radiation from the plasma. Another fundamentally limiting factor is the short lifetime of lasing in plasma. To excite atoms (ions) to desired energy levels and reach a certain degree of population inversion, significant power has to be delivered in a very short time. This is usually achieved by using a high power laser or fast electric discharge as pump source, whose pulse width is nanosecond in duration or shorter, to drive the high output power. Maintaining the plasma conditions is also difficult, since the plasma tends to expand and cool quickly. As a result, the population inversion and gain in the lasing medium (hot-dense plasma) can last only for a very short period of time. Therefore, even using a cavity, there will not be many oscillations before the lasing process dies. For these reasons, EUV/SXR lasers are generally limited to single pass or double pass amplification of spontaneous emission (ASE) through a high gain plasma.

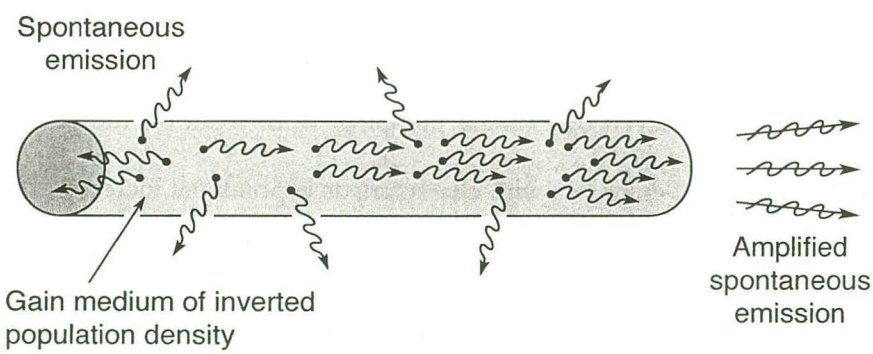

Fig. 4-2. Illustration of Amplified Spontaneous Emission (ASE) process. [48]

Fig. 4-2 illustrates the single pass ASE process in a plasma column. Although it only shows the amplification toward the right, please be advised that ASE actually occurs in all directions. Radiation to the side leaves the gain medium in too short a path to experience significant gain. Double-pass setups utilizing a mirror close to one end of the plasma column effectively increases its length, but have seen limited use due to pulse duration and damage.

The ASE process differs from the totally random spontaneous emission (as in a thermal source) in that the stimulated emission process indeed dominates in a high gain medium, especially at the ends of a long plasma column, where the emission from one end has experienced sufficient amplification (notice the right end of the plasma column in Fig. 4-2). However, the spontaneous emission origin means the output is, in nature, amplified noise. This makes the coherence properties of EUV/SXR laser beam very different from what we usually associate with an optical laser.

4.1.3 Limited Coherence of EUV/SXR Lasers and Possible Solutions

The operation of an EUV/SXR laser with only ASE (no cavity) greatly limits the coherence of the laser beam. Both the temporal and spatial coherence properties of an EUV/SXR laser beam can be significantly worse than those of the familiar (optical) laser beam.

The temporal coherence length is determined by the spectral bandwidth as $L_c = \lambda^2 / \Delta\lambda$ (Eq. 2-4). Without a cavity to provide longitudinal mode selection and support the use of other bandwidth-narrowing elements (e.g., an etalon), the linewidth of EUV/SXR laser is limited by the natural bandwidth of the transition (determined by the energy level's lifetime), and is usually increased by Doppler broadening due to the high ion temperature. After considering the broadening effect, the temporal coherence length of an EUV/SXR laser generally falls

into the range of microns or less. This is much less than optical lasers with longer wavelengths, careful longitudinal mode control and further frequency stabilization, whose longitudinal coherence length can be a meter or more. Nevertheless, the line emission nature of the EUV/SXR laser still makes it a better choice in terms of the longitudinal coherence when compared with other sources in this wavelength region. Typical bandwidth of $\Delta\lambda/\lambda \sim 10^{-4}$ and microns of longitudinal coherence length are quite useful for EUV/SXR interferometry, holography, and scattering.

Poor spatial coherence is another consequence of the no-cavity EUV/SXR laser. Without control of the spatial mode structure, the ASE-based laser acts as an amplifier through which all spatial modes can get amplified. A direct approach for improving the spatial coherence involves using the plasma's geometry to discriminate against different spatial modes. A long and narrow column is clearly of favor here (See fig. 4-3). However, a high degree of spatial coherence throughout the output beam requires the gain medium to have a Fresnel number ($N_F = a^2/\lambda z$) less than unity. Considering the short wavelength, this is very difficult to achieve in a plasma column, unless some form of spatial filtering is used [49, 50]. In fact, past experiments on EUV/SXR lasers showed very limited spatial coherence [51]. The very large numbers of spatial modes contained in the output of EUV/SXR lasers keep them away from the commonly accepted standard of coherent light source set by optical lasers; for this reason they are sometimes called "amplifiers" rather than "lasers". The demonstration of nearly full spatial coherence has been one of the main goals of EUV/SXR laser research.

A solution to achieve single mode operation of an EUV/SXR laser was theoretically investigated and it was found that refraction in a plasma can effectively reduce the number of guided spatial modes inside the plasma, thus increase the spatial coherence of the output

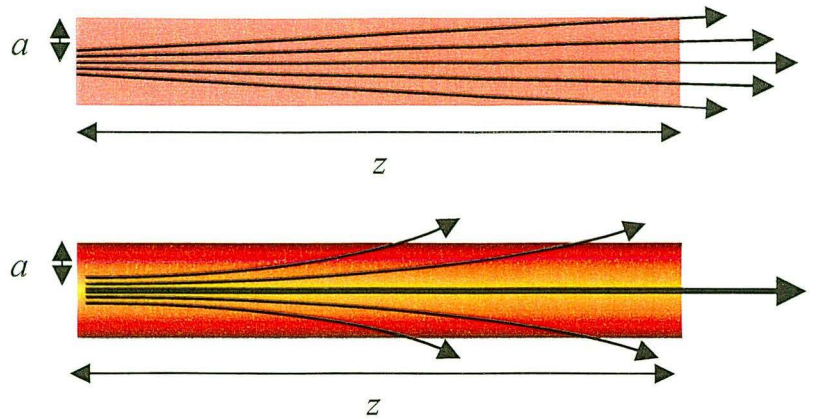

Figure 4-3. Mode selection in a plasma column. The upper diagram shows the case of low refraction, where the total number of guided modes is determined by the plasma's geometry. The lower diagram shows the case of strong refraction, where the total number of modes can be greatly reduced by refractive anti-guiding.

beam [52, 53]. The refractive index n in a plasma is less than unity due to the free electrons. It is related to the electron density n_e as

$$n = \sqrt{1 - \frac{n_e}{n_c}}$$

where

$$n_c = \frac{\pi m_e c^2}{e^2 \lambda^2}$$

is the critical density, above which light with wavelength λ can not penetrate into the plasma. In a plasma column, the axis region usually has the maximum electron density, thus least refractive index. Away from the axis region, the electron density is lower, and the refractive index is higher. As a result, refraction will "bend" light away from the axial region. Since gain is usually proportional to density, this causes the "refraction loss" and lowers the effective

gain, which is a well-known phenomenon to x-ray laser community. On the other hand, this refractive "anti-guiding" can significantly increase the spatial coherence of the laser beam as it leaves fewer modes to benefit from the available gain. Based on a simplified model assuming parabolic profiles for electron density and gain, calculations [52,53] show that the transverse coherence length (see section 2.1.2) at one end is

$$R_c(z) \approx \frac{z_r \sinh(z / z_r)}{ka} \tag{4-1}$$

where

$$z_r = a / \theta_r$$

and

$$\theta_r = \sqrt{n_{e0} / n_c}$$

z_r is "refraction length", the typical distance passed by a ray before it is refracted out of the active region. θ_r is the corresponding refraction angle.

Under weak refraction cases, z_r is long compared with plasma length such that $z \ll z_r$. At the limit of $z/z_r \rightarrow 0$, $\sinh(z/z_r) \rightarrow z/z_r$. Eq. (4-1) becomes a simpler form of $R_c(z) \approx z / ka$, which is what we expect from the van Cittert-Zernike theorem (see end of section 2.1.2). To approach full spatial coherence, we need $R_c(z) \sim a$, which will give us the same criteria as Fresnel number $N_F < 1$.

More interesting result comes when refraction is strong such that $z > z_r$. At the limit of $z \gg z_r$, $\sinh(z/z_r)$ approaches $\exp(z/z_r)/2$. This means an exponential increase of transverse coherence length with increasing plasma length, which is much faster than the linear increase in the weak refraction case. Although this looks promising, it still put very high requirement on the plasma column's geometry. The condition of $z > z_r$ is equivalent to $z/a > 1/\theta_r$. The

typical refraction angle θ_r in a lasing plasma is on the order of several mrad, which means that the length to width ratio of the plasma column has to be 100 or more to see a significant effect. This is not easy for typical plasma excitation techniques.

Recently the capillary discharge excitation of a 46.9 nm EUV laser developed by J. J. Rocca et al. in Colorado State University has been able to generate very long (>30 cm) and narrow (~200-300 μm) plasma columns [54]. With such elongated geometry, it provides a unique opportunity to verify rapid spatial coherence buildup due to refractive anti-guiding and test the possibility of approaching full spatial coherence with ASE-based EUV/SXR laser. In collaborations with Prof. Rocca's group, we performed a series of Thompson-Wolf two-pinhole interference experiments [24] with the laser. We demonstrated that refraction in a plasma with sharp density gradients can reduce the effective transverse source size significantly and result in essentially full spatial coherence [55]. It is to our knowledge the first demonstration of such high degree of spatial coherence from an EUV/SXR laser. The details of the experiments are presented in next section.

4.2 Coherence Properties of a 46.9-nm EUV Laser

4.2.1 Introduction to the Laser

The laser in our experiments is generated by excitation of an Ar-filled capillary channel with a fast discharge current pulse that rapidly compresses the plasma to form a dense and hot column with a large density of Ne-like ions [46, 56]. Collisional electron impact excitation of the Ne-like ions produces a population inversion between the 3p ($^1S_0$) and 3s ($^1P^1_0$) levels, resulting in amplification at 46.9 nm. The experiments are conducted utilizing aluminum oxide capillary channels 3.2 mm in diameter and up to 36 cm in length, filled with pre-

ionized Ar gas at a pressure of ~59 Pa. The plasma column is excited by a current pulse of ~25 kA peak amplitude, with a 10% to 90% rise time of approximately 40 ns. The set up is similar to that used in previous experiments [54, 57]. The excitation current pulse was produced by discharging a water-filled dielectric capacitor through a spark gap switch connected in series with the capillary load. The laser is very compact, occupying a table area of only 0.4x1 m.

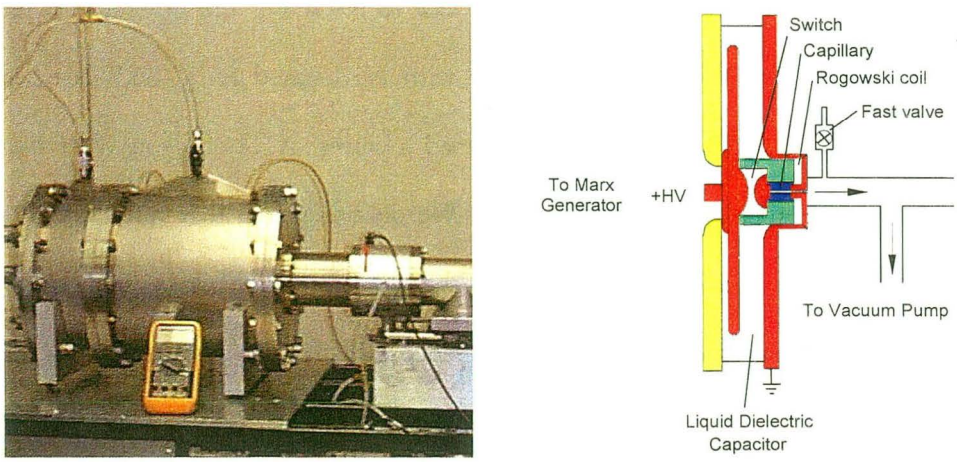

Figure 4-4. Photograph and schematic diagram of the 46.9-nm EUV laser. The laser is very compact (notice the multimeter in front). (Courtesy of J. J. Rocca, Colorado State University)

Efficient extraction of energy is obtained by operating the laser in a highly saturated regime. The laser pulse energy increases as a near exponential function of plasma column length, until the beam intensity reaches the gain saturation intensity at a plasma column length of about 14 cm [56]. For longer plasma columns, the laser pulse energy increases linearly with length from 0.075 mJ for a plasma column 16 cm in length, to 0.88 mJ (> 2×10^{14} photons/pulse) for a plasma column length of 34.5 cm. An average laser power of 3.5 mW is obtained when operating the laser at a repetition rate of 4 Hz [57].

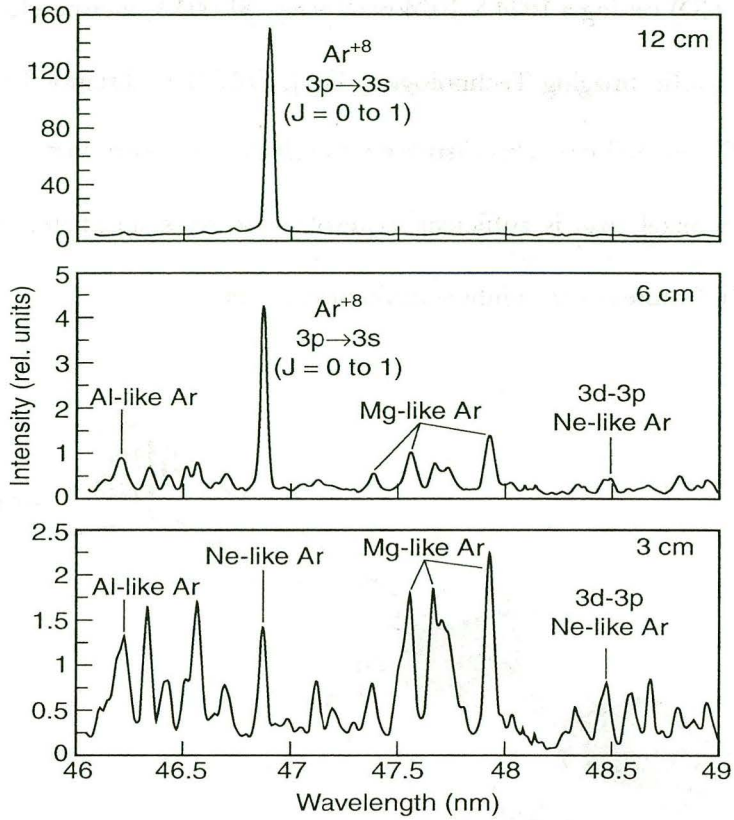

Figure 4-5. Axial spectra of Ar capillary discharge for three plasma lengths, showing the gradual domination of the 46.9-nm lasing line of Ne-like Ar. From Rocca et al., Ref. 56.

4.2.2 Spatial Coherence Measurements

The set up used in our two-pinhole interference experiment is shown in Figure 4-6. The pinhole masks consisted of pairs of 10 μm diameter laser-drilled pinholes at selected separations in 12.5 μm thick stainless steel substrates (National Aperture Inc., NH). Measurements were conducted placing the masks at axial distances of 15 cm and 40 cm from the exit of the capillary. An x-y translation stage was used to position the pinholes with respect to the beam. The interference patterns were recorded with an EUV sensitive charge-

coupled device (CCD) having a 1024 × 1024 pixel array (SI-003A, thermo-electrically cooled, back-thinned, Scientific Imaging Technologies, Tigal, OR). The distance from the pinhole plane to the CCD was 300 cm. This distance was selected to assure that the CCD's spatial resolution (25 μm pixel size) is sufficient to resolve the finest interference fringes, while recording essential features of the pinhole diffraction patterns.

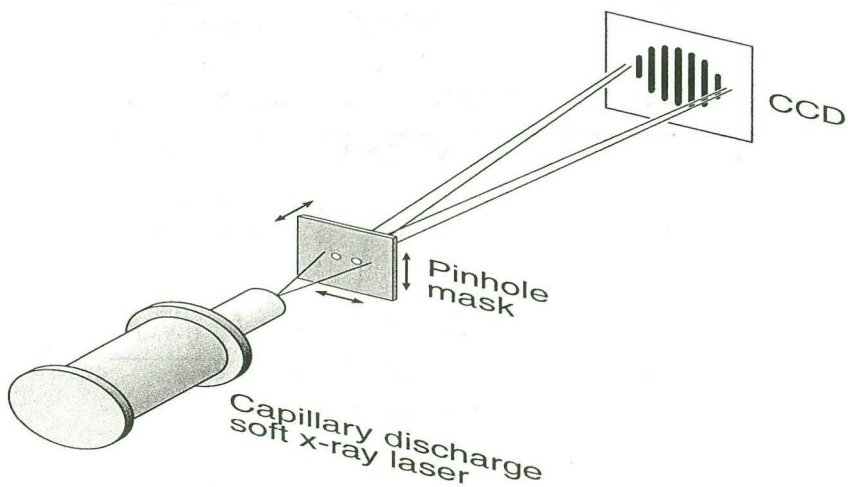

Figure 4-6. Schematic representation of the experimental set-up used in the two-pinhole interference coherence measurements.

The interference patterns recorded by the CCD contain an underlying background that is due to spontaneously emitted radiation from the hot plasma. To reduce its effect, we recorded the background after acquiring each interferogram. This was done by increasing the gas discharge pressure to ~130 Pa, which quenches the laser line while maintaining the background emission. Final interferograms were obtained by subtracting the recorded backgrounds from the original interferograms. This procedure also removes thermal "dark counts" of the CCD. The background is, however, somewhat weaker in the higher pressure

shots, thus the background removal is not complete. Therefore the fringe visibility is always somewhat undervalued. As a result, the highest spatial coherence values reported herein, which are sensitive to a small amount of background, constitute a conservative evaluation of the spatial coherence of the source.

Comparative interferograms corresponding to increasing capillary lengths of 18, 27 and 36 cm are shown in Fig. 4-7, with their corresponding lineouts. A mask with pinhole separation of 200 μm was used in all three measurements. The mask was positioned at a distance of 40 cm from capillary exit. The interferograms consist of two overlapped Airy patterns, modulated by the interference between them. The expected coherence buildup with increasing capillary length is clearly observed. The fringe visibility increases from 0.05 for the 18 cm long capillary, to 0.33 for the 27 cm long plasma, and reaches 0.8 for the 36 cm capillary. Assuming a Gaussian profile of the degree of coherence $|\mu_{12}|$, the coherence radii [58] for the three capillary lengths are 80, 135 and 300 μm, respectively. Although the last number is likely to be significantly underestimated as result of the background error, it is quite clear that the coherence radius scales much faster than linearly with capillary length. This is evidence of refractive mode selection as gain guiding alone provides only a linearly increasing coherence radius (see section 4.2).

With the assistance of refraction, a coherence radius comparable to the beam size was achieved with 36 cm long capillary length. Evidence of near full spatial coherence requires measurements using pinholes with separation comparable to the beam size. To clarify the point, we positioned the pinholes closer (15.7 cm) to the capillary exit. The spatial profile of the laser beam at this position was previously measured [57] and verified during these

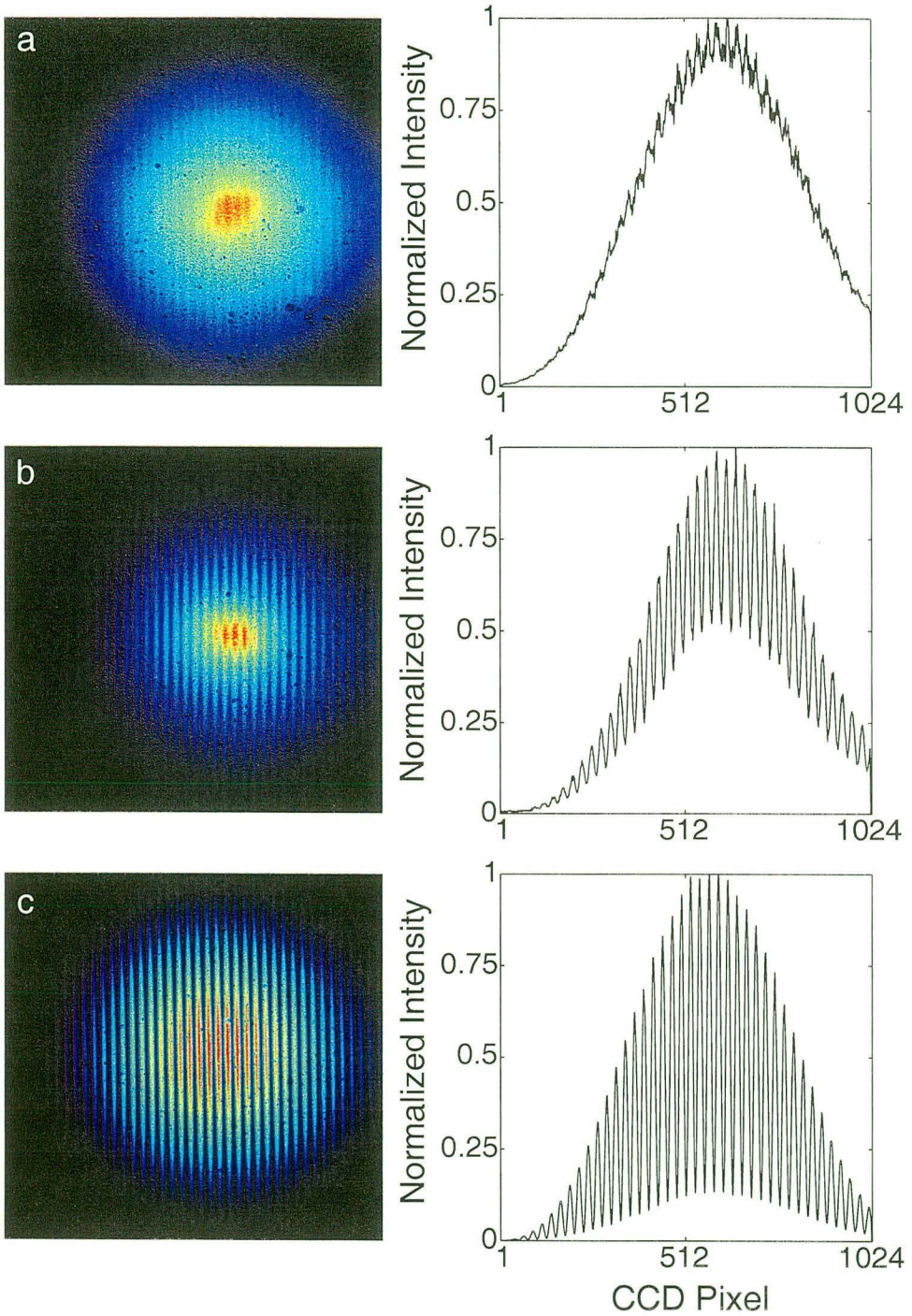

Figure 4-7. Interferograms and their lineouts showing the coherence buildup of the laser beam with increasing capillary length. The capillary lengths are (a) 18, (b) 27, and (c) 36 cm. The lineouts are obtained by vertically integrating 15 pixels of the CCD images.

experiments by scanning a single pinhole across the beam. Refraction causes a ring-shaped beam profile with a peak-to-peak diameter of approximately 950 μm. (See Fig. 4-8)

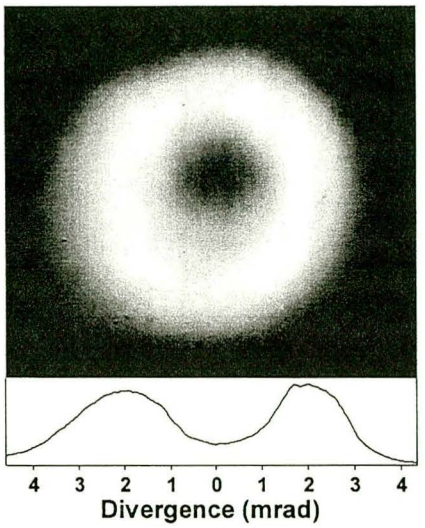

Figure 4-8. Ring-shaped beam profile of the 46.9-nm EUV laser, showing evidence of strong refraction. [57]

Fig. 4-9 (a) and (b) show the obtained interferograms and their lineouts with pinhole separations of 300 and 680 μm. In (a), visibility as high as 0.8 is observed. In (b), the large pinhole separation, combined with laser divergence, causes a large displacement of the two Airy patterns, so that they are no longer completely overlapping. The large visibility variations in different regions of the interferogram are the result of the intensity differences between the partially overlapped Airy patterns [59]. Maximum fringe visibility, ~0.55, occurs where the intensities of the two Airy patterns are equal (near the central region). Zero visibility occurs where there is a null in one of the Airy patterns. The degree of coherence $|\mu_{12}|$, determined from the maximum value of the visibility, is equal to 0.8 and 0.55, respectively.

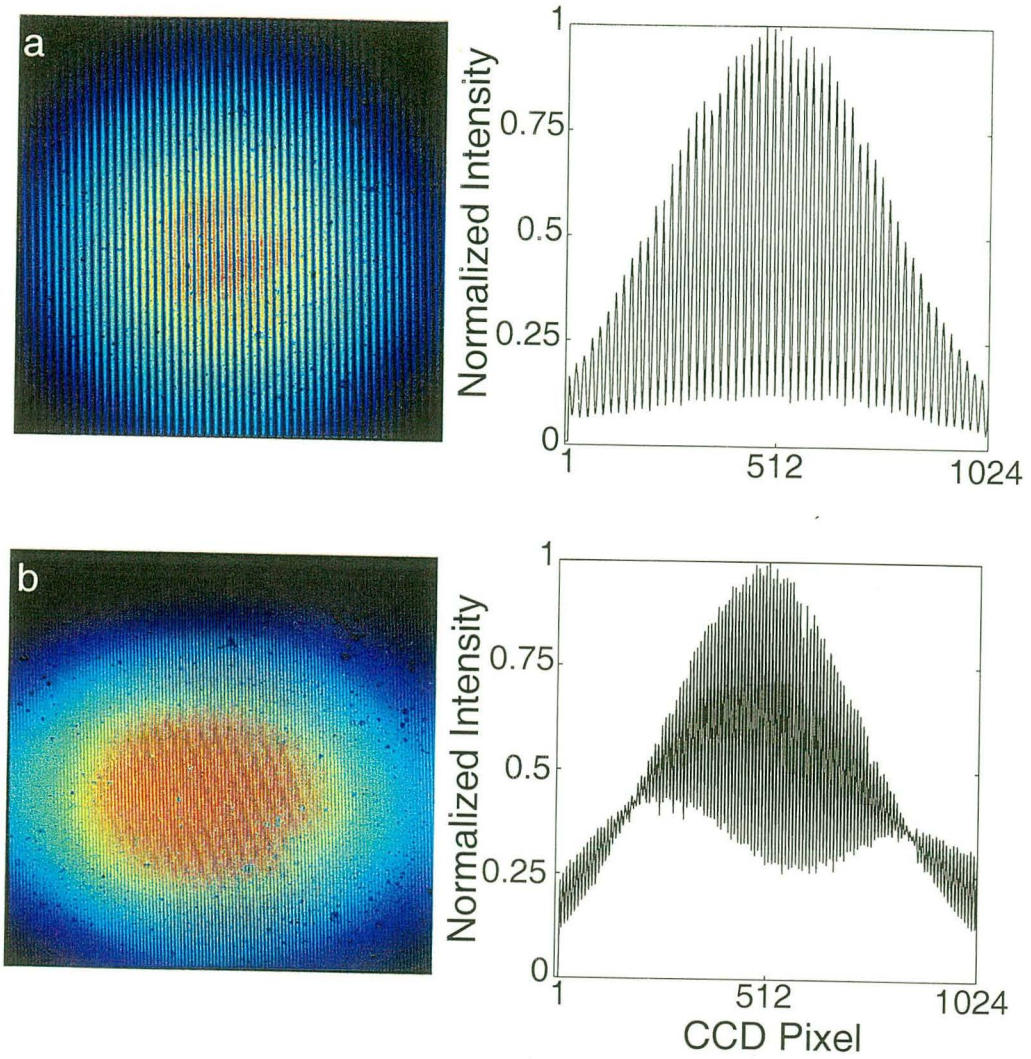

Figure 4-9. Interferograms and their lineouts obtained with two pinholes located at 15.7 cm from the capillary exit. The EUV beam at this position has a diameter of about 1 mm. The pinhole separations are a) 300 and b) 680 microns. Good fringe contrast observed at these large separations implies a high degree of spatial coherence throughout the beam.

These results indicate a very high degree of spatial coherence, essentially throughout the entire laser beam. Fig. 4-10 shows the experimental data together with a Gaussian profile of degree of coherence curve with an assumed coherence radius R_c = 550 μm. Considering the

small size of the laser beam (~1 mm), we have observed a spatial coherent area containing almost half the laser power, corresponding to an average coherent power of more than 1mW. A stricter convention, sometimes used to define coherent area, allows $|\mu_{12}|$ to drop only to a value of 0.88 ($e^{-1/8}$) [17]. Use of this stricter criterion would reduce the coherence radius to $R_c/2$. Even so, about 1/8 of the total power, or ~0.4 mW, is spatially coherent. Moreover, since this high coherent power is generated in only 4 pulses per second, with pulse width of 1.5 ns each, the laser's peak coherent power is estimated to reach 6×10^4 W. The coherent power can be focused to a spot limited only by diffraction. Assuming a 1-micron focus spot, the intensity would approach 10^{13} Wcm^{-2}.

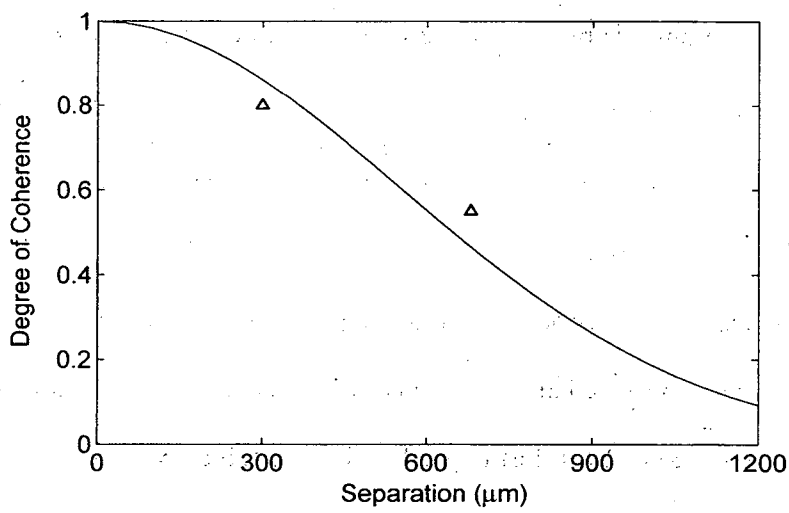

Figure 4-10. Measured degree of coherence, $|\mu_{12}(\Delta x)|$, of the laser beam vs. separation between two pinholes at 15.7 cm from the exit of the capillary. The solid line is for an assumed Gaussian profile $|\mu_{12}(\Delta x)|$ with a coherence radius Rc = 550 microns. The EUV beam at this position has a diameter of about 1 mm.

4.2.3 The 46.9-nm Laser as a Coherent Source

A coherent source should also be temporally coherent. This laser has a spectral bandwidth of $\Delta\lambda/\lambda \leq 1 \times 10^{-4}$, corresponding to a longitudinal coherence length longer than 300 μm, sufficient for most applications. Therefore it can be regarded as temporally coherent.

Previous experiments on that laser's beam divergence have shown that this laser can be well approximated as originating from a virtual source located ~5 cm inside the capillary. We can estimate the size of this source using the van Cittert-Zernike theorem. To produce the same Gaussian coherence profile with $R_c = 550$ μm, the equivalent incoherent source should have a diameter (RMS) of $d_s = \lambda z/\pi R_c = 5.4$ μm (see section 2.1.2). With a measured divergence angle of 7 mrad (2θ) [54] and an average power of 3.5 mW, the brightness of this source is then ~ 1.6×10^{17}, in units of photons s^{-1} mm^{-2} $mrad^{-2}$ within 0.01% spectral bandwidth. The peak brightness of this laser reaches a value of 2×10^{25}, making it the brightest EUV source in the world, all the more remarkable in that it is entirely contained on a small optical bench. No other EUV source, independent of its size, is presently capable of simultaneously generating such high average coherent power and peak spectral brightness.

In summary, we have observed an extraordinarily high degree of spatial coherence in a high average power soft x-ray laser beam produced by a tabletop device. The results were obtained by single pass laser amplification in a very long capillary plasma column using intrinsic mode selection mechanisms. The availability of full spatial coherence in tabletop EUV laser beams with high average power and extremely high spectral brightness opens new opportunities in science and technology.

4.3 Focusability of the 46.9-nm EUV Laser

High peak power and high spatial coherence from the 46.9 nm EUV laser prompts interest in its possible applications in nonlinear EUV light-matter interaction. One key issue is how small we can focus the EUV beam. High spatial coherence is necessary to achieve diffraction-limited focusing. However, spatial coherence alone is not enough. As discussed in chapter 2, full spatial coherence only implies a single spatial mode. The mode, however, is not necessarily well-behaved (like TEM_{00}), and may not be able focusable to a spot size of λ/NA. As stated in the last section, the high spatial coherence of this EUV laser comes from the very small number of guided modes inside the plasma. The phase and intensity distributions of the guided modes are determined by spatial profiles of the gain and refractive index inside the plasma, and they may not be the lowest order Gaussian modes. The ring-shaped beam profile seen in Fig. 4-8 suggests that the guided radiation is altered significantly by refraction, and is far from the fundamental Gaussian mode. An experiment [60] investigating the EUV beam's focusability is described in the following section.

4.3.1 Experiment Setup

Fig. 4-11 shows the focusing experiment setup. The laser beam is first reflected by a plane mirror and then focused by a spherical mirror. Both mirrors are 1-inch in diameter and coated to have 30% reflectivity at 46.9 nm. The plane mirror has a small hole in the center, which lets the focused light go through to form a focal spot after the mirror. This configuration is designed to have near-normal incidence at the spherical mirror, avoiding the aberration caused by off-axis illumination. A knife-edge is mounted on an x-y stage to perform scans of the light beam at different focal planes. The stage is driven by a computer-

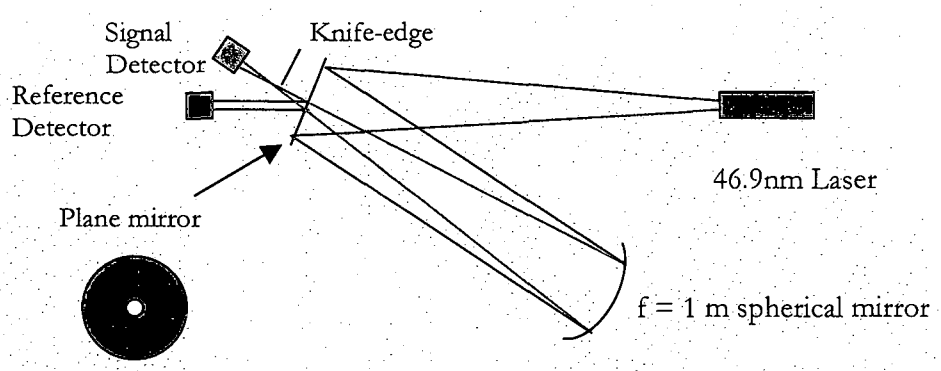

Figure 4-11. Experiment setup for measuring the focusability of the 46.9nm EUV laser.

controlled motor, having a minimum step size of 4 nm. A vacuum photodiode records intensity variations during the experiment. The signal is transmitted to, and stored in a digital oscilloscope for further analysis. The laser was operated at 0.5 Hz while the motor speed is controlled to ensure at least 50 shots are recorded in the range from 10% to 90% of maximum intensity. The hole in the plane mirror also leaks part of the laser beam to a reference detector. This reference is used to normalize the signal, thus reducing errors due to the shot-to-shot intensity fluctuations. Since the spatial profile of the laser beam is donut-like [Fig. 4-8], the small hole in the center has little effect on the beam focusing. The focusing mirror has a radius of 2 meters. This long focal length is selected to serve the main purpose of our experiment, which is to study the intensity profile of the focused light beam, rather than trying to reach high intensity by very tight focusing. It also eases the requirements on the optics and coating process, minimizing optical aberrations. The distance from the laser to the plane mirror is 1.7 m, and 1.3 m from the plane mirror to the spherical mirror, giving a total folded path length of about 3 m. The focus is about 15 cm behind the plane mirror.

4.3.2 M^2 Characterization of Light Beam

The focused x-ray beam is characterized in terms of an M^2 factor, which is a common practice for determining the beam quality of a laser beam [61]. In general, the propagation of a light beam can be described as:

$$W_x^2(z) = W_{0x}^2 + (\frac{M^2\lambda}{\pi W_{0x}})^2 (z - z_{0x})^2 \tag{4-2}$$

where z denotes the propagation distance and W_x is the spot size of the beam (x denotes one transverse direction), which is related to the intensity standard deviation σ_x as $W_x = 2\sigma_x$. Subscript "0" in Eq. (4-2) denotes the waist (the smallest spot). The variance σ_x^2, which plays an important role theoretical beam propagation analysis, is defined as

$$\sigma_x^2 = \frac{\iint x^2 I(x,y)dxdy}{\iint I(x,y)dxdy}$$

The beam diameter is $d_x = 2W_x = 4\sigma_x$. Using beam diameter d_x to calculate the divergence angle θ, the M^2 can be found to be

$$M^2 = (d_0 \cdot \theta)/(4\lambda/\pi) \tag{4-3}$$

A perfect single TEM_{00} mode laser beam would have a M^2 factor equal to one, corresponding to the diffraction-limited case. Deviations from this ideal case, such as partial coherence in a multi-mode beam, or an imperfect near-Gaussian intensity distribution, correspond to a higher M^2 factor.

To measure the M^2 factor, beam intensity profiles I(x,y) as a function of propagation distance z are needed. For our experiment involving high intensity EUV and an irregular transverse profile, we use a scanning knife-edge technique to measure the beam profile. Although in principle complete 1-D intensity distribution could be obtained by the knife-

edge profile, the shot-to-shot noise is usually too strong to get reliable results. On the other hand, if only the beam size is of interest, one can choose a clip level ε ($0< \varepsilon <0.5$) and the corresponding "clip width" D_c (defined as the distance the knife-edge moves from where the pass-through intensity is εI_{max} to where it rises to $(1-\varepsilon)I_{max}$) would be directly related to σ_x. Detailed calculations regarding the adequate choice of clip level and the scale factor used to convert D_c to standard deviation σ_x are presented in Ref. 62. We use their analysis to select a clip level of 20% and the corresponding scale factor of $D_c/\sigma_x = 2$, taking into account that our beam profile is somewhere between the donut mode and the ring mode. (See Fig. 4-12) Therefore, for our experiments, the relationship between beam diameter and the 20% to 80% D_c would be $d_x = 4\sigma_x = 2D_c$.

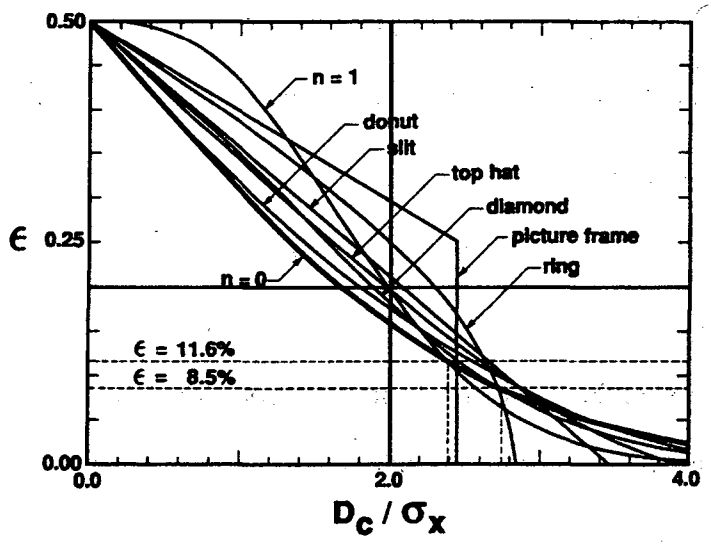

Figure 4-12. Choice of clip level and the scale factor in knife-edge experiments for different beam profiles. The figure follows Ref. 62. In our experiments, we choose a clip level of 20%, with a corresponding scale factor of 2.0.

4.3.3 Results

Using the method mentioned above, we measured the beam diameter at 9 positions ranging from –38 mm to 90 mm from the focus. Figure 4-13 shows an actual knife-edge scan data at a position where smallest spot is found. For a 20% clip level, the corresponding measured diameter is 80 microns.

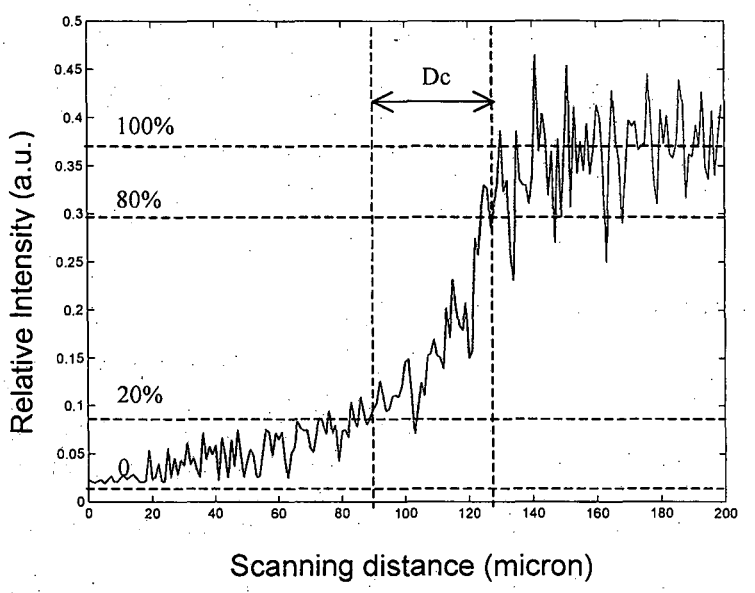

Figure 4-13. Knife-edge scanning data at a position close to focus. The beam diameter is 80 μm, decided by $d_x = 2Dc$ as described in the context. The dashed lines are shown to illustrate how the 20% clip level is applied to the experiment data.

Figure 4-14 shows the measured beam diameters at the 9 positions. The beam size increases linearly from data point No. 6 to No. 9, corresponding to a divergence angle of 12 mrad. Assuming the smallest diameter observed, 80 μm, is the waist, this will give M^2 = 16

according to Eq. (4-3). Two curves calculated using Eq. (4-2) with M^2 = 16 and 8 are shown for comparison.

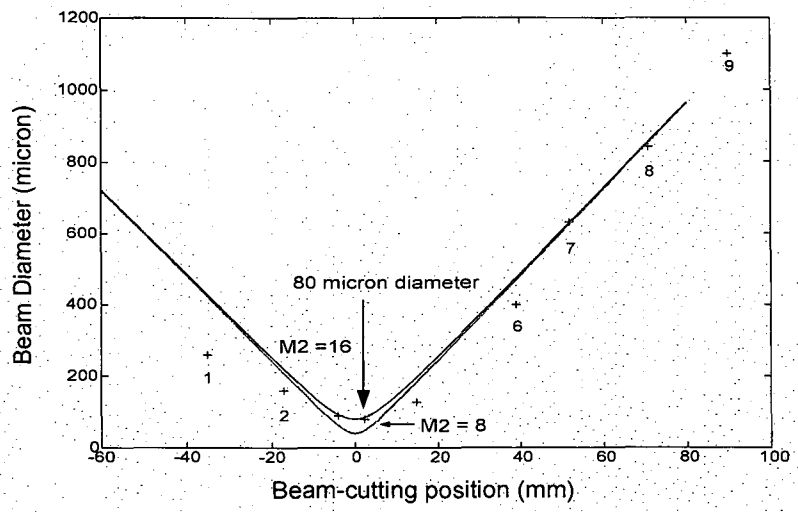

Figure 4-14. Beam diameters at different position. The divergence angle is 12mrad. Curves with M^2 of 16 and 8 are calculated using Eq. (4-2) and shown for comparison. It's clear that the beam quality is better than M^2 = 16.

M^2 of 16 is about 3 times larger than the prediction based on a wavefront measurement on this laser [63]. Several possible reasons could explain the discrepancy: first of all, our estimation of M^2 = 16 is actually quite conservative, with all nine data points below the curve. Thus 16 can be regarded as an upper limit of the actual M^2. Checking the curve of M^2 = 8, we can see that except for the region very close to the focus, it is similar to the curve for M^2 = 16. Even for M^2 = 8, seven of the nine data points are below the curve. This implies that accurate M^2 measurement would require more cuts within 10 mm of the focus to get a more reliable fitting of the waist diameter and the waist position. Secondly, experimental

errors or imperfections, such as misalignment, aberration in optics, optical table vibration, etc., would always tend to increase the spot size.

It should be noted that this experiment is not designed to reach a particularly small spot, nor a particularly high intensity. Although the 80-μm focus diameter looks large considering the 46.9 nm wavelength, it is obtained with a 1-meter focal length mirror, which corresponds to a numerical aperture of only about 0.01. Modestly tight focusing with a f = 50 mm mirror (N.A. = 0.2) would decrease the focus to several microns, and the peak intensity would reach 10^{13} Wcm^{-2} level. Availability of this high intensity and high photon flux would make it possible to observe new phenomena involving strong light-matter interaction in EUV/SXR region.

4.4 Comments on Lasers as EUV/SXR Source

As mentioned in section 4.1, lasing in short wavelengths requires significant pump power delivered on a short time scale. It is the main reason why early x-ray lasing experiments were pumped by the world's most powerful IR to near UV lasers [64]. The dependence on huge pump source limited laser's accessibility as coherent a EUV/SXR source. Fortunately, rapid progress made in the past decade has changed the situation and made tabletop EUV/SXR lasers a reality. Progress has been made in both the pump source and plasma excitation techniques. For the pump source, thanks to ultrafast laser technology, very high peak power is now available from compact femtosecond laser. Fast capillary discharge is another proven technique successfully producing high quality plasma suitable for lasing at EUV wavelengths, as we have seen in last section. For plasma excitation technique, the energy requirement for EUV/SXR lasing has been greatly reduced from 100's of Joules in early experiments to less

than 1 J nowadays [65]. The 46.9-nm laser is one outstanding representative of the remarkable achievement made by EUV/SXR laser community. It is impressive in many aspects: the compact size; efficient conversion from electricity directly to EUV photons; mJ-level pulse energy; dominating single lasing line with relative spectral bandwidth less than 0.01%; and an extremely high quality plasma with a favorable geometry (long and narrow) for approaching full spatial coherence. Its high pulse energy and good spatial coherence were utilized in diagnostics of dense plasmas [66, 67]. High contrast interferograms were obtained in single-shot experiments, allowing time-resolved plasma diagnostics. The shorter wavelength (compared with visible lasers) also enables it to detect higher electron densities (the critical density of a plasma is proportional to λ^{-2}). It is also attracting attention from chemists for studying reactions and catalysis of metal oxide by single photon ionization, overcoming the current limit of photon energy set by 118 nm laser [68]. In the coming years, compact EUV/SXR lasers will likely mature and be used as practical sources for a wide range of applications in the physical, chemical, and perhaps life sciences. With their low cost and compact size, they will provide more researchers access to the EUV/SXR wavelength region and stimulate new sciences and technologies.

The 46.9-nm wavelength is at the long wavelength end of the EUV/SXR spectrum. It is desired to have similarly compact, coherent sources at shorter wavelengths, for example around 13-14 nm for EUV lithography, and around 2.5 nm for "water window" biological microscopy. However, until now there is no other EUV/SXR laser demonstrating similar performance in terms of compactness, output energy and coherence. The reason is the unfavorable scaling of required power density versus wavelength for an ASE-based laser. Given the higher atomic energy levels, shorter lifetime of these levels, the smaller stimulated emission cross section at shorter wavelengths, and the difficulty to maintain a certain level of

population inversion, scaling to shorter wavelength EUV/SXR lasers requires pump power scale roughly as λ^{-4} to λ^{-5} [69]. For example, extending discharge excitation of the 46.9-nm laser to a Cd laser working at 13 nm, the scaling law requires an increase of delivered power by a factor of around 200. This will require a faster, more powerful discharge circuit, and increased efforts to maintain a uniform, high aspect ratio plasma column, in order to produce spatially coherent radiation at the mW average power level. Similar challenges also apply to laser-produced-plasmas sources. Currently although EUV/SXR lasing and even saturation have been realized at somewhat shorter wavelengths, they have utilized some very large-scale powerful lasers as pump sources. Pushing to shorter wavelengths, without compromising the compactness, is the most demanding challenge facing the EUV/SXR laser community today.

Chapter 5

High-order Harmonic Generation (HHG)

5.1 HHG Basics

Using infrared or visible lasers, shorter wavelength coherent radiation can be generated through nonlinear frequency mixing processes [70]. Harmonic generation is one well-known example. Recently the harmonic generation process has been extended to very high orders, reaching EUV and SXR wavelengths with widely available Ti:sapphire lasers. Naturally, the very high order nonlinear process requires extremely high pump intensity. Advances in ultrafast (< ps) laser technology [71] have made possible $>10^{15}$ Wcm^{-2} level of light intensity from very compact tabletop setups [72]. The interaction between atoms and such intense laser field has opened some fast-developing frontiers in nonlinear optics [73]. Among them, high-order harmonic generation (HHG) has attracted much attention as a promising method for the generation of ultrafast, coherent EUV/SXR radiation with a relatively simple setup.

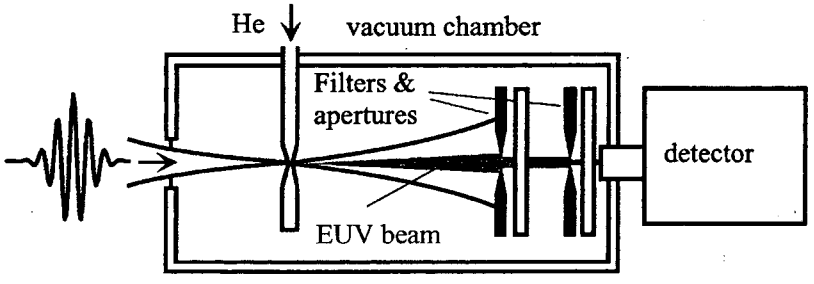

Figure 5-1. Typical experimental setup for high-order harmonic generation. EUV radiation can be generated by focusing an intense femtosecond duration laser beam onto the target, usually a gas jet. Modified from Schnürer et al., Ref. 74.

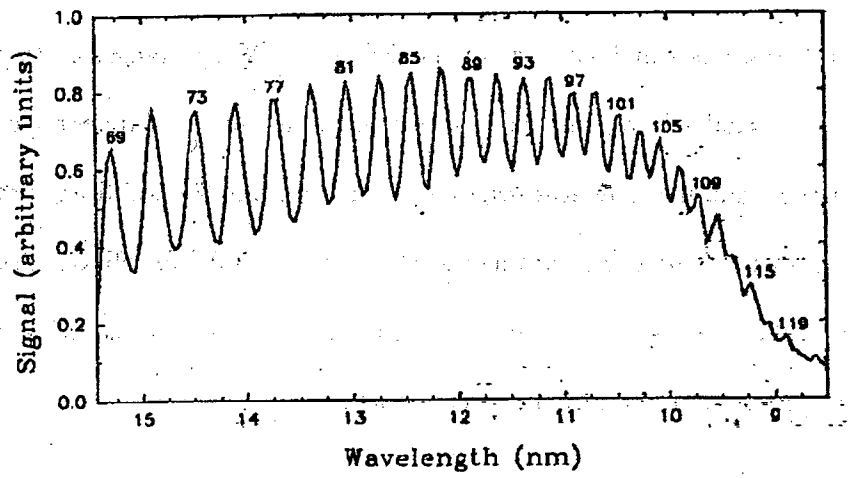

Figure 5-2. A measured spectrum of high-order harmonics. It is obtained by focusing a 1.053-μm neodymium laser beam into a helium gas jet. The focused intensity is ~ 3×10^{14} Wcm^{-2}. The "plateau" and cutoff regions can be clearly identified. From Tisch et al., Ref. 75.

In HHG, atoms exposed to a strong laser field can emit harmonic radiation at very high photon energies. Using intense femtosecond pulses, the harmonics have extended well into the "water window", with wavelength as short as 2.7 nm [76, 77]. This corresponds to harmonic order ~ 300. This appears to be an extension of the traditional harmonic generation process to very high orders, driven by an extremely intense laser pump. However, early experimental results suggested a mechanism. Typical HHG spectra exhibit a "plateau" region consisting of many odd harmonics, where the amplitude of the harmonics varies slowly, followed by a rather abrupt cutoff. (See Fig. 5-2) This is different from the traditional nonlinear process, where the higher order process is generally weaker than lower orders, and gradually fades away. The main reason for this difference is that HHG is a phenomenon in the so-called "strong-field regime", while the more familiar low order nonlinear process, for example second and third harmonic generation, is usually in the "perturbative regime" [73].

This difference is the result of the extremely high peak intensity of the laser field used in HHG. Typical intensities in HHG are in the 10^{14} - 10^{15} Wcm^{-2} range, corresponding to electric fields comparable to the internal atomic field. Consequently, different approaches are required to understand the nonlinear response of the medium. We will discuss this in detail in later subsections. For now, we introduce a semi-classical model for HHG, which captures the essence of the process and, when combined with quantum mechanical treatments of some aspects, provides a quite accurate physical picture.

5.1.1 Semi-Classical Model of HHG

The semi-classical model of HHG [78, 79] is based on a single active electron interacting with the light field in three steps. First, the high electric field of the laser suppresses the Coulomb potential barrier inside the atom, freeing the electron through quantum tunneling. Following this, the electron is treated as a free particle driven by the laser field. Some time later, around a half optical cycle later, the electron (driven by the linearly polarized field) returns to its parent ion. When they collide and recombine to the ground state, a photon is emitted with an energy of

$$\hbar\omega = I_P + K.E. \tag{5-1}$$

where I_p is the ionization potential of the atom and K.E. is the kinetic energy gained by the electron in the laser field. This process is illustrated in Fig. 5-3.

Whether or not the electron returns to the parent ion, and with what kinetic energy, depends on the phase of the light field at the time the electron tunnels free. We write the free electron's equation of motion in the incident laser's electric filed as:

$$\frac{dx(t)}{dt} = v(t)\,; m\frac{dv(t)}{dt} = -eE_0 \sin \omega t \tag{5-2}$$

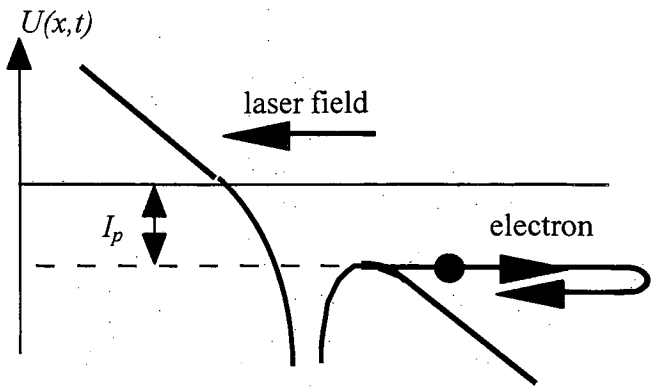

Figure 5-3. Illustration of the semi-classical model of HHG. An electron tunnels out of the atom with the help of a strong laser field which suppresses the Coulomb potential inside the atom. The electron is then driven by the laser field and may return to the atom as the linearly polarized laser field alternates its direction, recombining with the parent ion, and emitting a photon. The photon energy is the sum of ionization potential I_p and the kinetic energy obtained in the laser field. The emitted photon energy can therefore be much higher than the photon energy of the fundamental driving field. (Figure courtesy of H. C. Kapteyn, University of Colorado at Boulder)

where v(t) is electron's velocity and x(t) is its distance from the parent ion. Assuming the electron is released with zero velocity at time t_i and position x=0, the initial conditions are v(ti)=0 and x(ti)=0, and the solutions of Eq. (5-2) are:

$$x(t;t_i) = \frac{eE_0}{m\omega^2}[\sin\omega t - \sin\omega t_i - (\omega t - \omega t_i)\cos\omega t_i] \tag{5-3a}$$

$$v(t;t_i) = \frac{eE_0}{m\omega}[\cos\omega t - \cos\omega t_i] \tag{5-3b}$$

Eq. (5-3a) can be evaluated to see if x(t;ti)=0 has a solution other than t=ti, determining under what conditions the electron can be driven back to the ion. Eq. (5-3b) can then be used to determine the return kinetic energy as K.E.= ½ mv^2. The return energy is usually represented in terms of the ponderomotive energy, U_p, which is the mean kinetic energy of an electron executing harmonic oscillations in the laser field, where

$$U_p = e^2 E_0^{\ 2} / 4m\omega^2 \qquad (5\text{-}4)$$

The kinetic energy of the electron is then

$$K.E.(t;t_i) = 2U_p[\cos\omega t - \cos\omega t_i]^2 \qquad (5\text{-}3b')$$

Fig. 5-4 plots the electron's return energy as a function of its release time, limited to one optical cycle.

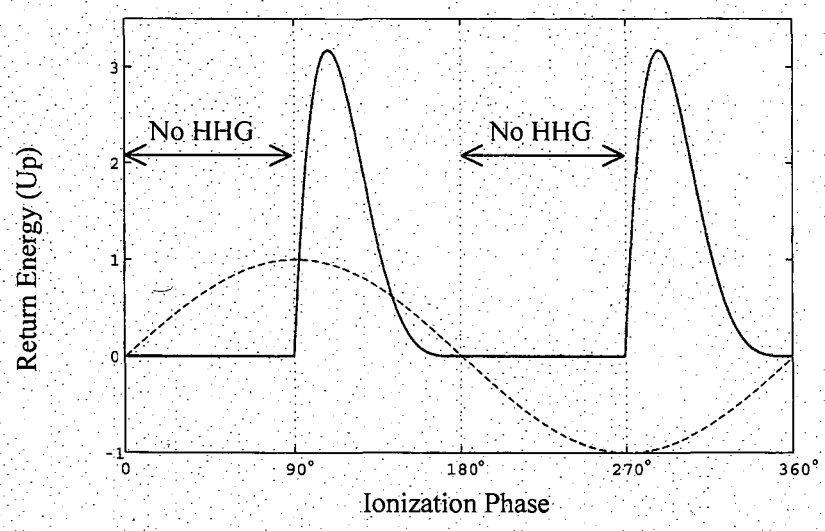

Figure 5-4. The electron's return energy (solid green line, in units of U_p) as a function of its release time. The maximum return energy is $3.17U_p$, corresponding to electrons tunneling free at a phase of ~108°/288° in the incident laser field. The electric field is shown in dash blue line as a reference. Electrons released at 0-90° and 180-270° will not return to the ion. Note that HHG process can happen twice each optical cycle.

From the figure, the maximum return (kinetic) energy is 3.17 U_p, giving a cutoff law of the maximum photon energy:

$$\hbar\omega|_{\max} = I_P + 3.17U_p \tag{5-5}$$

This explains the cutoff region observed in Fig. 5-2 and matches many experiment observations. The ponderomotive energy U_p can be much higher than the photon energy of the fundamental pump with available high intensity ultrafast lasers. In practical units, Eq. (5-4) can be written in terms of light intensity I and wavelength λ as:

$$U_p(eV) = 9.3\times10^{-14} I(Wcm^{-2})[\lambda(\mu m)]^2 \tag{5-4'}$$

Assuming $I = 10^{15}$ Wcm^{-2}, λ = 800 nm and He (I_p = 24.5 eV) as the active medium, the cutoff harmonic will have a photon energy of 220 eV; the HHG spectrum will extend well into EUV region. Modifications can be made to include the non-adiabatic effect associated with few-cycle pulses [77]. The HHG process happens symmetrically twice each optical cycle; this periodicity in time domain (T/2) corresponds to spacing of 2ω in frequency domain, explaining the odd harmonics observed. Another interesting observation is that for plateau harmonics (whose return energies are less than the peak value of 3.17 U_p), there are two possible release phases corresponding to the same return energy. Released at different times, the electrons will have different trajectories and spend different times in the continuum. Both trajectories contribute to the emission at the same photon energy. This has important consequence on the properties of HHG radiation; it will be discussed in later subsections.

The semi-classical model can be recovered as the classical limit of a fully quantum-mechanical (QM) analysis (the Lewenstein-Ivanov model [80]). For the purpose of coherence property discussions, the QM model has to be used to fully understand the

nonlinear response of the medium. In the following subsections we outline the QM analysis of HHG process for a single atom, and discuss the macroscopic effect (propagation /phasematching) in order to better understand the coherence properties of the generated harmonic fields.

5.1.2 Nonlinear Polarization for HHG

In the harmonic generation processes, harmonic fields are driven by the induced nonlinear polarization. For a single atom, we use $\vec{p}^{NL}(q\omega)$ to denote the nonlinear polarization at the q-th harmonic frequency. It is the Fourier component at qω of the dipole moment $\vec{p}(t) = -e\vec{x}(t)$:

$$\vec{p}^{NL}(q\omega) = \int \vec{p}(t)\exp(iq\omega t)dt \tag{5-6a}$$

The dipole moment in QM description is

$$\vec{p} = -e\vec{x} = -e\left\langle \psi(\vec{x},t)\middle|\vec{x}\middle|\psi(\vec{x},t)\right\rangle \tag{5-6b}$$

the wavefunction $\psi(\vec{x},t)$ evolves according to the Schrödinger equation

$$i\hbar\frac{\partial}{\partial t}\left|\psi(\vec{x},t)\right\rangle = [H_0 + H_{\text{int}}]\left|\psi(\vec{x},t)\right\rangle$$

where $H_0 = \frac{-\hbar^2}{2m}\nabla^2 + V(\vec{x})$ is the atomic Hamiltonian, describing the electron's motion under the Coulomb potential inside the atom, and $H_{\text{int}} = e\vec{x}\cdot\vec{E}(t)$ is the interaction Hamiltonian, describing the influence of the external field of the pump laser.

We mentioned earlier that the HHG process is different from the traditional harmonic generation process in that HHG is in a strong-field regime while the latter is in perturbative

regime. This difference has important subsequences for the properties of HHG radiation. In traditional harmonic generation process, the electric field of light is much weaker than the internal atomic field. Thus $H_{int} << H_0$, and it can be treated as a perturbation. The electron's wave function can then be expanded in a series, with higher terms corresponding to higher nonlinear orders. The nonlinear polarization can be generally written as [70]

$$\vec{p}^{NL(q)}(\omega) = \overleftrightarrow{\chi}^{(q)}(\omega;\omega_1,\omega_2,\cdots,\omega_q)\vec{E}(\omega_1)\vec{E}(\omega_2)\cdots\vec{E}(\omega_q) \tag{5-7}$$

which describes the q-th order nonlinear frequency mixing process, where $\overleftrightarrow{\chi}^{(q)}$ is the nonlinear susceptibility tensor. An important consequence of the perturbative expansion is that $\overleftrightarrow{\chi}^{(q)}$ is determined by the properties of the medium (energy levels, unperturbed wavefunctions, etc.) and the **frequencies** of the light involved; it does not have an explicit dependence on the **amplitudes** of the light. For harmonic generation within an isotropic medium pumped by linearly polarized light, which is typical of the HHG setup, Eq. (5-7) can be simplified to

$$p^{NL}(q\omega) = \chi^{(q)}E_L{}^q \tag{5-7'}$$

where we have dropped the vector and tensor notation. Thus, assuming $\chi^{(q)}$ to be a constant, the dipole moment at the q-th harmonic frequency simply follows the q-th power of the fundamental field. The solution to the coupled wave equation [70] for the harmonic field also becomes very simple. The spatial mode of the harmonics will just follow that of the pump. Specifically, if the pump laser has a TEM_{00} Gaussian mode, the q-th harmonic will also be TEM_{00}, with beam size shrunk to $1/\sqrt{q}$ of the pump beam [81]. The phase-space product of the q-th harmonic field will thus be q times smaller (both the beam waist and divergence angle is $q^{1/2}$ times smaller) than that of the fundamental, scaling with the

wavelength. This is consistent with the discussion in chapter 2.

The perturbation treatment implies the preservation of coherence in harmonic generation. However, in the strong field regime, where H_{int} is comparable to H_0, the solution to Schrödinger equation cannot be obtained by a perturbation expansion. A strong field approximation has been developed to simplify the full QM model [80, 82]. Based on that model, the dipole moment can be expressed in the form of an integration over all possible quantum paths as [83]: (atomic units are used here, following Ref. 83)

$$\vec{x}(t) = i\int_0^t dt' \int d^3\vec{P}\{\vec{D}^*(\vec{P}-\vec{A}(t))\exp[-iS(\vec{P},t,t')]\vec{E}(t')\vec{D}(\vec{P}-\vec{A}(t'))\} + c.c. \quad (5\text{-}8)$$

Here $\vec{P} = \vec{v} + \vec{A}(t)$ is a canonical momentum with $\vec{A}(t)$ denoting the potential vector. $\vec{D}(\vec{v}) = \left\langle \vec{v}\middle|\vec{x}\middle|0\right\rangle$ is the field-free dipole transition matrix element. The quasi-classical action, $S(\vec{P},t,t')$, is

$$S(\vec{P},t,t') = \int_{t'} dt''\left(\frac{[\vec{P}-\vec{A}(t'')]^2}{2} + I_p\right) \quad (5\text{-}9)$$

Eq. (5-8) can be interpreted in the spirit of Feynman's path-integral [84]; it is a sum of probability amplitudes over all possible starting times and paths corresponding to the three-step semiclassical model. The terms within the integral can be divided into the transition into continuum at time t', $\vec{E}(t')\vec{D}(\vec{P}-\vec{A}(t'))$; free electron propagation until time t ($\exp[-iS(\vec{P},t,t')]$); and recombination (transition back to the ground state, $\vec{D}^*(\vec{P}-\vec{A}(t))$).

5.1.3 The Two Trajectories and Intensity-Dependent Dipole Phase

Using a saddle-point analysis, the integral in Eq. (5-8) over all possible paths can be greatly reduced to a sum over a few relevant paths, which can be determined using the principle of

stationary action [85]. Of great value, this approach nicely connects the QM picture to the semi-classical model discussed earlier by identifying two quantum paths which dominate contributions to the dipole moment, each corresponding to a classical trajectory. The final dipole moment is the coherent sum of these paths, showing pronounced quantum interference effects. The most significant result from the path integral approach is that the **phase** of the dipole moment is **intensity-dependent**. Eq. (5-8) shows that the dipole moment acquire a phase from the free electron propagation in the continuum, which is represented by the quasi-classical action $S(\vec{P},t,t')$. For each of the two quasi-classical trajectories discussed above, the action can be roughly approximated by $-U_p\tau_s$ where U_p is the ponderomotive potential and τ_s is the electron's excursion time within the continuum [85]. The excursion time can be found to be near constant for most of the harmonics and thus the laser-induced dipole phase varies linearly with the intensity (the pondermotive potential is proportional to intensity) [86].

The intensity-dependent dipole phase means that the coherence of the pump field is not fully preserved in the nonlinear polarization. This is significantly different than the traditional (weak field) harmonic generation process, as discussed earlier. For HHG experiments, femtosecond pulses, either focused or guided in a wave-guide, are used. The intensity varies both in time (the pulse envelope) and space (the spatial mode). As a result, the dipole phase also varies both in time and space. These phase variations reduce both the temporal coherence and the spatial coherence of the HHG radiation.

The intensity-dependent dipole moment, including the contributions from the two trajectories, can be expressed as [87]

$$d_q(I) = A_1(I)\exp(-i\alpha_1 I) + A_2(I)\exp(-i\alpha_2 I) \qquad (5\text{-}10)$$

where A(I) denotes the strength and α is the phase coefficient, proportional to the excursion time for each trajectory. The two trajectories have different excursion times; one is short and the other is relatively long. We will use titles "short trajectory" and "long trajectory" to describe them. The short trajectory has a dipole phase only weakly depending on the intensity while the dipole phase of the long trajectory strongly depends on the intensity. These two components can in fact be spatially separated and exhibit different temporal coherence properties. Both can be explained in the framework discussed above. The spatially varying dipole phase (caused by the spatial mode of the pump) introduces a curvature of the phase front; we would expect the long trajectory to be more divergent due to this effect. The temporally varying phase (caused by the pulse envelope) introduces a chirp, or spectral broadening; we would thus expect the long trajectory to be less temporally coherent. This is indeed observed experimentally [87, 88]. (See Fig. 5-5)

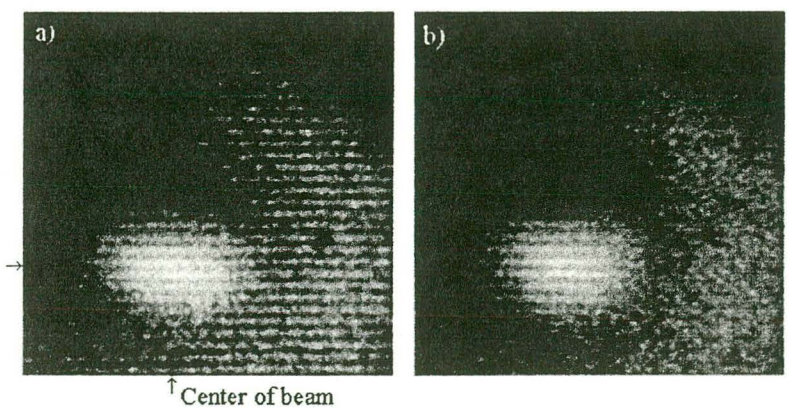

Figure 5-5. Effects of the two trajectories in a temporal coherence measurement of HHG. Interference pattern are recorded with a time delay between pulses of a) 0fs and b) 25 fs. Light in the center region is mainly from contribution of the short trajectory, which is less divergent and has longer coherence time. Light in the outer region is mainly from contribution of the long trajectory, and is less coherent. From C. Lyngå et al., Ref. 87.

5.1.4 Phase-Matching Effect

The above discussions are focused on the nonlinear response of a single atom. On the macroscopic scale, HHG radiation is the coherent addition of the fields due to all atoms in the interaction region. The total field is described in the coupled wave equation under the slowly varying envelope approximation, using the macroscopic polarization $\vec{P}^{NL}(q\omega)$ as the driving term [70], where $\vec{P}^{NL}(q\omega)$ is related to the single atom response by $\vec{P}^{NL}(q\omega) = n_a \vec{p}^{NL}(q\omega)$, where n_a is the atomic density and $\vec{p}^{NL}(q\omega)$ is the single atom polarization described in Eq. (5-6). Propagation and phase-matching across the field will strongly influence the final output of the HHG radiation and make it quite different from the nonlinear response of a single atom. It also offers the possibility of macroscopic control of the emission by isolating the contribution of a single trajectory. This has been extensive studied by shifting the focal position of the pump beam in gas jet experiments [84, 86, 89, 90]. This approach delineates the two contributions to the dipole phase variation associated with a focused Gaussian beam as the pump. One is the geometric phase change associated with propagation of the Gaussian beam, while the other is due to the intensity-dependent dipole phase, varying with the intensity across the focused beam. The best phase matching condition on-axis is that where the phase variation of the polarization over the interaction region is minimal, which occurs when the laser is focused before the gas jet. Changing the focal position can influence phase-matching for either trajectory, dramatically altering the beam spatial and temporal profile and spectrum. An example is shown in Fig. 5-6, in which the calculation was done by Salières et al. [89]. In the calculation, the parameters are selected to mimic typical experimental conditions. The pump laser (825-nm wavelength) is assumed to be Gaussian in both space (confocal parameter = 5 mm) and time (150 fs FWHM). The

peak intensity at focal plane (z=0) is 6×10^{14} Wcm^{-2}. The generating gas is neon.

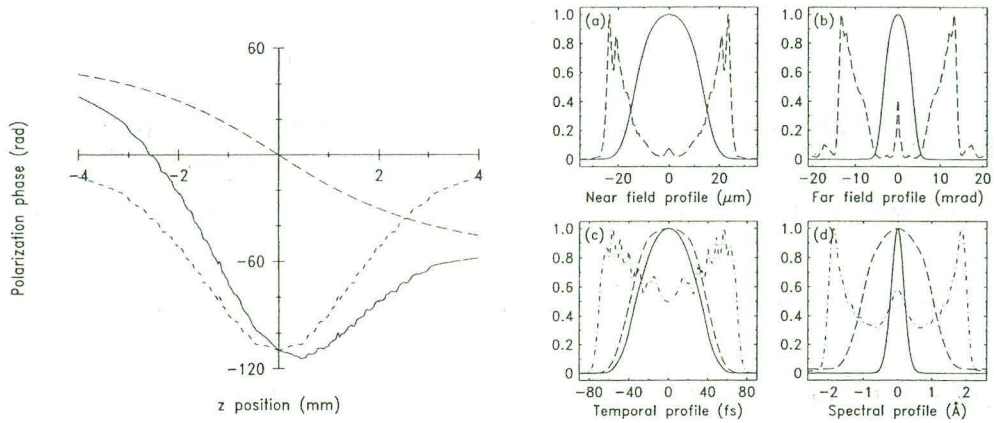

Figure 5-6. Coherent control of HHG process by changing the position of the laser focus relative to the generating gas. Left: Phase of the harmonic (q=45) polarization along propagation axis (solid line). The long-dashed line indicates the propagation of the fundamental, and the short-dashed line the dipole phase. The z=0 position is the focal plane. Right: (a) Near-field, (b) far-field, (c) temporal, and (d) spectral profiles of 45th harmonic. In (a) through (d), the solid line is the result obtained at z= 3mm, and the dashed line at z = -1 mm. The dot-dashed line in both (c) and (d) represents the result obtained at at z=0. From Salières et al., Ref. 89.

Simple optimization of HHG by positioning the focus to appropriate location is limited by the short interaction length of the gas jet setup. As a result, although fairly good spatial coherence [91] and beam quality [92] have been observed, they are still not approaching the full coherence limit. In following part of the chapter, we extend our analysis to guided HHG process inside a hollow fiber. Extended phase-matching over a long interaction region not only greatly improves the conversion efficiency to the phase-matched orders, but also results

in an essentially full spatial coherence.

5.1.5 Phase-Matched HHG in Hollow Fiber

The harmonic generation process is most efficient when phase-matching is achieved throughout the interaction region [70]. Since the real part of refractive index in the EUV/SXR wavelength region is less than unity [1], high harmonics travel at phase velocities faster than c. the speed of light in vacuum. As a result, free space propagation of the pump will not "catch" the harmonics. This phase mismatch will limit the effective interaction length and therefore limit the conversion efficiency.

The research group led by Profs. H. C. Kapteyn and M. M. Murnane utilized a hollow core fiber setup to realize phase-matched HHG over a long interaction distance [93], in which the phase velocity of the pump is controlled. For the guided pump light, the wave vector of propagation in the hollow fiber can be written as [93]

$$k_{laser} \approx \frac{2\pi}{\lambda} + \frac{2\pi n_a \delta(\lambda)}{\lambda} - n_e r_e \lambda - \frac{u_{nm}^2 \lambda}{4\pi a^2} \tag{5-11}$$

where λ is the vacuum wavelength, the second and third terms represent the dispersion due to the gas and the plasma (created by ionization), respectively, and the fourth term is due to the wave-guide effect of the hollow fiber. Here n_a is the atom density, n_e is the electron density, δ depends on the gas atom's dispersive property, and r_e is the classical electron radius. The wave-guide contribution in the last term, with a as the radius of the wave guide and u_{nm} is a constant corresponding to the guided mode structure [94]. The negative sign of the last two terms indicate that they increase the phase velocity of the pump, making it possible to be greater than c. By varying the gas pressure and the fiber radius, a balance can

be reached such that $qk_{laser} = k_{q\omega}$ (wave vector of the q-th harmonic), achieving phasematching where both the laser pump and the high harmonic has the same phase velocity, somewhat faster than c. This geometry increases the conversion efficiency of light into the EUV by up to two orders of magnitude over what would be possible with similar pulse energies in a free-space focus configuration [93].

The pump pulse propagates predominantly in the EH_{11} mode (EH, electric hybrid) of the hollow core fiber, and the HHG is restricted to the central, most intense portion of the pump field [94]. This guided propagation eliminates the geometric phase variation along the propagation direction associated with a focused Gaussian laser beam (the long-dashed line in left panel of Fig. 5-6). The intensity variation along the propagation direction is also minimal, further eliminating the intensity-dependent phase variation of the harmonic dipole (the short-dashed line in left panel of Fig. 5-6). We expect this guided, quasi–plane wave interaction would favor phase-matching to the more coherent short trajectory and the long interaction length would further improve the coherence properties. In fact, the observed two orders of magnitude conversion efficiency enhancement in the phase-matched orders [93] suggests that an improvement of the temporal coherence is already present. In the next section, we show that extended phase-matching also results in good beam mode quality, and essentially full spatial coherence, in the generated EUV beam.

5.2 Observation of Full Spatial Coherence from a HHG Source

In this section we present spatial coherence measurements of EUV light generated through the HHG process with a phase-matched hollow-fiber geometry. The generated beam was found to exhibit essentially full spatial coherence. The work is part of collaborations with Profs. Kapteyn and Murnane's group at JILA, University of Colorado at Boulder [95].

5.2.1 Experiment Setup

In this work, light from a high-repetition-rate (5 kHz, ~0.8 mJ/pulse) Ti:sapphire laser system, operating at 760 nm with a pulse duration of 25 fs, was focused into a 10-cm-long, 150-μm-diameter, hollow core fiber filled with argon gas (Fig. 5-7). The EUV radiation was phase-matched at a pressure of 29 torr, resulting in emission of about three to five harmonics centered around a photon energy of 31 eV (odd harmonic orders, 17 through 23). A 0.55-μm-thick aluminum filter was used to remove the fundamental laser light and was immediately followed by the pinholes. In an image of the EUV beam 95 cm after the exit of the hollow core fiber (Fig. 5-8), the diameter of the EUV beam is 1 mm at the $1/e^2$ intensity point, with a slight ellipticity (~1.3) due to imperfections in the hollow-fiber shape. The beam divergence of < 1 mrad is consistent with a diffraction-limited source size of 40 μm diameter within the fiber. Using a vacuum photo-diode, we measured a photon flux of ~2×10^{12} photons/s.

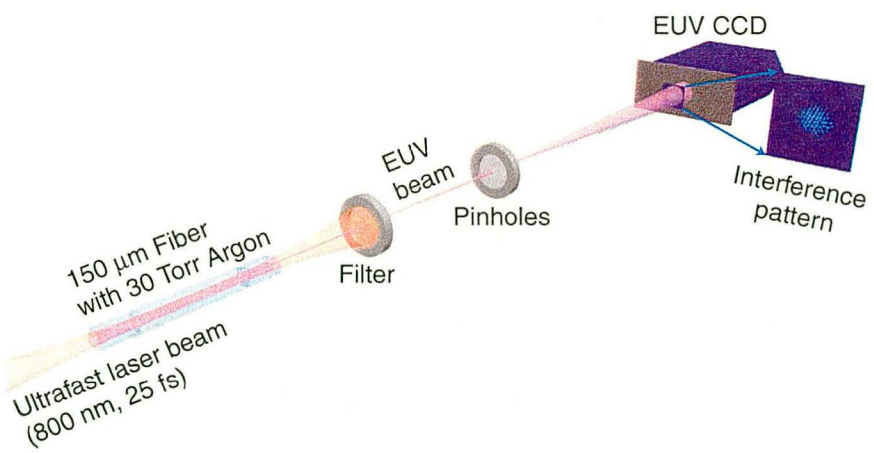

Figure 5-7. Experimental setup for the spatial coherence measurements of EUV light beam generated through HHG process in a hollow fiber.

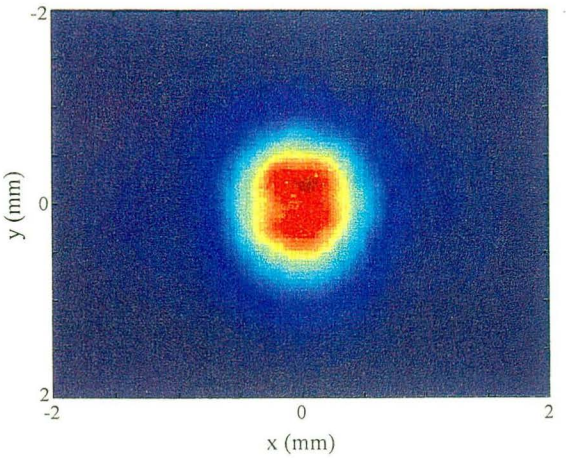

Figure 5-8. Beam profile of the EUV light measured 95 cm from the exit of the fiber.

5.2.2 Recorded Two-Pinhole Interference Patterns

Spatial coherence of the EUV light was measured using the double-pinhole interference technique described earlier in section 2.1.2. The fringe visibility was measured across the width of the EUV beam by sampling it with pinhole pairs separated by lateral distance varying from 142 to 779 μm. Laser-drilled apertures (National Aperture, Inc., Salem, NH) consisting of either 20- or 50-μm-diameter pinhole pairs, were placed 95 cm from the exit of the fiber. An EUV charge-coupled device (CCD) (Andor, Inc., Belfast, Northern Ireland) camera placed 2.85 m from the pinholes captured the diffracted image. Images of high dynamic range were captured with a CCD integration time of between 20 and 240 s (100,000 to 1,200,000 laser shots). Integration over a large number of shots demonstrates both the high spatial coherence and the long-term wavefront stability of the EUV beam. The EUV beam was sampled at 14, 24, 29, 38, 58, and 78% of the beam diameter using pinhole pair

separations of 142, 242, 292, 384, 574 and 779 μm, respectively (separations verified by a scanning electron microscope). Sample data are shown in Fig. 5-9.

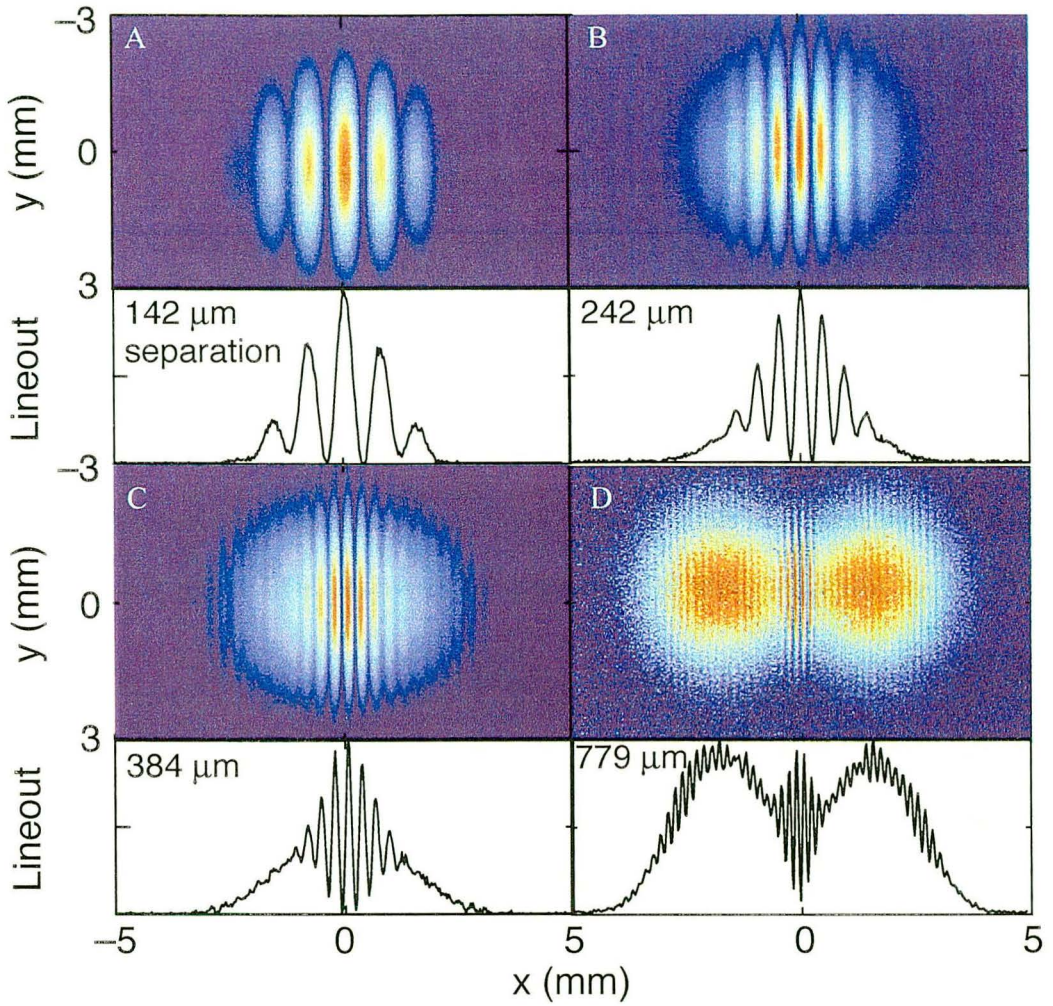

Figure 5-9. Interference patterns for the EUV beam diffracted by pinhole pairs of various separations, together with lineouts of the images. The separations are (A) 142, (B) 242, (C) 384, and (D) 779 μm. Blue represents minimum intensity, and red represents maximum intensity. Strong modulation (fringe visibility) indicates a high degree of spatial coherence.

5.2.3 Results

In the measured diffraction patterns, the fringe visibility varies across the pattern. The decrease of fringe visibility away from the central region is due to the limited temporal coherence as a result of the broadband radiation (several harmonics). In fact, Fourier analysis of the interference pattern over the entire field can yield information about the incident spectrum. A detailed mathematical analysis enables retrieving both the spatial coherence and spectrum information from the interferograms; we will describe the method in detail in the next section. The results of the spatial coherence analysis are shown in Fig. 5-10. It indicates that unit spatial coherence is maintained over most of the EUV beam. Even before performing a full analysis of the data as that in the next section, the high degree of coherence is indeed very convincing just by observing the extremely high fringe visibility of the interferograms.

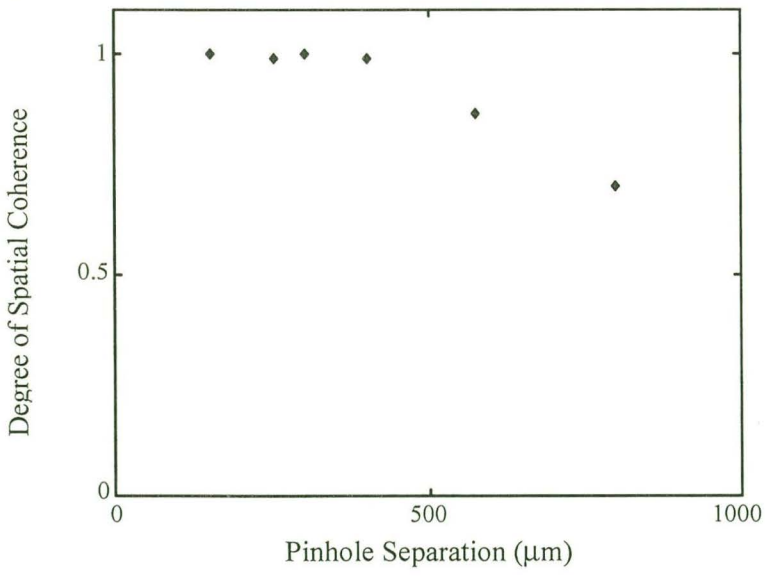

Figure 5-10. Spatial coherence of the EUV beam as a function of pinhole separation. The beam diameter is ~ 1 mm, with intensity profile shown in Fig. 5-8.

The entire setup, including the femtosecond laser system, EUV generation cell, imaging setup, and x-ray CCD camera, occupies 100 cm by 350 cm of optical table space. This compact, coherent, laser-like source of tabletop EUV radiation is extremely useful for applications such as high-resolution coherent imaging. This capability was demonstrated by performing Gabor holography as part of the collaboration experiment [95].

5.3 Two-Pinhole Interference Experiment with Polychromatic Light

In a standard two-pinhole coherence measurement the incident field is assumed to be quasi-monochromatic, so that temporal coherence effects are isolated from the measurement of spatial coherence. In the experiments described in previous chapters using undulator radiation and an EUV laser, the longitudinal coherence length of the sources are longer than the maximum path length differences from the CCD to the two pinholes, therefore the quasi-monochromatic assumption is valid. However, HHG sources generate broad-bandwidth radiation, having multiple harmonic orders. The interference pattern formed by illuminating a pinhole pair with such broad-bandwidth sources will thus contain both temporal and spatial coherence information regarding the source as well as the power spectrum. In this section we investigate this effect in detail and introduce an experiment in which we demonstrated that the power spectrum of the coherent EUV beam, consisting of four harmonic orders, can be measured by analysis of the far-field intensity distribution produced by a pinhole pair. Such a spectral measurement can be calibrated by a straightforward measurement of the geometry of the experiment, providing absolute wavelength and relative intensity information. This approach proves particularly useful in the EUV, since wavelength calibration to high accuracy can be achieved with straightforward measurements, and the only element that has a spectral response that must be separately

calibrated is the CCD. This experiment is, to our knowledge, the first spectral measurement of a non-monochromatic source by analysis of the pinhole-pair interference pattern at any wavelength. The experiment was also performed at JILA, University at Colorado, Boulder, as part of collaborations with Profs. Kapteyn and Murnane's group [96].

5.3.1 Theoretical Analysis

Our analysis is based on coherence theory as described previously in chapter 2. In the far field the path-length difference between two sampled portions of a field, P_1 and P_2 in Fig. 5-11(a) gives rise to an interference pattern that is determined by the spatial and temporal coherence of the source. This path difference introduces a time delay, $\tau = \Delta r / c = xd/(zc)$, that generates an autocorrelation, $\int E(t)E^*(t-\tau)dt$, of the incident field. The power spectrum is the Fourier transform of the field auto-correlation (see section 2.1.1 regarding temporal coherence). Therefore, measuring the pinhole-pair interference pattern is equivalent to measuring the power spectrum of the field that is incident on the pinhole pair, provided that the field is spatially coherent and the spatial extent of the field autocorrelation is less than the width of the Airy pattern from a single pinhole in the observation plane. This connection has been known for some time [97] but to date has not been exploited for a determination of the power spectrum of a light field.

The exact relationship between the interference pattern and power spectrum can be derived as follows. The intensity distribution in the observation plane, with equal illumination of two pinholes, can be written as

$$I(x) = 2I^{(0)}(x)[1 + \gamma_{12}(x)\cos(2\pi \frac{d}{\lambda_0 z} x)] \qquad (5\text{-}12)$$

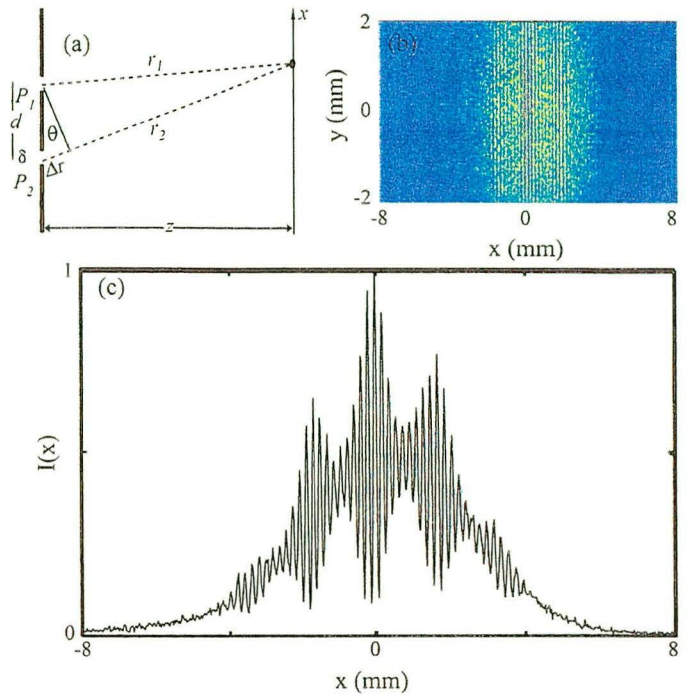

Figure 5-11. (a) Schematic of the experimental setup, where we have recorded (b) the EUV interferogram (note that the intensity is weakest for blue and strongest for red colorings), and (c) average of (b) along the y axis. The experimental conditions used are z = 2.85 m, δ = 20 μm and d = 575 μm.

where $I^{(0)}(x)$ is the Airy distribution due to diffraction through a pinhole of width δ , d is the pinhole separation, z is the distance from the pinhole pair to the observation plane, λ_0 is the central wavelength of the light field, and γ_{12} is the complex degree of mutual coherence (see the geometry in Fig. 5-11(a)). Here the time delay has been transformed to the spatial coordinate $x = zc\tau/d$. For quasi-monochromatic light, the fringe visibility, $V = [I(x)_{max} - I(x)_{min}] / [I(x)_{max} + I(x)_{min}]$, equals to the degree of spatial coherence $|\mu_{12}|$, where $\mu_{12} = \gamma_{12}(0)$ is the complex coherence factor. The τ -dependence of $\gamma_{12}(\tau)$ can be included in a simple

sinusoidal oscillation term. (See discussions in section 2.1.2 from Eq. (2-6) to Eq. (2-9)). More generally, and more relevant here (for polychromatic light) [98],

$$\gamma_{12}(\tau) = \Im^{-1}\{S(v)\mu_{12}(v)\} \tag{5-13}$$

where $\Im$ denotes Fourier transform and $S(v)$ is the power spectrum normalized such that $\int_0^\infty S(v)dv = 1$. From Eq. (5-12), the interference pattern from a pinhole pair, as shown in Fig. 5-11(b), will have a broad spatial extent determined by the Airy distribution from a single pinhole. The modulations within the Airy disk are due to interference of radiation from the two pinholes. The slow modulations are due to the interference of the broad bandwidth associated with several harmonics, while the fast oscillations are determined by the geometry and the central wavelength. The depth of modulation is determined by the spatial coherence of the beam, and therefore this technique can also be applied to light fields with imperfect spatial coherence.

Equation (5-12) is best analyzed in the spatial frequency domain. A Fourier transform of Eq. (5-12) gives

$$\Im\{I(x)\} \equiv F(f_x) = 2T(f_x) \otimes \{\delta(f_x) + \frac{1}{2}S(f_x)\mu_{12}(f_x) \otimes [\delta(f_x - f_0) + \delta(f_x + f_0)]\} \tag{5-14}$$

where $\otimes$ is the convolution operator, $T(f_x) = \Im\{I^{(0)}(x)\}$ is a dc spike, $\delta(f_x)$ is the Dirac delta function, $f_0 = d/(z\lambda_0)$ is the carrier spatial frequency due to the pinhole-pair interference pattern, and $S(f_x)\mu_{12}(f_x) = \Im\{\gamma_{12}(x)\}$. Thus, a Fourier transform of the interferogram produced from a Young's pinhole-pair measurement should yield three terms: a dc term corresponding to a spike at zero (or dc) frequency and two terms containing information on the power spectrum convolved with the dc spike and weighted by the spatial coherence function at that frequency. Equation (5-14) yields information on only the

product of the power spectrum and the coherence factor at any frequency, however, we can retrieve useful information on both the spatial coherence and spectrum based on it, as discussed below.

1) Determination of Spatial Coherence

In the case of quasi-monochromatic radiation, the degree of spatial coherence μ_{12} is twice the height of one of the sideband terms after the maximum value of the dc spike has been normalized to unity. More generally, we can sum the integral of the sidebands and divide by the integral of the dc term, resulting in the following expression

$$\overline{\mu}_{12} = \frac{\int T(v) \otimes S(v - v_0)\mu_{12}(v - v_0)dv + \int T(v) \otimes S(v + v_0)\mu_{12}(v + v_0)dv}{\int 2T(v)dv} \qquad (5\text{-}15)$$

This expression defines an average degree of spatial coherence ($\overline{\mu}_{12}$) weighted by the spectral intensity ($\overline{\mu}_{12} = \int S(v)\mu_{12}(v)dv$). In section 5.2 the spatial coherence of the EUV beam was determined by this method. We performed a Fourier transform of the data, identified the sidebands, and integrated to obtain the average spatial coherence. In Fig. 5-9(D), the two Airy distributions are separated by ~ 3.2 mm, compared with the pinhole separation of 779 μm. This is due to the fact that the pinholes are sampling the curvature of the EUV phase front, and the local tilt is larger than the divergence due to diffraction. Under such circumstance, Eq. (5-12) does not apply and the Fourier transform method is not valid. Nevertheless, in the central region where the two diffraction patterns have equal intensity, the observed fringe visibility can be used as a minimum measure of $|\mu_{12}|$. For all other pinhole separations, the two methods agree.

2) Determination of Spectrum

Eq. (5-14) provides a way to directly obtain $S(\nu)\mu_{12}(\nu)$. If the spatial coherence $\mu_{12}(\nu)$ is constant over all the frequencies, then $S(\nu)\mu_{12}(\nu)$ provides the shape of the spectrum, $S(\nu)$. It is not always true that $\mu_{12}(\nu)$ is constant over all frequencies; however, where essentially full spatial coherence is observed, we can assume $\mu_{12}(\nu)$ is close to 1 for all frequencies, and thus constant. For example, in the experiments presented in last section, we obtained an average degree of spatial coherence, $\int_0^\infty S(\nu)\mu_{12}(\nu)d\nu$, of ~ 0.9. This indicates a small spectral deviation of the spatial coherence. In this case, we can determine the spectrum of the radiation by performing Fourier transforms of the interferograms. The details are presented in the next subsection.

5.3.2 The Spectrum Measurement Experiment

For the experiment we used 27-fs laser pulses generated by an amplified Ti:sapphire laser system at a 5-kHz repetition rate, a wavelength of 800 nm, and with energy of ~10 mJ per pulse. The pulse is focused into a 10-cm-long, 150-μm-diameter hollow-core fiber filled with 30 Torr of Ar gas such that the HHG process is phase matched and peaked at the 21st harmonic. A 0.35-μm-thick Al filter is used to remove the fundamental IR beam, after which a 20-μm-diameter pinhole pair with a 575-μm center-to-center separation (as verified by a scanning electron microscope) is placed 95 cm from the fiber exit. The far-field diffraction pattern observed 2.85 m from the pinhole pair with an exposure time of 60 s is shown in Fig. 5-11(b). An additional 0.35-μm-thick Al filter placed immediately before the CCD camera eliminates unwanted IR scattered light. The HHG spectra were also measured with

an imaging EUV spectrometer (Hettrick Scientific HiREFS SXR-1.75), which measures the product $S(v)\eta(v)$, where $\eta(v)$ is the relative efficiency of the spectrometer.

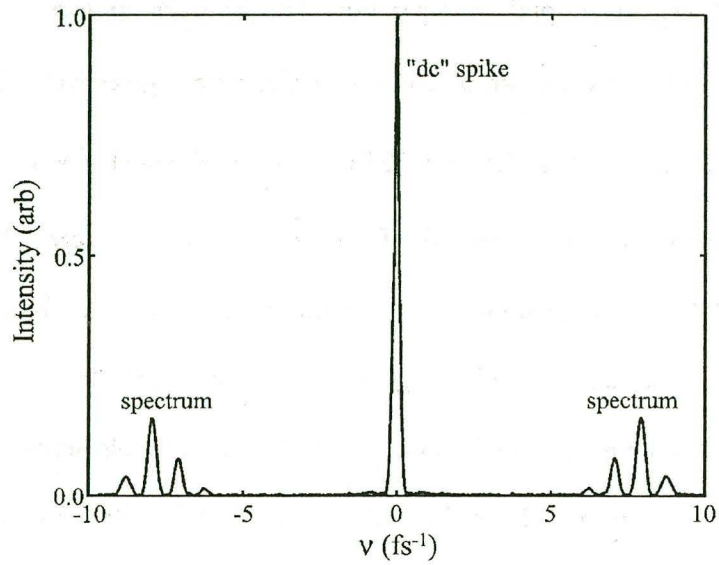

Figure 5-12. Fourier transforms of Fig. 5-11(b), showing the spatial frequency distribution scaled in optical frequency. The central frequency observed in the sidebands corresponds to the 21st harmonic of the laser at 800 nm.

Fig. 5-12 shows the spatial frequency distribution along the x dimension, obtained from a Fourier transform of the interferogram produced by the pinhole pair [shown in Fig. 5-11(b)]. The high quality of the data of Fig. 5-12 is due in large part to the fact that the two-dimensional Fourier transform of the interferogram (with substantial random detector noise) implicitly averages over all 256 lines of data in the y dimension. In essence, we take 256 simultaneous single-shot field autocorrelation traces; the interferogram averaged over all y is shown in Fig. 5-11(c). The optical frequency axis is obtained by multiplication of the spatial frequency axis by zc/d. Therefore, the pinhole separation and the distance to the detector determine the calibration of the wavelength axis in Fig. 5-13. The three terms expected from

Eq. (5-14) are clearly shown in Fig. 5-12. The resolution of a spectral measurement is limited by the width of the dc spike, which is proportional to the diameter of the pinhole and inversely proportional to the pinhole separation. The dc spike appears at the zero spatial frequency and has a fractional width of $\Delta v / v_0 = 0.022$, which agrees well with the predicted resolving power of $\Delta v / v_0 = 0.8\delta / d$, or 0.027 for our experimental geometry.

The percent error in the optical frequency calibration can be written as $\Delta v / v = \Delta z / z + \Delta d / d$ and demonstrates that the accuracy of the frequency scaling is directly related to the accuracy of the geometry measurement. In this experiment the distance to the detector is measured within $\sim \pm 0.02\%$ and pinhole separation is measured within ~0.008%, with an overall accuracy of $\sim \pm 0.03\%$ (± 2 THz). Note that it is easy to obtain an accuracy much higher than the resolving power of the instrument. An alternative technique for calibration of the optical frequency is to use a well-characterized, narrow-band optical source (e.g., a He–Ne laser) at one wavelength and record the interference fringes, which can be used to calibrate the scaling constant, zc/d. Once determined, that constant can be used to accurately calibrate the spectrum of an optical field in any spectral region.

The HHG spectrum appears as two sidebands well separated from the dc term of the spatial frequency distribution. The harmonic peaks are broadened because of the intrinsic resolution of this measurement; i.e., we measure a convolution $T(v) \otimes S(v) \mu_{12}(v)$ or $T(v) \otimes S(v)$, assuming constant $\mu_{12}(v)$, as is the case for this experiment. The broadening is evident from the comparison of the spectrum measured by the x-ray spectrometer (dashed curve of Fig. 5-13) compared with the pinhole spectrum (solid curve). However, the width of the spectrum obtained from the x-ray spectrometer after being convolved with the dc spike is identical to that obtained from the pinhole pair. The difference in the intensity of the two spectra is due

to the varying efficiency of spectrometer response, assuming constant spatial coherence across the harmonic spectrum, as explained above. The inset of Fig. 5-13 plots the ratio of the two spectra, $[S(\nu)\eta(\nu) / S(\nu) = \eta(\nu)]$. The spectral response, including an ~ 50-nm SiO_2 passivation layer on the CCD chip, must also be known for a complete determination of the spectral intensity distribution.

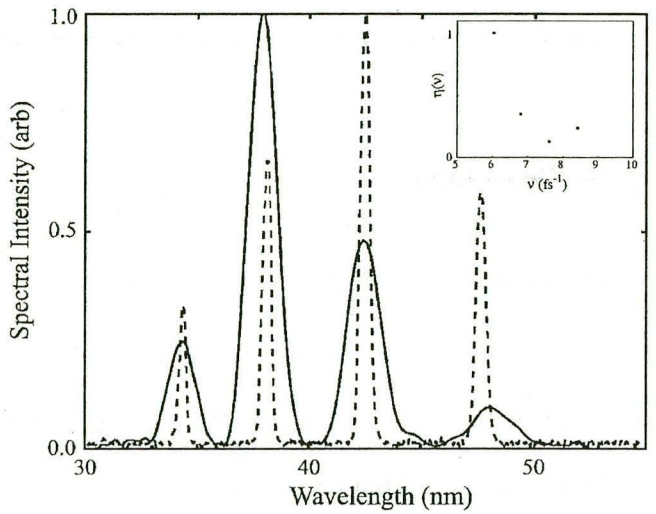

Figure 5-13. EUV spectrum obtained from a spectrometer $[S(\nu)\eta(\nu)]$ (dashed curve) and from the two-pinhole interference measurement $[S(\nu)]$ (solid curve). The inset shows the spectrometer relative efficiency, $\eta(\nu)$, inferred from these data. When the spectrometer data are convolved with the pinhole resolution, the measured and calculated linewidths agree to within 10%.

In summary, we have experimentally demonstrated a robust and accurate technique that allows the absolute wavelength and spectrum of a light field to be determined from the far-field interferogram produced by a pinhole pair. Furthermore, this technique provides a

convenient method of absolute calibration in the EUV region of the spectrum where few tunable sources currently exist. The spectrum obtained is verified with the spectrum measured by a conventional grating spectrometer. The resolution of the pinhole-pair spectrum can be improved by a simple change in geometry, by either shrinking the pinhole diameter or increasing the pinhole separation, at the cost of reduced photon flux. The quality of the data is extremely high because of the implicit averaging of the two-dimensional Fourier transform. Finally, this experiment provides verification of an important link between the spatial coherence properties of an optical field and its power spectrum.

5.4 Ultrashort Pulse Generation

One the most exciting features of HHG is its ability to generate very short duration pulses. Through HHG, people can, for the first time, reach the attosecond (1 as = 10^{-3} fs = 10^{-18} s) regime. For this reason, we include this section to introduce some of the efforts worldwide to generate attosecond pulses through HHG process.

Femtosecond lasers have been widely used in the investigation of chemical dynamics, for example atomic motion in molecules and phase transitions. Studies in ultrafast phenomena have made great contributions to basic science [99]. HHG source, pumped by a femtosecond laser, has the ability to generate ultrashort pulses. Many of the techniques utilizing EUV/SXR radiation introduced in chapter 1 will find new interesting applications with such short pulses.

More exciting is the adventure to even shorter pulses. In the past decades progress in ultrafast laser technology has pushed the pulse duration of optical laser to their physical limit; the shortest pulses are now only a few wave cycles. However, the long wavelength becomes the ultimate limit. For example, one cycle of 800-nm laser lasts 2.7 fs. Therefore,

ultrafast optical lasers are not capable of exploring dynamics on a sub-fs time scale. To explore faster dynamics, for example electronic dynamics inside atoms, even shorter pulses are needed. HHG provides a viable technique for the generation of attosecond pulses because of its shorter wavelengths. Earlier works on attosecond pulse generation through HHG were limited to a "train" of short pulses, as a result of coherent superposition of the harmonics. It has been predicted [100] the HHG harmonics generated in a macroscopic medium are locked in phase if phasematching is realized. Those many phase-locked harmonics, with spacing of $2\omega_0$ in frequency domain, can combine and generate "spikes" in time domain. The width of the resultant spikes is determined by the number of harmonics involved; the separation is set by half laser period T_L (See Fig. 5-14). The mechanism is similar to a mode-locking laser with many phase-locked longitudinal modes.

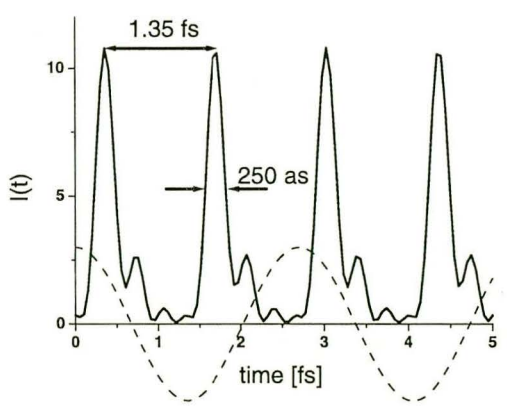

Figure 5-14. A calculated train of attosecond pulses generated by HHG. The temporal intensity profile is reconstructed from the sum of five harmonics, with measured phases and amplitudes. The FWHM of each pulse is ~ 250 as. From Paul et al., Ref. 101.

The aforementioned attosecond pulse train with separation of only a couple of femtosecond ($T_L/2$ = 1.35 fs for 800-nm fundamental laser) limits its application. More desirable is

isolated attosecond pulses. This can be done with HHG using complicated polarization [102], or using extremely short pulse duration (referred to as "few-cycle" pulses) IR/visible lasers [103, 104]. The latter is graphically illustrated in Fig. 5-15. In "few-cycle" pulses, the electric field reaches its peak magnitude only in (the central) one cycle. Based on the semi-classical model, photons with highest energy (in the cutoff region) would be generated within a very narrow time window (the electron has to be released with "perfect" phase to gain maximum kinetic energy), which is much less than one optical cycle.

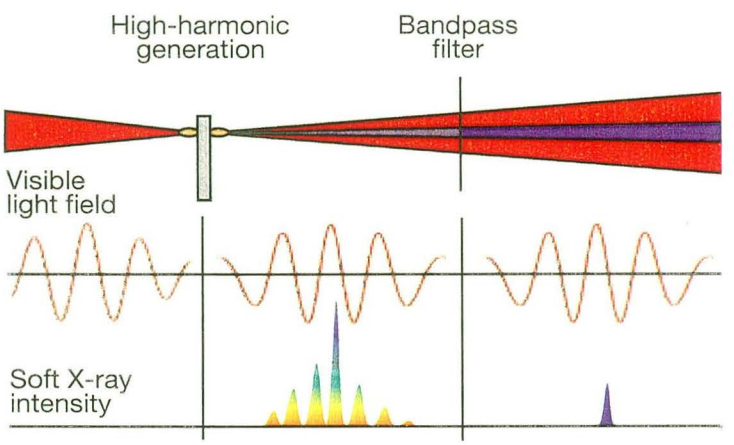

Figure 5-15. Isolated attosecond pulse generation through HHG process. First, the few-cycle visible light pulse interacts with a jet of neon atoms to produce a train of pulses in the EUV and soft-X-ray spectral range. The rainbow colors of the individual pulses symbolize the respective spectral energy content. The highest photon energy components are contained only in a single pulse generated near the peak of the driver pulse. After a high-pass filter, an isolated attosecond pulse would be obtained. From Hentschel et al., Ref. 105.

5.5 Comments on HHG as EUV/SXR Source

The HHG source described in this chapter generates spatially coherent EUV radiation at around 30 nm, with photon flux of ~2×10^{12} photons/s. This roughly converts to an average power of several μw in one harmonic peak. Such a power level in EUV is very useful for applications such as imaging, metrology and optic inspection, etc. It can be further improved using higher pump power and higher repetition rate. The peak power is extremely high, thanks to the short pulse duration. When properly focused, the intensity would reach a very high level, permitting nonlinear optical studies in EUV/SXR region.

However, the good performance of the source benefits a lot from the phase-matched interaction inside the fiber. Without using the phase-matching technique, as in the cases of HHG in gas jets, the available photon flux is usually 2-3 orders of magnitude lower. The 30-nm wavelength is still longer than the more important 13-nm wavelength for EUV Lithography and 2.4 to 4-nm wavelength (water window) for biological imaging. Similar to the situation for EUV lasers discussed in the last chapter, pushing to shorter wavelength using HHG also proves to be very challenging. The cut-off law of HHG (Eq. (5-5)) implies higher photon flux can be reached with higher intensity lasers. However, using a very strong pump laser, the ionization rate may be too high, such that many atoms would be quickly ionized. Less number of neutral atoms left will result in lower HHG yields. Moreover, the phase-matching will also be much more difficult to realize and maintain. High ionization rate will produce more free electrons. Electron dispersion will accelerate the phase velocity of the pump (see Eq. (5-11)). This term is small for low ionization; however, the contribution of this term goes up rapidly with intensity, to an extent that the pump will travel too fast to be phase-matched. As a result, efficient phase-matched HHG is limited to photon energy <90

eV. At higher energies, the EUV/SXR photon yields are too low for HHG to be a practical source for many experiments. Very recently quasi-phase-matching has been demonstrated at >100 eV [106], and in the water window [107], in a diameter-modulated hollow fiber. Progress with this novel quasi-phase-matching technique would help improve the photon flux at shorter wavelengths and extend the applications of HHG sources further into the EUV/SXR spectral region.

Chapter 6

Other EUV/SXR Sources

As we have seen in previous chapters, producing coherent radiation at EUV/SXR wavelengths requires quite a great effort. Coherent radiation is necessary for applications relying on interference effects, for example interferometry, holography and coherent imaging. For some other applications, a high degree of coherence is not necessarily a merit, indeed sometimes is even problematic. For example, in microscopy and lithography, spatial coherence can limit optical performance by introducing ringing and speckle effects, thus having impact on resolution, depth of focus, etc. Optimal resolution is usually achieved with partially coherent illumination (see section 2.2) and thus coherent sources are not always desired. In this chapter, we discuss examples of other EUV/SXR sources, most of them largely incoherent. They are either routinely used or being actively pursued, in support of ongoing research or proposed future applications.

6.1 Synchrotron-Based Sources

Chapter 3 has focused on undulator radiation. There are other two forms of synchrotron radiation based on relativistic electrons accelerated by magnetic fields, bending magnets and wigglers, also widely available in modern synchrotron radiation facilities, each producing short wavelength radiation for various applications. Fig. 6-1 shows a schematic comparison of them. In following subsections we will briefly summarize the properties of bending magnet and wiggler radiation.

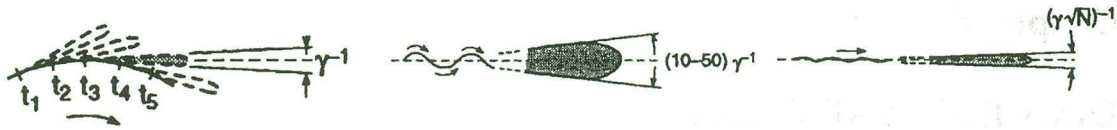

Bending Magnet – A "Sweeping Searchlight" | Wiggler – Incoherent Superposition | Undulator – Coherent Interference

Figure 6-1. Emission pattern for synchrotron radiation from different magnet structures: bending magnet, wiggler, and undulator. (Following Ref. 108)

6.1.1 Bending Magnet Radiation

Bending magnet radiation requires the simplest structure (dipole magnet) and is least expensive to construct. It is also used to bend the electron beam so that it travels within the circular (or near-circular) storage ring and can be continuously re-circulated. Involving only a short impulse field (a fraction of a cycle), it produces a very broad spectrum of radiation, useable for many applications. For these reasons, bending magnet beamlines are widely available, even in 3rd-generation facilities optimized for undulator radiation. Bending magnet radiation is the earliest noticed form of laboratory synchrotron radiation and has been thoroughly studied. Here we include only some most important attributes. The spectrum and photon flux are closely related to a parameter, the "critical" photon energy E_c, which is defined as:

$$E_c = \frac{3e\hbar B\gamma^2}{2m}$$

where e and m is charge and mass of electron, B is the strength of magnet field, $\hbar$ is Planck's constant and $\gamma = E_e / mc^2$ is the relativistic factor (E_e is the electron beam energy). Within a

bandwidth of $d\omega/\omega$ at photon energy E, the on-axis photon flux per unit solid angle is given by [33]

$$\left.\frac{d^3F}{d\theta d\psi d\omega/\omega}\right|_{\psi=0} = 1.33\times10^{13} E_e^{\,2}(GeV)I(A)H_2(E/E_c)\frac{photons/s}{mrad^2\cdot(0.1\%BW)}$$

where I is the electron beam current, and θ and ψ are the in-plane (plane of the electron's circular path) and out-of-plane angle, respectively. The function H_2 is related to a modified Bessel function of the second kind (denoted by K) as

$$H_2(y) = y^2 K_{2/3}^2(y/2)$$

Bending magnet radiation has a characteristic emission angle of $\sim 1/\gamma$ in the out-of-plane (ψ) direction. The ψ-dependence can be integrated, giving the photon flux per unit in-plane angle (θ) as

$$\frac{d^2F}{d\theta d\omega/\omega} = 2.46\times10^{13} E_e(GeV)I(A)G_1(E/E_c)\frac{photons/s}{mrad\cdot(0.1\%BW)}$$

where G_1 is another function, also related to the Bessel function K, as:

$$G_1(y) = y\int_y^{\infty} K_{5/3}(y')dy'$$

Figure 6-2 shows the plots of H_2 and G_1, as functions of the parameter E/E_c. One observes that bending magnet radiation is basically a broadband "white" light, covering a very wide spectral region, typically extending from the infrared to hard x-rays. The importance of E_c is illustrated in the plot. Half of the radiated power is in photons of energy less than E_c and the other half in photons of energy above E_c. The spectrum has an effective cutoff at around $4E_c$, above which the available photon flux is significantly lower. Using the Advance Light Source (ALS) in Berkeley as an example, with a 1.9 GeV (γ=3720) storage ring and a

bending magnet strength of B=1.27 tesla, the critical photon energy is 3.07 keV. Thus, the spectrum covers the entire range of EUV/SXR wavelengths, from several tens eV to more than 10 keV. This wide spectrum coverage provides convenient flexibility to various applications. For example, in beamline 6 at ALS, the bending magnet radiation is providing sufficient photon flux to both a SXR microscope, operating at 500 eV or higher, and an EUV metrology and calibration tool, operating in the 100 eV region. An ongoing upgrade at ALS has installed some "superbend" magnets with a stronger field, extending the spectrum well into the hard x-ray region, although ALS is considered a "low energy" machine with its 1.9 GeV electron energy.

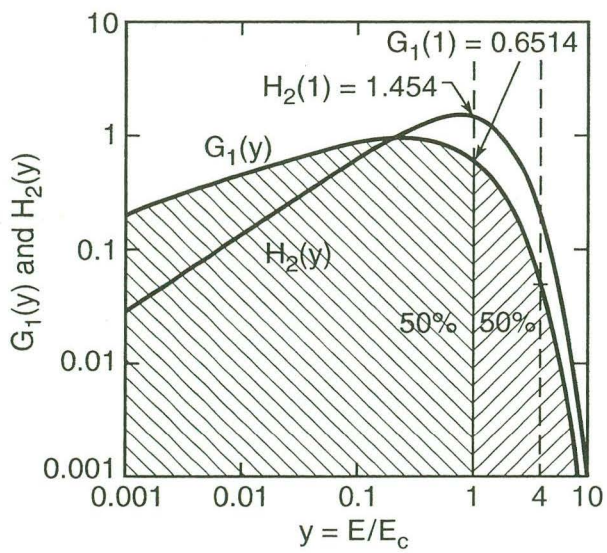

Figure 6-2. Functions H_2, representing on-axis photon flux density from a bending magnet, and G_1, representing the vertically integrated photon flux, as functions of photon energy normalized to the critical photon energy. [From Chapter 5, Ref. 1]

With bending magnet radiation "sweeping" in the in-plane direction, more photon flux can be obtained using a larger collection angle θ. On the other hand, the brightness is still limited. Without the interference effect between N periods, the spectral brightness of bending magnet radiation is generally N^2 lower than undulator radiation. With N~100, this results in a typical 4 orders of magnitude lower spectral brightness. For example, at ALS the typical spectral brightness for bending magnet radiation is on the order of 10^{14}-10^{15}, in unit of photons/s/mrad^2/mm^2/0.1%BW, compared with 10^{18}-10^{19} for undulator radiation.

6.1.2 Wiggler Radiation

Wiggler radiation has been briefly discussed in section 3.2. It corresponds to the limiting case of $K >> 1$, where the angular excursions of the electrons are much larger than $1/\gamma$ so that the radiation from the various magnet periods do not overlap, and therefore no interference effect occurs. As a result, the wiggler radiation can be well described as the incoherent superposition of 2N bending magnet radiation. Its spectrum is more similar to continuous broadband bending magnet radiation, than to the discrete peaks of undulator radiation. It provides higher power than bending magnet (due to the factor 2N) and reaches shorter wavelengths than undulator can (due to higher permitted magnetic field). Its spectral brightness is higher than bending magnet, but still usually 2 orders of magnitude lower than undulator radiation at its resonant wavelengths (see Fig. 6-3). Wiggler can be a good candidate for applications in which high photon flux is desired but coherence is not important.

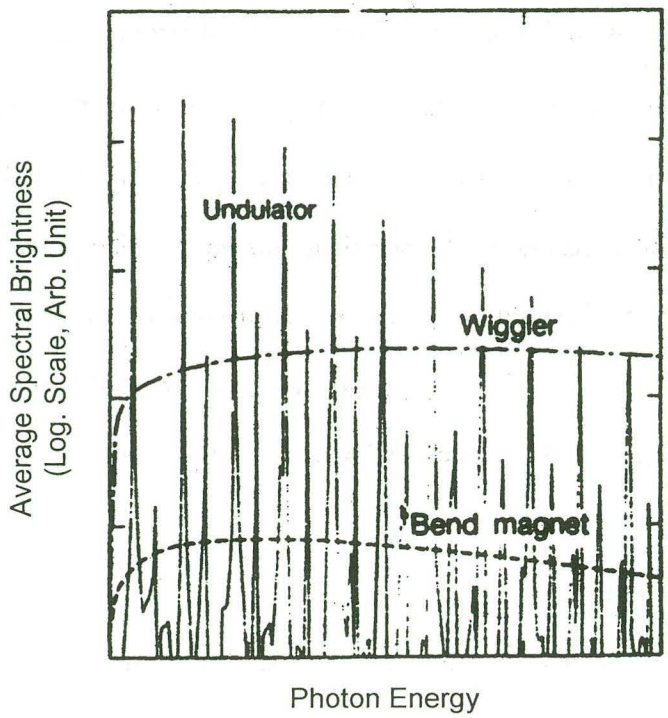

Figure 6-3. An illustration of different spectral characteristics of radiation from bending magnet, wiggler and undulator. [33]

6.1.3 Femtosecond Pulses at Short Wavelengths

Ultrafast EUV/SXR and x-rays provide many exciting research opportunities, as discussed in section 5.4.1 on femtosecond and attosecond pulse generation. In synchrotron radiation facilities, highly relativistic electrons offer another approach for the production of very short pulse duration radiation. As discussed in chapter 3, for an undulator, the Lorentz space-time transformation causes a factor of $2\gamma^2$ contraction in the observed radiation wavelength compared with the undulator period λ_u (Eq. 3-5). Correspondingly, there is a factor of $2\gamma^2$ reduction in pulse duration when compared with the time needed for an electron to pass the undulator. More specifically, assuming the undulator has N periods, the time for an electron to pass the undulator is (for highly relativistic electron, we have v ~ c)

$$\tau_{travel} = N\lambda_u / c$$

It is generally not short. For example, a 6-meter long undulator corresponds to a travel time of 20 ns. However, the pulsewidth of the observed radiation is

$$\tau_{rad} = N\lambda_{rad} / c = N(\lambda_u / 2\gamma^2) / c = \tau_{travel} / 2\gamma^2$$

since the radiation has only N periods of oscillation at the shorter wavelength λ_{rad}. Assuming a 5.1-GeV electron energy (γ~10,000), the pulsewidth can then be "compressed" to 0.1 fs, or 100 as. For bending magnet radition, the pulsewidth of the radiation from a single electron is even shorter. We can use the uncertainty principle to roughly estimate it:

$$\tau_{b.m.rad} \approx 1 / \omega_c$$

where $\omega_c = E_c / \hbar$ is the angular frequency corresponding to the critical photon energy E_c. With typical E_c in keV region, the pulse duration is also on the order of attoseconds.

The above estimations are based on a single electron. In a storage ring, the electrons travel in "bunches". Those bunches, however, typically have duration on the order of 10s of picoseconds, too long for modern investigations of ultrafast dynamics. Therefore, for current synchrotron radiation experiments, the factor limiting pulsewidth is the duration of the electron bunches. A recent experiment performed at ALS overcame this by using a "laser slicing" technique to separate a very narrow electron pulse (τ_{slice} ~ 100 fs) from the longer electron bunch in the storage ring (τ ~ 30 ps for ALS). In the experiment, femtosecond laser pulses (~100 fs) from a Ti:sapphire laser system were synchronized to the storage ring master clock and co-propagated with the electron bunches through a wiggler. The high electric field of the laser pulse produces an energy modulation to the electrons; the electrons can be accelerated or decelerated, depending on the optical phase seen by the electron at the entrance of the wiggler. Optimized condition for energy modulation occurs when the wiggler

is resonantly tuned, i.e., the central wavelength of the wigglers, $\lambda_0 = \lambda_w / 2\gamma^{*2}$ (same notations as used in chapter 3), equals to the laser wavelength. The energy modulation can be several times as large as the original electron beam energy spread, and the electrons with modulated energy can be spatially separated from the electron bunch in a dispersive bending magnet. The electron "slice" then radiates in a following bending magnet, producing femtosecond x-ray pulses, which can also be spatially separated at the beamline image plane and utilized in downstream experiments. This process is illustrated in Fig. 6-4.

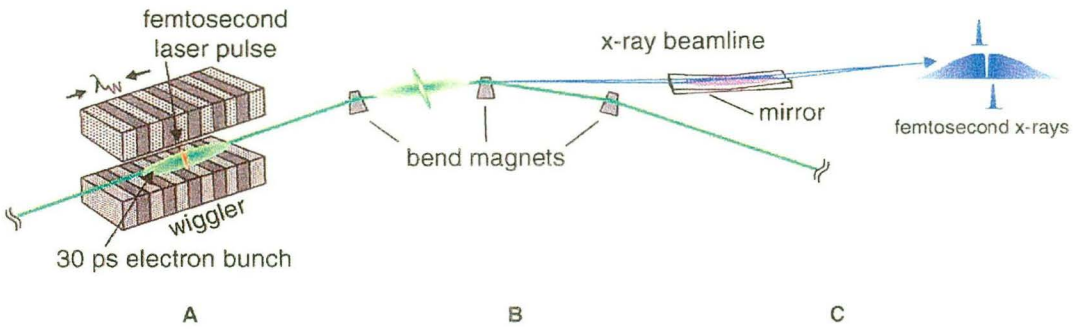

Figure 6-4. Schematic of the laser slicing method for generating femtosecond synchrotron pulses. (A) Co-linear laser interaction with electron bunch in a resonantly tuned wiggler. (B) Transverse separation of energy modulated electrons in a dispersive bend of the storage ring. (C) Separation of the femtosecond synchrotron radiation at the beamline image plane. From Schoenlein et al., Ref 109.

Another proposal [110, 111], the LUX (Linac-based Ultrafast X-ray facility), proposes to use dedicated, recirculating, superconducting linacs to produce 2.5-3 GeV electron beam at 10 kHz repetition rate. The pulse length of the electron bunch is 2 ps. Soft x-rays will be produced through laser seeded, cascaded harmonic generation process in undulators [112]. The process is a seeded FEL (free electron laser) process, in which two undulators are used.

The first one is modulator, in which the electric field of the seed laser modulates the energy of the electrons. The modulator is followed by a dispersion section, in which the energy modulation is converted into a coherent spatial density modulation. The electron bunch then enters another undulator, the radiator, which is tuned to harmonic wavelength of the seed laser and radiates coherently. Using a tunable seed, calculations indicate that it could produce femtosecond harmonics in the 20 eV - 1 keV spectral region by using four cascaded stages (Fig. 6-5). The light will be fully coherent, with 10-200 fs pulse duration. For hard x-rays, the electron beam will pass through 2-meter-long, 1.4-cm period undulators and generate high spectral brightness undulator radiation. Novel bunch tilting and x-ray pulse recompression is proposed to compress the x-ray pulse to less than 100 fs [113]. The photon energy would be tunable over 1-12 keV, by utilizing undulator harmonics. Both soft and hard x-rays would be synchronized with pump laser systems for excitation/probe experiments.

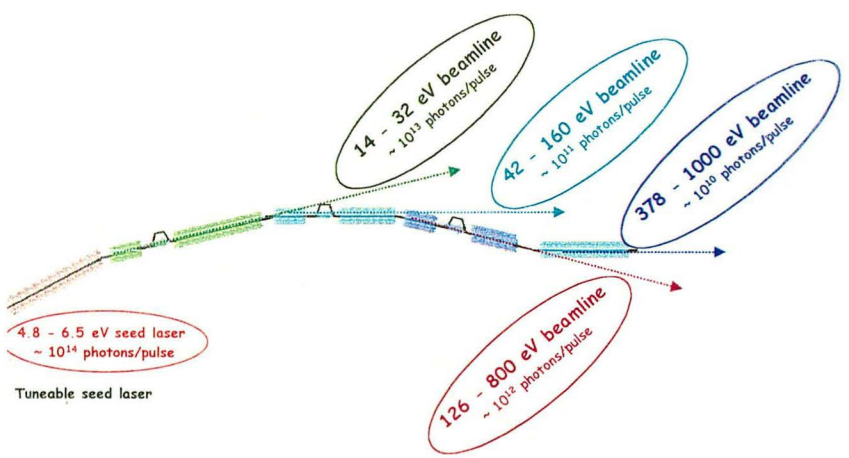

Figure 6-5. In the proposed LUX facility, soft x-rays are generated through laser seeded, cascade harmonic generation process, covering photon energies of 20 eV - 1 keV. The output would preserve the coherence of the seed laser. From Ref. 111.

An earlier effort to produce femtosecond x-ray involve Thomson scattering of femtosecond infrared laser pulses by relativistic electrons [114]. The scattered light was frequency up-shifted to the x-ray region by a similar factor of $2\gamma^2$ (90° scattering, forward direction). With this setup, a modest electron energy (50 MeV in the experiment, γ=98) was sufficient to generate 30 keV hard x-ray photons using an 800-nm infrared laser. The duration of the x-ray pulse was about 300 fs. This approach has the advantage of reaching the hard x-ray region using lower energy electrons, but generated only a modest photon flux due to small Thomson scattering cross section. (In the reported experiment, $\sim 3 \times 10^4$ x-ray photons per 300 fs pulse were collected under the following conditions: 60-mJ, 100-fs (FWHM) laser pulses; electron bunches of 1.3 nC charge, 20 ps (FWHM) pulse duration; and an interaction region of 90 μm in diameter.)

6.2 Plasma Radiation Sources for EUV Lithography

Plasma radiation sources are small-scale sources and thus can be widely deployed. They are of essential importance for more widespread use of short wavelength applications, for example EUV Lithography (EUVL). EUVL, as the leading candidate for next generation lithography at feature sizes of 32 nm and below, is experiencing extensive research and engineering investments from the semiconductor industry and collaborating national labs. One of the top issues for the success of EUVL is the source. To match the good performance of Mo/Si multilayer-coated mirrors, EUVL operates in the 13-14 nm wavelength region. A typical EUV stepper (the optical printing tool) consists of 9 to 10 multilayer mirrors, limiting the effective bandwidth to about 2% - 2.5% (See Fig. 1-4 for a typical reflection curve of one multilayer coating). High volume production tools require

high average power from the source to be economically competitive. The current requirement on the EUV radiation source is an in-band power (2% bandwidth, 13.5 nm central wavelength, spectrally clean and particulate free) of about 100 W at an intermediate focus (after collecting optics) to support a processing rate of one hundred 300-mm wafers per hour. There are also stringent requirements on repetition rate, stability of output power, etendue (equivalent to phase-space product), and lifetime of the condenser optics, etc [115]. Current efforts toward commercial EUVL sources include laser-produced-plasma (LPP) and electric discharge plasma sources. In LPP, high (peak and average) power lasers are used to generate a plasma and heat it to an EUV emitting temperature. The target is usually Xe, while other materials, for example Sn, are also under investigation. An LPP source is relatively easy to scale up (by using more powerful pump laser), but the overall conversion efficiency (from electricity to EUV) is low. Discharge sources use a high current electrical discharge to initiate and heat the plasma. They directly convert electrical power to EUV radiation, thus the overall efficiency is higher. They are also very compact. However, one big problem facing discharge sources is debris. Particles are generated from hot plasma interaction with the electrodes and surrounding materials. These particles must be prevented from reaching the multilayer collecting optics as the deposition will quickly degrade the mirror reflectivity. Gas curtains and traps are used to reduce particle contamination, but the problem is not yet solved.

Table 6.1 lists the current accomplishments of EUVL source developers. While the output power has been improved significantly during the past several years, the available clean, in-band power is still a factor of ten low. As can be seen from the table, the current best level of power at intermediate focus is about 10 W, far from the required ~100 W. Further improvements are clearly needed if this technology is to be used in 2009, as planned. To

increase the EUV power, possible approaches include scaling up the laser or discharge drive power and increasing conversion efficiency, the latter by creating more favorable plasma conditions and perhaps using alternate materials. Increasing pump power will also require improved thermal management, better control of debris, and other engineering considerations. The challenge facing source developer is significant, and presently a bottleneck for the commercial deployment of EUVL.

Table 6-1. Comparison of current EUV Lithography source candidates as of February 2003
(Courtesy of G. D. Kubiak, Sandia National Lab)

Source	Laser-produced plasma	Dense Plasma Focus	Capillary discharge	Hollow-Cathode Triggered Pinch	Z-Pinch	Star Pinch
Developers	TRW, Jmar, VNL, Xtreme Tech., PowerLase, EUVA	Cymer	VNL/UCF, Gremi, EUVA	Philips, ILT Aachen	Xtreme Tech.	PLEX
Demonstrated 13 nm power (W/sr in 2% BW)	3.5	4.3 avg, 17.2 burst	2.9	10.5 (Xe) 31.5 (Sn)	8 avg. 23.9 burst	9
Power @ Inter. Focus (W)	9.4	5 Avg.	4	5 (Xe)	6.9 Avg.	9
Demonstrated average repetition rate	5000	1000	10,000	4500	2000	1000
Demonstated peak repetition rate	6000	4000	10,000	4500	6000	1000
Projected repetition rate	26000	6000-10,000	>10,000 (mpx)	>6000	>6000	8000
Input pulse energy (J)	0.9	12	3	2.67	5.0 - 15.0	10
Projected heat load (W)	23,000	up to 90,000	30,000	30,000	up to 90,000	80,000
Source size (mm)	0.3 Diam.	0.4 Diam x 2.5	0.8 Diam.	0.5 Diam. X 1.8	1.3 Diam. X 2.3	~0.7 Diam x 3.2
Source-limited "C1" Lifetime (pulses)	2.0E+08 - 1E+09	>5E+07	1.0E+07	1.0E+08	>1.0E+06	>1.0E+07
Maximum demonstrated CE in 2π sr	0.9% Xe, 2.2% Sn	0.45%	0.30%	0.55%	0.55%	0.60%

Chapter 7

Conclusion

We have investigated the properties of three currently available EUV/SXR sources: undulator radiation, laser, and high-order harmonic generation. In this final chapter, we summarize and compare their attributes and limitations for potential applications.

Of the three kinds of sources, undulator radiation has the best spectral coverage and highest average power (photon flux). Undulators in low energy (1-3 GeV) synchrotron radiation facilities provide continuously tunable radiation throughout the EUV/SXR region. Reaching shorter wavelength (hard x-rays) can be realized in a straightforward way, by using higher energy (6-8 GeV) machines. The central radiation cone of undulator radiation typically contains watt-level average power, within a few percent relative spectral bandwidth. The central radiation cone power can be further filtered, both spectrally and spatially, to provide radiation with desired coherence properties. Milliwatt-levels of spatially coherent power are readily obtained.

Limited accessibility to synchrotron facilities is a significant obstacle for the spreading of EUV/SXR science and technology. The other two kinds of sources, the laser and HHG source, hold the promise of becoming complementary sources because of their smaller sizes. In the experiments described in previous chapters, we demonstrated both sources' capabilities to produce coherent EUV radiation at very useful power level. Moreover, both of them have some unique properties that are not available with undulators. For lasers, high energy per pulse and good temporal coherence (monochromaticity) make them the suitable sources for experiments such as single-shot interferometry and 3-D holography. For HHG,

the femtosecond (and even shorter) pulse duration will push ultrafast phenomenon studies to a new spectral region. Both of the compact sources also generate much higher peak powers, promising new opportunities for nonlinear optics and strong light-matter interaction studies in the EUV/SXR region.

The two tabletop sources have their limitations. They both face significant challenges to reach shorter wavelengths (see section 4.4 and 5.4 for detailed discussions). Except for the 46.9-nm laser described in this thesis, the spatial coherence of other EUV/SXR lasers is still quite limited, due to their ASE-based configuration. For HHG, the conversion efficiency is still low, limiting the pulse energy to the nJ-level and average power to the μW-level, even with phase-matching.

The above comparisons are summarized in Table 7-1.

Table 7-1. Comparison of the three sources

Undulator	✓ Tunable across a wide range ✓ Very useful average power ✓ Good coherence with filtering	✕ Big Facilities ✕ Limited Accessibility
Laser	✓ Monochromatic ✓ High energy per pulse ✓ Good spatial coherence (EUV)	✕ Limited spatial coherence (SXR) ✕ Scalability to shorter wavelengths
HHG	✓ Coherent ✓ Good spectral coverage (EUV) ✓ Ultra-short pulse	✕ Pulse energy /Average power ✕ Scalability to shorter wavelengths

Given the difficulties for both laser and HHG source to reach higher photon energies, undulator radiation will continue to be the best coherent radiation source for SXR wavelengths (< 5 nm). At the longer EUV wavelengths, with rapid progress in both laser and HHG source developments, it is very likely that these two sources will be able to provide adequate power and stability for practical applications in the coming years. In fact, the two particular sources described in this thesis have already been used in applications of interferometry and holography. The compact sources will accelerate scientific and technological advances in areas such as metrologies for EUV lithography, microscopy, high-density plasma dynamics probing, and ultrafast dynamics of molecules and surfaces. Moreover, once the sources become widely available to more scientists, we believe new ideas and applications will emerge. The next decade will probably witness a fast expansion of EUV techniques to a larger community.

References:

1. D. Attwood, Soft X-rays and Extreme Ultraviolet Radiation: Principles and Applications (Cambridge University Press, 1999), Chapter 1
2. W. Chao et al., Opt. Lett., in press; W. Chao et al., SPIE 4146, 171 (2000).
3. D. Tichenor et al., SPIE 4688, 72 (2002); P. Naulleau et al., SPIE 4688, 64 (2002).
4. P. Naulleau et al., Appl. Optics 38, 7252 (1999); K. Goldberg et al., J. Vac. Sci. Tech. B 16, 3435 (1998).
5. D. Sayre et al., Science 196, 1339 (1977).
6. C. Magowan et al., Proc. Nat. Acad. Sci. U.S.A. 94, 6222 (1997).
7. P. Fischer et al., Rev. Sci. Instru. 72, 2322 (2001).
8. T. Nguyen, Ph.D. thesis, Applied Science and Technology Program, University of California at Berkeley (1993).
9. P. Naulleau et al., Sematech Symposium on EUV Lithography (Dallas, TX, November 2002).
10. E. Anderson et al., J. Vac. Sci. Tech. B 18, 2970 (2000).
11. C. Chang et al., Appl. Optics-IP 41, 7384 (2002).
12. See, for example, the Chandra X-ray Observatory specifications at http://chandra.harvard.edu/press/fact1.html.
13. A. B. C. Walker et al., Science 241, 1781 (1988); An example of compact EUV telescope is TRACE (Transition Region And Coronal Explorer), more details at http://sunland.gsfc.nasa.gov/smex/trace.

14. J. D. Jackson, Classical Electrodynamics, 3rd Edition (John Wiley & Sons, 1999), Chapter 14

15. J. J. Rocca, Rev. Sci. Instru. 70, 3799 (1999).

16. Z. Chang et al., Phys. Rev. Lett. 79, 2967 (1997); C. Spielmann et al., Science 278, 661 (1997).

17. M. Born and E. Wolf, Principles of Optics, 7th Edition (Cambridge University Press, 1999), Chapter 10

18. R. Loudon, The Quantum Theory of Light, 3rd Edition (Oxford University Press, 2000).

19. L. Mandel and E. Wolf, Optical Coherence and Quantum Optics (Cambridge University Press, 1995).

20. G. W. Goodman, Statistical Optics, (John Wiley & Sons, 2000), Chapter 5.

21. G. W. Goodman, Introduction to Fourier Optics, 2nd edition (McGraw-Hill, 1996), Chapter 2

22. R. J. Bell, Introductory Fourier Transform Spectroscopy (Academy Press, 1972).

23. Ref. 1, Chapter 8

24. B. J. Thompson and E. Wolf, J. Opt. Soc. Am. 47, 895 (1957).

25. Coherence and Fluctuations of Light (1850-1966) (SPIE, Bellingham, WA, 1990), L. Mandel and E. Wolf, Editors. P.H. van Cittert, pg.1; F. Zernike, pg. 100; the theorem is also discussed in detail in Chapter 8 of Ref. 1 and Chapter 10 of Ref. 16.

26. S. A. Ponomarenko and E. Wolf, Opt. Lett. 25, 663 (2000).

27. Ref. 21, Chapter 4

28. L. Jochum and W. Meyer-Ilse, Appl. Opt. 34, 4944 (1995).

29. H. J. Levinson, Principles of Lithography (SPIE Press, Bellingham, WA, 2001).

30. P. Salieres, A. L'Huillier and M. Lewenstein, Phys. Rev. Lett. 74, 3776 (1995); T. Ditmire et al., Phys. Rev. Lett. 77, 4756 (1996).

31. Ref. 1, Chapter 5

32. D.T. Attwood, K. Halbach, and K.-J. Kim, Science 228, 1265(1985).

33. K.-J. Kim, "Characteristics of Synchrotron Radiation," pp. 565-632 in Physics of Particle Accelerators, AIP Conference Proccedings 184 (Amer. Inst. of Physics, New York, 1989), M. Month and M. Dienes, Editors

34. H. Kitamura, Kasokuki Kagaku (Accelerator Sci.) 1, 45 (Ionics Publishing, Tokyo, 1986)

35. Ref. 1, Chapter 5, pp. 172-177.

36. A. Hofmann, "Theory of Synchrotron Radiation," Stanford Synchrotron Radiation Laboratory report ACD-Note 38 (unpublished).

37. ALS website: http://www-als.lbl.gov.

38. C. Chang et al, Opt. Commun. 27, 1028 (2002).

39. K. Rosfjord (CXRO/LBNL), private communication.

40. C. Chang et al, Opt. Lett. 27, 1028 (2002).

41. T. H. Maiman, Nature 187, 493 (1960); A. Javan, W. R. Bennett, Jr., and D. R. Herriot, Phys. Rev. 6, 106 (1961).

42. H. C. Kapteyn, Appl. Opt. 31, 4931 (1992).

43. A. Vinogradov, I. Sobel'man, and E. Yukov, Sov. J. Quantum Electron. 5, 59 (1975); B. A. Norton and N. J. Peacok, J. Phys. B 8, 989 (1975).

44. Table 6.2, Ref. 1.

45. R. C. Elton, X-ray Lasers (Academic Press, San Diego, 1990).

46. J. J. Rocca et al., Phys. Rev. Lett. 77, 1476 (1996).

47. J. J. Rocca, private communication.

48. Ref. 1, chapter 7, pg. 269

49. D. T. Attwood, in Proceedings of the First Symposium on the Applications of Laboratory X-Ray Lasers, edited by N. M. Ceglio (published by Lawrence Livermore National Lab as CONF-850293-Abstracts, 1985), pp. 74-83.

50. M. D. Rosen, J. E. Trebes and D. L. Matthews, Comments Plasma Phys. Controlled Fusion 10, 245 (1987).

51. Some representative spatial coherence measurements of EUV/SXR lasers can be found in:

J. E. Trebes et al., Phys. Rev. Lett. 68, 588 (1992).

Y. Kato et al., in Ultrashort Wavelength Lasers, edited by S. Suckewer (SPIE, Bellingham, 1992), pp. 56-64.

M. C. Marconi et al., Phys. Rev. Lett. 79, 2799 (1997).

R. E. Burge et al., J. Opt. Soc. Am. B 14, 2742 (1997); R. E. Burge et al., J. Opt. Soc. Am. B 15, 1620 (1998); R. E. Burge et al., J. Opt. Soc. Am. B 15, 2515 (1998);

More papers can be found in X-Ray Lasers 1996, edited by S. Svanberg and C-G. Wahlström(Inst. Phys., Bristol, 1996); and X-Ray Lasers 1998, edited by Y. Kato, H. Takuma and H. Daido (Inst. Phys., Bristol, 1998).

52. R. A. London, M. Strauss and M. D. Rosen, Phys. Rev. Lett. 65, 563 (1990); R. A. London, Phys. Fluids 31, 184 (1988).

53. P. D. Gasparyan, F. A. Starikov and A. N. Starostin, Physics-Uspekhi 41, 761 (1998).

54. C. D. Macchietto, B. R. Benware and J. J. Rocca, Opt. Lett. 24, 1115 (1999).

55. Y. Liu et al., Phys. Rev. A 63, 033802 (2001).

56. J. J. Rocca et al., Phys. Rev. Lett. 73, 2192 (1994).

57. B. R. Benware et al., Phys. Rev. Lett. 81, 5804 (1998).

58. Here we use coherence radius R_c to characterize the transverse coherence length. The definition of R_c is following the convention of coherence area A_c used in Ref. 20 as $\pi R_c^2 = A_c = \int\int |\mu_{12}(\Delta x, \Delta y)|^2 d\Delta x d\Delta y$. Therefore, a Gaussian profile $|\mu_{12}|$ would be $|\mu_{12}(\Delta x, \Delta y)| = \mathrm{Exp}\,(-(\Delta x^2 + \Delta y^2)/2R_c^2)$.

59. Ref. 20, pp. 171-187.

60. Y. Liu et al., SPIE 4505, 41 (2001).

61. A. E. Siegman, M. W. Sasnett and T. F. Johnson, Jr., IEEE J. Quan. Electr. 27, 1098 (1991).

62. A. E. Siegman and S. W. Townsend, IEEE J. Quan. Electr. 29, 1212 (1993).

63. S. Le Pape et al., Phys. Rev. Lett. 88, 183901 (2002).

64. C. Chenais-Popovics et al., Phys. Rev. Lett. 59, 2161 (1987); B. J. MacGowan et al., Phys. Rev. Lett. 59, 2157 (1987);

65. D. Korobkin et al., Phys. Rev. Lett. 81, 1607 (1998).

66. R. F. Smith et al., Phys. Rev. Lett. 89, 065004 (2002).

67. J. J. Rocca et al., Phys. Plasmas 10, 2031 (2003).

68. E. R. Bernstein, in proposal for a National Science Foundation EUV Engineering Research Center.

69. Ref. 1, Chapter 7; Ref. 15, Sec. II.

70. Y.-R. Shen, The Principles of Nonlinear Optics (John Wiley & Sons, 1984).

71. D. E. Spence, P. N. Kean and W. Sibbett, Opt. Lett. 16, 42(1991).

72. S. Backus et al., Rev. Sci. Instru. 69, 1207 (1998).

73. T. Brabec and F. Krausz, Rev. Modern. Phys. 72, 545 (2000).

74. M. Schnürer et al., Phys. Rev. Lett. 80, 3236 (1998).

75. J. W. G. Tisch et al., Phys. Rev. A 49, R28 (1994).

76. Ch. Spielmann et al., Science 278, 661 (1997).

77. Z. Chang et al., Phys. Rev. Lett. 79, 2967 (1997).

78. P. B. Corkum, Phys. Rev. Lett. 71, 1994 (1993).

79. K. Kulander, K. Schafer and J. Krause, in Super Intense Laser-Atom Physics, NATO Advanced Study Institutes, Ser. B, Vol. 316 (Plenum Press, New York, 1993).

80. M. Lewenstein et al., Phys. Rev. A 49, 2117 (1994).

81. R. W. Boyd, Nonlinear Optics, 2nd Edition (Academic Press, 2002), section 2.8.

82. W. Becker, S. Long and J. K. McIver, Phys. Rev. A 50, 1540 (1995).

83. M. Lewenstein, P. Salières and A. L'Huillier, Phys. Rev. A 52, 4747 (1995).

84. P. Salières et al., Science 292, 902 (2001).

85. M. Lewenstein, P. Salières and A. L'Huillier, Phys. Rev. A 52, 4747 (1995).

86. P. Balcou et al., Phys. Rev. A 55, 3204 (1997).

87. M. Bellini et al., Phys. Rev. Lett 81, 297 (1998).

88. C. Lyngå et al., Phys. Rev. A 60, 4823 (1999).

89. P. Salières, A. L'Huillier and M. Lewenstein, Phys. Rev. Lett. 74, 3776 (1995)

90. Dong Gun Lee et al., Phys. Rev. A 63, 021801(R) (2001).

91. L. Le Déroff et al., Phys. Rev. A 61, 043802 (2000).

92. L. Le Déroff, P. Salières and B. Carré, Opt. Lett. 23, 1544 (1998).

93. A. Rundquist et al., Science 280, 1412 (1998).

94. E. A. J. Marcatili and R. A. Schmeltzer, Bell Sys. Tech. J. July, 1783 (1964).

95. R. A. Bartels et al., Science 297, 376 (2002).

96. R. A. Bartels et al., Opt. Lett. 27, 707 (2002).

97. E. Wolf and A. Devaney, Opt. Lett. 6, 168 (1981).

98. A. Friberg and E. Wolf, Opt. Lett. 20, 623 (1995).

99. The 1999 Noble Prize in chemistry was rewarded to Prof. Zewail for his contributions to ultrafast revolution.

100. Ph. Antoine, A. L'Huillier, M. Lewenstein, Phys. Rev. Lett. 77, 1234 (1996).

101. P. M. Paul et al., Science 292, 1689 (2001).

102. P. B. Corkum, N. H. Burnett, and M. Y. Ivanov, Opt. Lett. 19, 1870 (1994).

103. I. P. Christov, M. M. Murnane and H. C. Kapteyn, Phys. Rev. Lett. 78, 1251 (1997).

104. I. P. Christov, M. M. Murnane and H. C. Kapteyn, Phys. Rev. A 57, R2285 (1998).

105. M. Hentschel et al., Nature 414, 509 (2001).

106. A. Paul et al., Nature 421, 51 (2003).

107. E. A. Gibson et al., Science 302, 95 (2003).

108. H. Winick, in Synchrotron Radiation Sources: A Primer, H. Winick, ed. (World Scientific, 1994).

109. R. W. Schoenlein et al., Science 287, 2237 (2000).

110. W. Barry et al., "Feasibility study for a recirculating linac-based facility for femtosecond dynamics", Lawrence Berkeley National Lab report LBNL-51766.

111. "LUX – A Linac-Based Ultrafast X-Ray Source for the Future" booklet, available at http://bc1.lbl.gov/CBP_pages/CBP/groups/LUX/.

112. L.-H. Yu et al., Science 289, 932 (2000).

113. Zholents et al., Nuclear Instru. Method A 425, 385 (1999).

114. R. W. Schoenlein et al., Science 274, 236 (1996).

115. G. D. Kubiak, "Prospects and Challenges for High-Power EUVL Sources", in SPIE's 28th Annual International Symposium and Education Program on Microlithography (Santa Clara, CA, February 2003)

Ernest Orlando Lawrence Berkeley National Laboratory
One Cyclotron Road | Berkeley, California 94720

Prepared for the U.S. Department of Energy under Contract No. DE-AC03-76SF00098